Politecnico di Torino

POLITECNICO DI TORINO

Master of Science Course
in Materials Engineering for Industry 4.0

A.A. 2024-2025

Master of Science Thesis

Development of Innovative Components for Integrated Electrochemical Carbon Capture and Utilization

Academic Tutor:
Prof. Fontana Marco

Co-supervisors:
Prof. Castellino Micaela
Dr. Sacco Adriano

Candidate:
Barberis Andrea

Abstract

In response to the global climate emergency caused by increasing atmospheric carbon dioxide (CO_2) concentrations, one of the most promising strategies is the capture and conversion of CO_2 (CCU) into value-added products. Among the various approaches, the Electrochemical CO_2 Reduction Reaction (eCO_2RR) enables the transformation of CO_2 into useful compounds through the use of electrolysers and specific electrocatalysts. In this context, bicarbonate electrolysers represent an innovative solution, capable of combining carbon capture and utilization in a single system, removing energy demanding processes. However, these devices still present significant challenges for future scale-up and industrial implementation. This thesis focuses on the development of advanced materials and components to optimize integrated CO_2 capture and utilization in bicarbonate electrolysers, with the specific objective of designing a low-energy, efficient electrolyser for the selective conversion of CO_2 into carbon monoxide (CO).

Experimental activities were carried out on an MEA (Membrane Electrode Assembly) electrolyser equipped with different catalytic systems. As a benchmark, silver nanoparticles-based gas diffusion electrodes (GDEs) were tested using 3 M $KHCO_3$ as catholyte and 0.05 M H_2SO_4 as anolyte. The electrochemical performance was monitored while optimizing silver-based catalysts. Improved activity was observed when silver nanoparticles were combined with sputtered silver layers on porous carbon substrates, enhancing both catalytic behavior and Faradaic efficiency. Additional tests in temperature and pressure conditions provided further information for the potential scalability of the system for industrial applications. In parallel, alternative low-cost catalysts were investigated to address the economic limitations associated with noble metals. In particular, cobalt phthalocyanine (CoPc), an organometallic single-atom catalyst, was investigated combined with carbon supports. Supported materials obtained by coupling CoPc with carbon nanotubes (CNTs) and carbon black (CB) were produced and characterized. The synthetized electrocatalysts were characterised using XPS, XRD and FESEM techniques in addition to electrochemical characterizations. Among these, the CoPc-CB 1:3 ratio, exhibited the best catalytic performance, achieving a Faradaic efficiency for CO of up to 56% under current densities of 200 mA cm^{-2}.

Overall, the results highlight the potential of integrating innovative catalyst design with advanced electrolyser architectures to overcome the limitations of conventional CCU systems. The optimized materials developed in this work demonstrate significant progress toward scalable, energy-efficient electrochemical processes, contributing to the vision of a circular carbon economy and sustainable industrial technologies.

Contents

List of Figures

List of Tables

The thesis work was carried out at the *Center for Sustainable Future Technologies of the Italian Institute of Technology* (IIT), under the supervision of Dr. Adriano Sacco.

Chapter 1

Introduction to Carbon Capture and Utilization

1.1 Climate crisis and emissions

Since the late 20th century, the Earth's average temperature has risen, rainfall has decreased, and sea levels have gone up. Largely due to the faster melting of glaciers and polar ice caps. At the same time, extreme weather events such as hurricanes, glacial earthquakes, and storms are becoming more frequent and more powerful, even in places that rarely experienced them before [1]. These environmental changes are creating serious social challenges: forcing people to migrate more often, driven by food shortages and the loss of liveable land after disasters. Migrations and disasters influence countries economies, many of which now depend on significant aid and financial support to recover [2].

A clear correlation can be observed between the escalation of environmental degradation and human activities, particularly those linked to industrialization [3]. The successive industrial revolutions have led to the intensive exploitation of finite and non-renewable natural resources, such as oil and natural gas, to satisfy the growing demands of technological advancement and a rapidly increasing global population [4]. The growing demand for large-scale energy and manufacturing has greatly increased pollutant emissions. These pollutants are either released directly into the environment or stored in landfills, where they cause lasting ecological harm.

Among the various sources of pollution, greenhouse gases (GHGs) represent the most critical and impactful category. Virtually all production processes, electricity consumption, and especially the extensive use of internal combustion engines contribute to GHG emissions. These gases, predominantly carbon dioxide (CO_2), methane (CH_4), and various industrial compounds, alter the composition of the atmosphere [5]. They contribute to the depletion of the ozone layer and intensify the greenhouse effect by trapping solar radiation within the atmosphere, leading to global warming. A natural greenhouse effect is present on Earth to create a balanced and mitigated environment for life to prosper, the increasing quantity of gases such as CO_2 (Figure 1.1) lead to an amplification of this natural effect. As of 2020, the emissions of CO_2 from anthropic activities amount to 30.000 Gt [6]. CO_2 generates Polar Stratospheric Clouds (PSC) over Artic regions catalyzing chlorine into reactive radicals accelerating the ozone depletion [7].
Addressing these adverse impacts necessitates direct and proactive human intervention. While the reduction of consumption and the transition to alternative energy sources are essential steps toward sustainability, they are insufficient on their own.

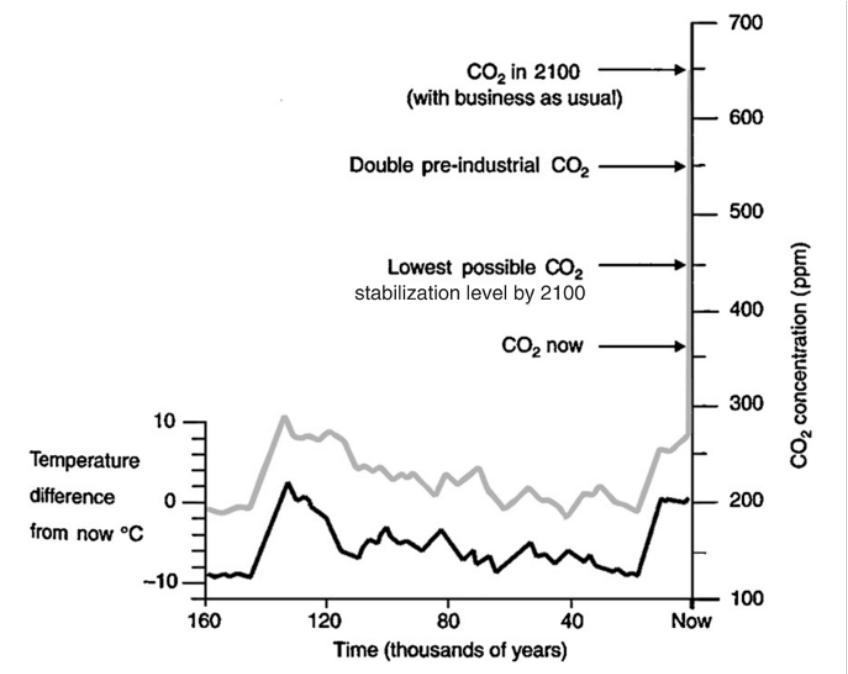

Figure 1.1: Comparison of polar temperature and CO_2 emissions in history [8].

An emergent strategy is through the capture of CO_2 and conversion into added-value products. This solution allows decarbonation of the atmosphere separating CO_2 and using it as feedstock for production of useful products. Efficient and economically suitable technologies are required to guarantee energetic sustainability of the process and efficient carbon conversion.

1.2 Carbon Capture and Storage

An initial possibility to reduce CO_2 concentration is to remove the excess emissions from the atmosphere and store the captured gas. Considering CO_2 present in atmospheric air and flue gasses of production plants, the definition of a capture process is: a selective removal of CO_2 from a mixture of gasses with the regeneration of material used for the separation via a reverse reaction. This separation is given by a chemical reaction or physical adsorption, efficiency of capture and separation is given by the "reversibility" of the process [9].

1.2.1 Chemical absorption

Historically, MonoEthanolAmine has been used in industrial applications [10] having the capability of selectively absorbing CO_2 and capturing the CO_2 in liquid form. [9] CO_2 reacts with the amine to create a soluble compound, but needs to be broken to release CO_2 after heating. The main drawbacks of the chemical dissolution are that CO_2 is present in low concentrations in air and in flue gases of production [11] meaning a low driving force for capture and requiring large equipment with high energy solvent regeneration. Flue gas might also contain contaminants like SO_x and NO_x that could degrade solvents easily. Liquid dissolution is widely used for its high TRL and costs, it comes also with its high energy demand: to release CO_2 gas from the captured liquid, high temperature processes are required. The regeneration energy of amine compounds is around 3.5 GJ/ton CO_2 [10], making the process extremely inefficient. Considering the overall amine-based capture process, it shows an energy demand of 6.5 GJ/tonne CO_2

and a cost of 61.4 euros/tonne CO_2 [12]. Other than amine solvents, other solutions have been studied for carbon capture such as bicarbonate dissolution that falls in the category of chemical absorption but is dependent on acidic equilibrium for CO_2 gas release. In this case too, the regeneration energy demand is high [13].

1.2.2 Physical adsorption

Possible alternatives to liquid capture are through specific adsorption on solid adsorbent material with physical bonds [14]. The flue gas or ambient air is fluxed on the adsorbent material that has been modified in order to adsorb only CO_2 molecules. The CO_2 molecules get adsorbed on the surface and can be released with temperature swings or pressure and vacuum swings. The materials used are zeolites, silicon based porous network with tunable adsorbent properties, and Metal Organic Frameworks (MOF), highly porous structure with organic and inorganic components [15]. These materials require also significant energy for regeneration and suffer from reduced performance with moisture and impurities. Compared to liquid capture, solid capture requires lower temperature and faster regeneration. Considering a porous silica adsorbent compound, silica-alkoxylated polyethyleneimine (SPEI), the capture energy requirements drop to 4.3 GJ/tonne CO_2 and the costs reduce to 49.8 euros/tonne CO_2 [16].
Adsorption is limited to the amounts of active sites on the solid surface, creating as such a limited amount of possible adsorption of CO_2, while in liquid-based capture the amount of possible dissolution is dependent on the solubility of the soluble compound and the quantity of solvent.
For these reasons, physical adsorption is an interesting and efficient technique but is limited for laboratory and specific applications such as filters of CO_2 on the ISS (international space station) but can't be used for industrial applications [17].

1.3 Carbon Capture and Utilization

Carbon Capture allows reduction CO_2 concentration but has a limited effect considering the low concentrations in air and flue gas. Furthermore, once captured CO_2 doesn't have any value or role if kept stored. An alternative to give value to captured CO_2 is **Carbon Capture and Utilization** (CCU). CCU aims to capture carbon dioxide from mixed gas streams, such as ambient air or industrial exhaust, and repurpose it into useful and less harmful by-products. This process not only mitigates the environmental impact of CO_2 emissions but also aligns with the long-term objectives set forth by international climate agreements, including the Paris Agreement (COP21, 2015).
Unlike the capture and storage technologies, CCU is the key and is helpful for creating added-value products and valorize atmospheric carbon waste.

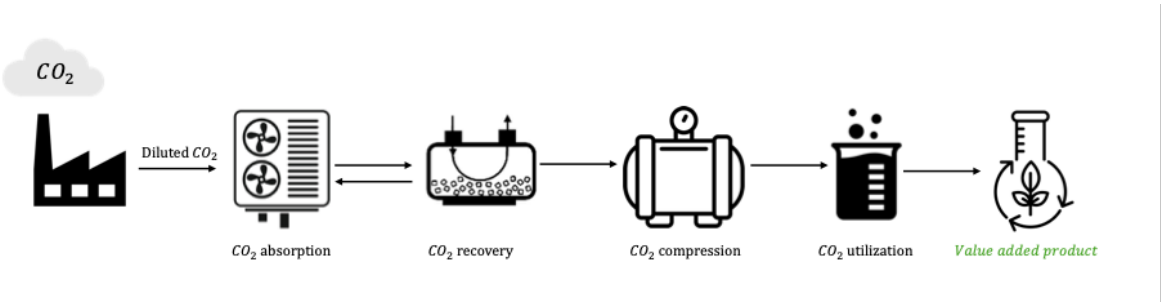

Figure 1.2: Schematic representation of Sequential CCU

As shown in the Figure 1.2, the capture and valorization system is composed of a capture module and a valorization module. The capture module is composed of a CO_2 absorption system that separates CO_2 gas from other gasses and stocks it in liquid or gas form. The valorization module is more complex having a CO_2 recovery system using thermal or energetic process. The regenerated CO_2 is compressed to create a steady gas flow which follows a reactive process to produce value-added products.

1.4 Valorization of carbon dioxide

After being captured, CO_2 is regenerated in a gas to be used in valorization reactions: reactions aiming to transform the CO_2 gas in added-value chemicals that can be used in other chemical processes or as fuels.
Since the $1800s$, CO_2 has been used for synthesis of chemicals but given its intrinsic stability ($\Delta Gf^\circ = -396kJ/mol$) and kinetic inertness, it requires effective catalytic techniques or high energy processes. Giving enough energy and modifying the external conditions, from CO_2 many organic compounds like carbon monoxide (CO) and methane (CH_4) gasses can be obtained but also more complex structures such as acids with carboxylation. The obtained compounds of CO_2 valorization and reactions can be divided in fuels and chemicals, thus closing the carbon loop being products that can be used in new production processes or as fuels but with lower GHGs emission impact [18].

1.4.1 Thermocatalytic processes

Given the thermodynamic stability of carbon dioxide, its chemical conversion into fuels or value-added chemicals typically requires high temperatures and pressures to activate the C=O bond. Thermocatalysis, driven by thermal energy, has emerged as a highly efficient and scalable approach, particularly suitable for the industrial-scale synthesis of fine chemicals such as hydrocarbons, olefins, and ammonia. As such, thermocatalytic CO_2 conversion is considered a promising route for producing high-value carbon-based compounds, primarily through hydrogenation reactions in the presence of suitable catalysts under controlled temperature and pressure conditions.
In thermocatalytic processes, CO_2 molecules initially adsorb onto the catalyst surface. To initiate the reaction, a significant amount of activation energy (Ea) is required to bend and weaken the C=O bond. A subsequent energy barrier must then be overcome for the formation of reactive intermediates, wherein hydrogen (H_2) acts both as the reducing agent and as a source of hydrogen atoms (H). The nature and strength of interactions between these intermediates and the catalyst surface play a critical role in determining the selectivity of the final products. By regulating C–H bond formation and C–C coupling mechanisms, the process can be tuned to favor either C_1 products or more complex and valuable C_{2+} compounds [19].
As illustrated in Figure 1.3, the hydrogenation of CO_2 without a catalyst requires substantial thermal energy to overcome the high activation energy (Ea_1) of the elementary reaction steps (solid line). In contrast, the use of effective catalysts significantly reduces these energy barriers (Ea_2 and Ea_3), thereby enhancing the overall reaction rate (dashed line). Therefore, the development and optimization of highly active and selective catalysts are essential for improving the efficiency of CO_2 thermocatalytic conversion [19].
Thermal energy is a fast and widely used process of delivering energy to a system but comes with drawbacks. Firstly, the Joule effect creating a low conversion rate from secondary energies (mainly electricity) to a primary energy such as heat. To generate the required thermal energy,

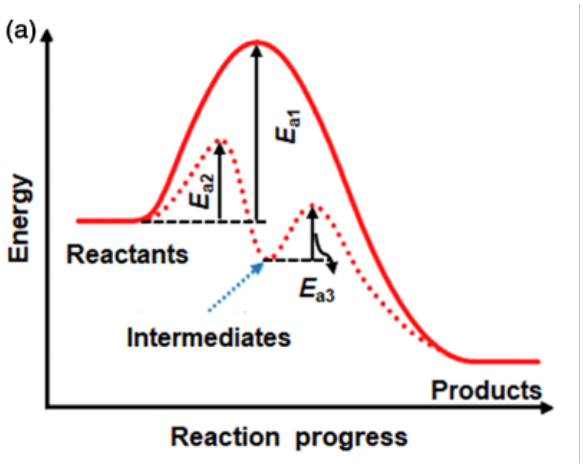

Figure 1.3: Comparison of the activation energies necessary to overcome with (Ea_2 and Ea_3) and without (Ea_1) the employment of a catalyst in the reaction. [19]

much more electricity is required creating energy consuming processes. Second main drawback is that generation of heat often is accompanied by CO_2 emissions that is unwanted for a process aiming to reduce CO_2 concentration.

1.4.2 Alternative catalytic processes

Alternatively, novel techniques have emerged through the use of organo-metallic catalysts reducing the operating temperature and pressure but also microalgae that have photosynthetic activity [20].
Microalgae, due to their photosynthetic activity, could be used to capture and valorize the CO_2. Microalgae have the ability of fixing CO_2 directly from waste streams such as flue gas as well as using nitrogen from the gas as a nutrient. Before microalgae can be converted into fuels, the biomass content has to be harvested and dried. The conversion can be carried out through thermochemical or biochemical conversion. The products synthesized depend on the algae or bacteria variety chosen and also on the operating conditions [21].
It is the use of biochemical agents, as enzymes, to stimulate a chemical reaction and, thus, obtain products by using less drastic operating conditions than in heterogeneous or homogeneous catalysis. Inspired by nature, a large body of research has been devoted to new materials catalyzing CO_2 functionalization in either electrochemical or chemical ways. In 2009, the U.S.-based start-up Carbon Science developed a prototype capable of producing liquid fuels. This demonstration system employed a proprietary biocatalytic process designed to decompose CO_2 and water, subsequently recombining the released carbon and hydrogen atoms to synthesize methanol, a liquid fuel [21].
Although this route is highly innovative and promising, the technology is still at laboratory scale and difficult to scale to industrial demand.

1.4.3 Electrochemical approaches

Thermochemical processes for CO_2 utilization, which typically rely on organic and inorganic solvents, are well-established and achieve high capture efficiencies. However, they are inherently constrained by their thermodynamics: negative reaction enthalpies necessitate high-temperature regeneration steps, resulting in significant energy consumption.

Electrochemistry emerges as a possible solution to these limitations. Rather than using heat that is generated by electricity, an alternative is to use directly the energy and properties of electricity to control and make the desired reactions happen. It operates under isothermal conditions, enhancing reversibility, improving overall energy efficiency, and ensuring safer process conditions. More importantly, electrochemical methods align directly with the ongoing electrification of industrial processes. As electricity from renewable sources becomes increasingly available, direct electrochemical utilization of CO_2, without intermediate conversion into heat or other primary energy carriers, minimizes efficiency losses and maximizes the sustainable use of renewable power.
Electrochemistry allows for CO_2 reduction reaction (**CO_2RR**) enabling the production of valuable hydrocarbons and oxygenates, including ethylene, methane, carbon monoxide (CO) making it more reliable alternative to traditional CO_2 conversions. These products are key actors for production of polymer material or fuel from carbon waste helping reduce the carbon footprint globally [22]. Particular interest is made on the production of CO. Beyond its direct market value, CO serves as a versatile feedstock for the production of value-added chemicals and can also be combined with H_2 to generate *syngas*. Syngas plays a crucial role in the Fischer–Tropsch process, enabling the synthesis of simple hydrocarbons and thereby synthetic fuels [23], which are of significant industrial relevance. However, electrochemistry faces many challenges: balancing costs and efficiencies in order to achieve large-scale feasibility, addressing these challenges is crucial for developing more effective strategies for this new technology.

1.5 Integrated Carbon Capture and Utilization

As of 2025, pure CO_2 gas-fed electrolyzers are now benchmarked and industrially used. They reach almost 100% selectivity of conversion into CO but require pressurized purified CO_2 from flue gasses. The purification process is extremely energy demanding making the overall process inefficient even if the electrolyzer has high selectivity, as discussed previously.
A promising alternative, is to bypass the desorption step altogether by directly utilizing CO_2 in its absorbed form, as captured by the solvent. This approach is known as the integrated carbon capture and utilization (ICCU) process. For instance, conventional amine-based capture systems require heating above 100°C to regenerate the solvent and release CO_2, which significantly raises the total energy consumption of the process [24]. By contrast, ICCU enables the direct use of captured CO_2 products as feedstocks for downstream reactions, thereby eliminating the need for energy-demanding gas recovery and compression. As illustrated in Figure 1.4, this integration allows the captured compounds to either be locally reconverted into gaseous CO_2 through mechanisms other than thermal desorption, or to participate directly in chemical transformations leading to value-added products. Such an integrated framework not only reduces energy penalties but also enhances the overall sustainability and industrial feasibility of CCU technologies.

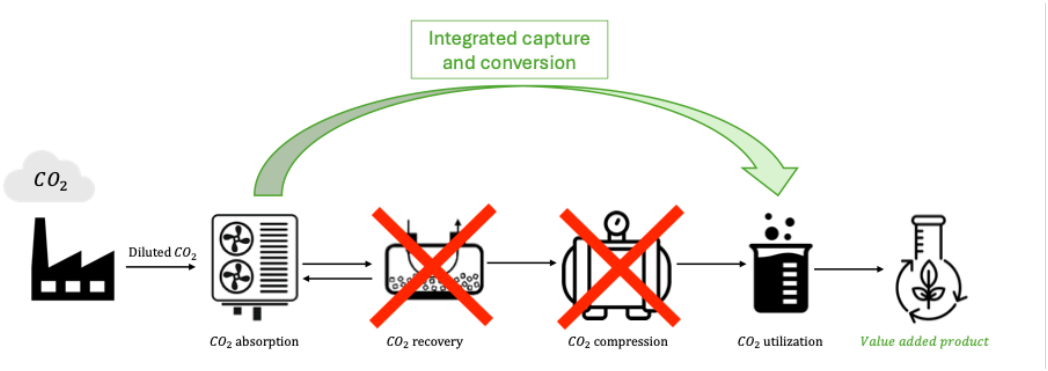

Figure 1.4: Schematic representation of an integrated CCU process

1.6 Aim of the Thesis

The present thesis investigates the development of efficient electrochemical ICCU components to address the critical challenges posed by greenhouse gas emissions, with particular focus on CO_2 emission. Electrochemistry is considered as a promising alternative to conventional CCU approaches, owing to its intrinsic scalability and operational modulability. In order to integrate the capture and conversion processes, a bicarbonate solution is adopted as the carbon feedstock. The experimental work is divided into two main parts. In the first part, an optimization study is conducted on silver (Ag)-based electrodes, selected on the basis of an extensive review of the existing literature. In perspective of a possible industrial scale-up, the study focused also on the impact of exterior parameters such as temperature and pressure. In the second part, a more detailed investigation is carried out on alternative low-cost and energy-efficient electrode materials, with the objective of identifying suitable substitutes for Ag-based systems.
The central focus of the thesis is the electrochemical conversion of CO_2 into carbon monoxide (CO), as CO represents the most profitable product of the CO_2-to-CO reduction pathway.

Chapter 2

Introduction to electrochemical CCU

This chapter discusses the fundamental principles of electrochemistry and their application in CCU and ICCU. The design and components of electrochemical cells are examined to describe the operating principles of electrolyzers and potential improvements.

2.1 What is electrochemistry?

The field of electrochemistry is vast and an important area of modern research, combining the studies of electricity and chemistry. Electrochemistry dates back to 1793, when Volta developed the first battery and discovered the connection between chemical reactions and electric current [25]. Building on his work, in 1800, Nicholson used Volta's battery to decompose water into hydrogen and oxygen, demonstrating electricity's ability to drive chemical reactions [26]. Following this discovery, Faraday demonstrated that there is a quantitative relationship between the amount of electricity consumed in an electrochemical reaction and the amount of electrolysis products, paving the way for more systematic studies of electrochemical reactions [27]. In essence, electrochemistry concerns the reaction of a chemical species at the interface between an electron conductor and an ionic conductor, involving charge transfer between the species and the electrode. The "electrode" is generally made out of metal or semiconducting material, while the ionic conductor termed "electrolyte" can be either solution based or solid based.
Electrochemistry is employed in a variety of applications such as energy production with solid state fuel cells, electrosynthesis with for example electroplating of metals on complex shapes but also selective corrosion [28].

In response to the growing global demand for energy and the urgent need for sustainable technologies, electrochemical systems have emerged as highly promising candidates for both energy conversion and storage. Their modularity, scalability, and capacity to operate under mild conditions make them particularly attractive for applications in clean energy and carbon management. A generic electrochemical cell, often referred to as an **electrolyzer**, consists of electrodes, an electrolyte, and catalysts, which together enable the exchange of electrons and the transport of ionic species. Through these processes, the electrolyzer drives the reduction or oxidation of reactants, leading to the formation of new chemical products [29].
Within this broader framework, CO_2 electrolyzers have gained increasing attention due to their ability to transform CO_2 into valuable carbon-based products via electrochemical reduction. Among the various configurations investigated to date, gas-fed electrolyzers have been identified as the most promising design. Their architecture allows for enhanced mass transport of CO_2 to the catalytic sites, improving reaction efficiency and product selectivity. Positioning

them as leading candidates for practical implementation of electrochemical CO_2 conversion technologies.

2.2 Electrochemical Carbon Dioxide Reduction Reaction

In this section are examined the components and designs of an electrolyzer and their influence on CO_2-to-CO electrochemical conversion. The following paragraphs will describe optimized designs for maximization of CO_2RR and efficiency, considering various catalysts and additives.

2.2.1 H cell

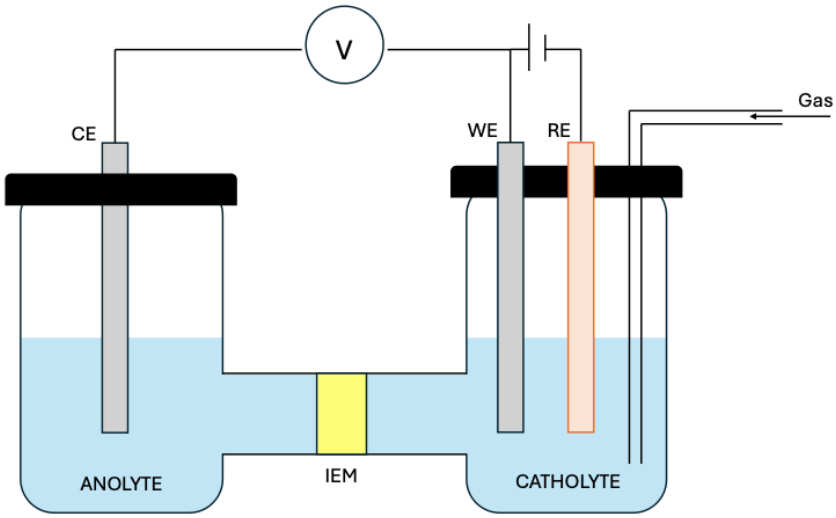

Figure 2.1: Schematic representation of a H-cell, anolyte and catholyte exchanging ions through an IEM (Ion Exchange Membrane) where tension is applied to electrodes (CE: Counter Electrode, WE: Working Electrode, RE: Reference Electrode

The H-cell is the simplest electrolyzer structure widely used in electrochemical research to understand the dynamics and reactions occuring inside the cell. It is composed by: anode and cathode placed in two compartments separated by an Ion Exchange Membrane (IEM). The membrane prevents the mixing of products formed at each electrode while allowing specific ion transfer between the two compartments. (Figure 2.1) Typically the cell is made out of glass containers filled with the studied electrolyte [30].
Three electrodes compose the setup: the working electrode (WE), the counter electrode (CE) and the reference electrode (RE). The WE features the studied catalyst and the reaction of interest occurs. The CE is placed in the opposite compartment closing the circuit and showing complementary reaction (oxidation or reduction). The RE is situated near the WE measuring the potential and isolating the reaction from the rest of the setup maintaining a stable and reproducible potential for precise measurements [31].
In CO_2RR studies, CO_2 gas is bubbled to keep the electrolyte saturated.

At the catalyst-coated cathode, CO_2 can be electroreduced to different products. The similarity

of reductive potentials for all each reaction pathways, shown in Table 2.1 in neutral conditions creates a competitiveness between CO_2 reduction and hydrogen evolution at the cathode side [30]. SHE stands for *Standard Hydrogen Electrode* which is a reference for electrochemical reactions and is obtained with a Reference Electrode (RE) (Figure 2.1).

Table 2.1: Occurring reactions in an electrochemical cell at pH 7 (adapted from [32] [33])

Reaction	E *vs.* SHE (V)
$2H_2O + 2e^- \rightarrow H_2 + 2OH^-$	0
$CO_2 + 2H_2O + 2e^- \rightarrow HCOO^- + OH^-$	-0.61
$CO_2 + H_2O + 2e^- \rightarrow CO + 2OH^-$	-0.52
$CO_2 + 3H_2O + 4e^- \rightarrow HCHO + 4OH^-$	-0.89

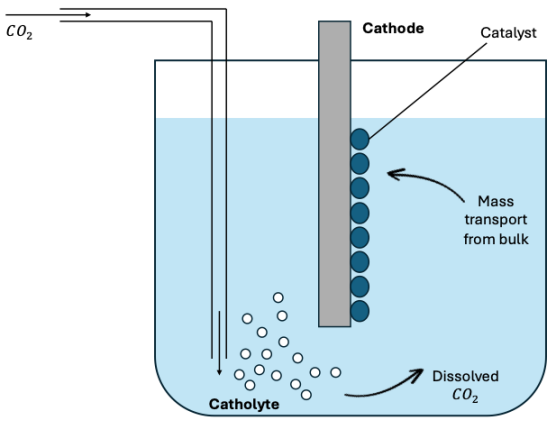

Figure 2.2: Cathodic compartment of an H-cell. Dissolved CO_2 in the electrolyte undergoes the CO_2RR when it reaches the catalyst-coated cathode surface.

In an H-cell setup the CO_2 is bubbled in the catholyte, considering it being a water-based solution it can be assumed that it is mainly water. Gaseous CO_2 has an extremely low dissolution in water of *34 mmol/L*, only the CO_2 dissolved in the catholyte can be reduced, making the electrochemical process highly inefficient (Figure 2.2). Furthermore, the H-cell compartments are voluminous, implying that there is also a mass transport limitation from the bulk solution to the interface with the electrode.The limited solubility of CO_2 in aqueous electrolytes, combined with the complexity of mass transport phenomena, necessitates the use of relatively low current densities in order to maintain high CO_2RR selectivity. At high current densities, mass transport limitations become more significant, promoting the HER (Hydrogen Evolution reaction) over CO_2RR.

Given its simple design, the H-cell is used for fundamental electrochemical works. Its well-controlled environment allows the study of catalysis but also material stability. It is used for basic electrode behaviour and understanding the reaction mechanisms.

2.2.2 Electrocatalyst

The electrocatalyst material is the functional core of the electrode, providing the active surface where reactant molecules undergo electrochemical transformation. Its properties have an essential role, governing the reaction pathways according to its nature. Different catalyst materials favor different mechanisms, varying the electrode's selectivity for specific products. Achieving high selectivity toward CO is of particular importance, given its value as both a feedstock for chemical synthesis and a precursor for syngas production. Catalyst performance can be further enhanced through targeted modifications, such as tuning interactions with the support or optimizing charge transfer properties, ultimately improving activity, selectivity, and stability [34].

When a reductive potential is applied to the system, strong interactions between the ions/solvent molecules and the electrocatalyst surface are observed. The surface of the cathode has a negative charge, generating a region of adsorbed ions of opposite charge, then a diffuse layer of charges around the surface that goes into the bulk solution [35].
Under CO_2RR conditions, when a CO_2 molecule adsorbs onto an electrode surface [36], it binds to the surface through chemisorption, which involves electron redistribution and the formation of a chemical bond. Discussion on how CO_2 binds to a catalyst surface is helpful in understanding the chemisorption process, which often is the first elementary step of the CO_2RR. The highest occupied molecular orbital (HOMO) and the lowest unoccupied molecular orbital (LUMO) of CO_2 are $1\pi g$ and $2\pi u$, respectively [37]. Both the relative order as well as the absolute HOMO and LUMO energy levels greatly influence the adsorbate-surface chemistry. Furthermore, chemisorption is highly directional, like all chemical bonds. Consequently, chemisorbed adsorbates (chemisorbates) adhere to specific sites, and this binding interaction strongly depends on their orientation with respect to the surface.

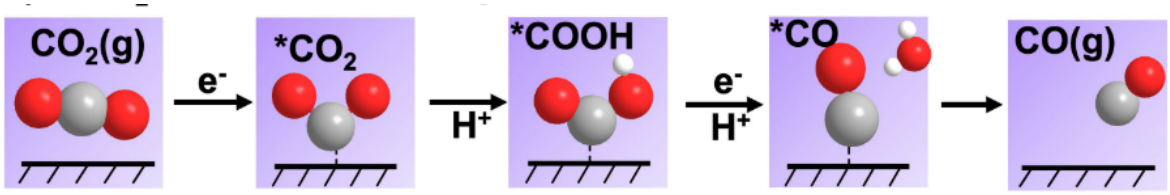

Figure 2.3: Proposed mechanism for which the CO_2 is bound to the catalyst surface leading to the production of CO [38]

The chemisorbed molecule shows a bend configuration due to the donation of electrons and acceptance from electronic levels creating hybrid electronic states [39]. The C end down configuration, as shown in Figure 2.3, is preferred for the CO and hydrocarbon-producing electrocatalysts, based on the fact that the overlap of both $1\pi g$ and $2\pi u$ orbitals with the metal states is most favored by a linear geometry, and the carbon center is electrophilic. From this configuration, CO_2 reacts with protons and electrons while bonding with the surface, this generates CO bonded on the surface that is released in gas form [38].

The majority of existing CO_2 reduction reaction electrocatalysts can be divided in three groups: metallic, non-metallic and molecular catalysts, as shown in Figure 2.4.

Monometallic catalyst

Monometallic electrocatalysts have been extensively studied, demonstrating high product selectivity and commercial availability compared to other catalyst types. Considering that the

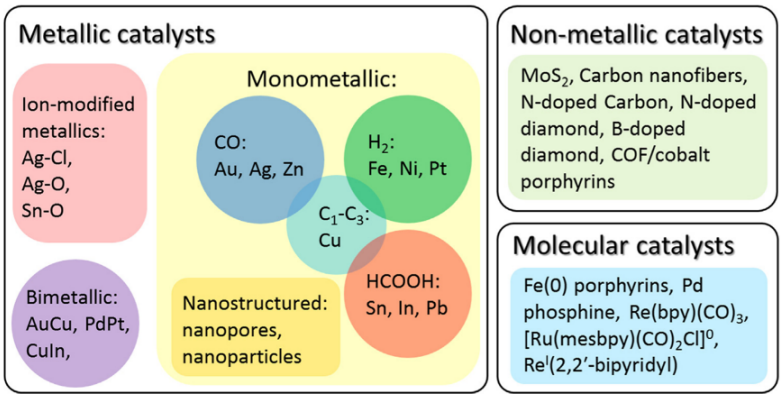

Figure 2.4: Classification of electrocatalysts for CO_2RR into metallic, non-metallic, and molecular categories [40]

interaction between the ions in solution and the catalyst is made at their interface: maximizing the catalyst's surface maximizes the interaction with the reactant. Nanostructured materials provide much more surface-active sites than bulk materials because of their enhanced surface areas. They also expose many edge or low-coordination sites, which can behave very differently from the flat, fully coordinated surfaces found in bulk materials [40]. For these reasons most of commercial electrocatalysts are made out of **nanoparticles of monometallic material**.
Concerning the CO_2-to-CO electroconversion, Au, Ag and Zn based catalyst are now benchmarked [41]. Oxyde derived catalysts are obtained from intensional cycles of oxidation and reduction of metallic electrodes showing improvements from bulk metal electrode having more active sites on the surface but complex to control reactions. Non metallic catalyst show good conversion rates of CO_2 to CO but are extremely expensive to produce. Finally molecular catalyst have very complex structure but thanks to their tuneable nature they can be modified for major selectivity.

Single-Atom Catalyst

Instead of relying on nanostructured metal surfaces, single-atom catalysts (SACs) can be used as an alternative. These catalysts are composed of a single metallic atom, such as Cobalt or Iron, surrounded by an organic compound, and is capable of catalyzing reactions via a redox reaction. The metal atom serves as the catalytic center, while the surrounding organic framework facilitates electron transport during electrochemical reduction. The organic framework can be modified to interact with specific groups of the support or of the reactant molecule [42].
Many noble materials (Ag, Au, Pt) show high selectivity and catalytic activity, however the scarcity, high cost, and possible losses in the reduction process of precious metals limit their large-scale application [43] [44]. As an abundant transition metal with catalytic properties, **cobalt** is recommended as one of the most promising ideal substitutes for noble metals [45]. Cobalt is a group VIII element, which is readily available in its oxidized state (Co^0, Co^I, Co^{II}, Co^{III}, Co^{IV}). CO_2RR mediated by cobalt catalysts typically involves a Co^{II} to Co^I intermediate state transition. Among the class of cobalt-based materials, Cobalt Phthalocyanine (CoPc) (Figure 2.5) is the most attractive showing easy accessibility, chemical stability and structural tuning at a molecular level.[46].

Theoretically, CoPc exhibits superior CO formation activity due to the moderate binding energy of *CO at the Co site. Figure 2.6 illustrates the mechanism of electrocatalytic CO_2RR to CO via CoPc [47]. It's important to note that both the mechanism and the reac-

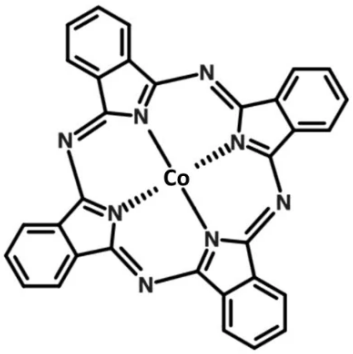

Figure 2.5: Molecular representation of a Cobalt Phthalocyanine (CoPc) having a Cobalt metal site bonded with Van Der Waals forces to Nitrogen of the aromatic rings.

tion rate-determining step (RDS) of the CO_2RR via CoPc are slightly different under high ($>$ 0.3 M) and low ($<$ 0.3 M) bicarbonate conditions. The RDS at low bicarbonate concentrations involves electron transfer, while that at high bicarbonate concentrations involves concerted proton-electron transfer.

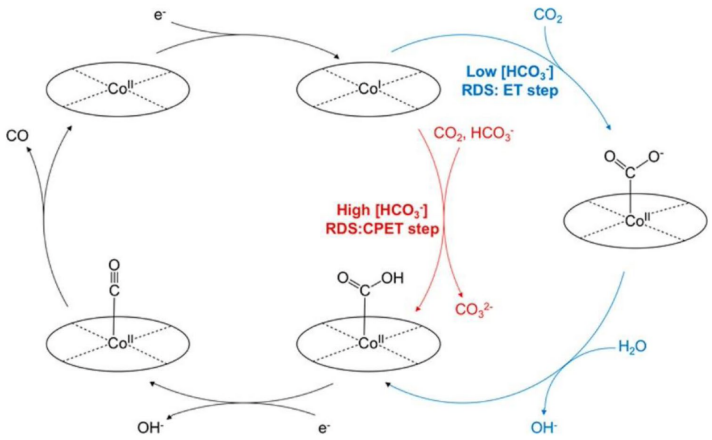

Figure 2.6: Proposed mechanism for CO_2RR with CoPc catalyst. Comparison between low bicarbonate (blue) and high bicarbonate conditions (red), higher bicarbonate lead to less catalytic steps. [47]

In low bicarbonate concentrations ($<$ 0.3 M), there is an electron transfer and a following reaction with water. While in high bicarbonate concentrations ($>$ 0.3 M) it is observed a Cooperative proton-electron transfer (CPET) creating a carbonate ion, as shown in equations (2.1 - 2.4).

$$Co^{II}Pc + e^- \rightarrow Co^{I}Pc \tag{2.1}$$

$$RDS : Co^{I}Pc + CO_2 + HCO_3^- \rightarrow Co^{II}Pc - COOH_{ads} + CO_3^{2-} \tag{2.2}$$

$$Co^{II}Pc - COOH_{ads} + e^- \rightarrow Co^{II}Pc - CO_{ads} + OH^- \tag{2.3}$$

$$Co^{II}Pc - CO_{ads} \rightarrow Co^{II}Pc + CO \tag{2.4}$$

Compared to noble metals, transition metals interact with the reacting species by showing different oxidized states. In the case of CoPc, $Co^{(II)}$ is the stable compound while $Co^{(I)}$ is the active one. Upon adsorption of CO_2 or bicarbonate there is a transition from (I) to (II), and

electrons facilitate a transition (II) to (I). To ensure catalytic activity, current is required not only for CO_2RR reactions but also to regenerate the Cobalt.
From its organo-metallic nature, pure CoPc exhibits strong agglomeration of molecules when deposited. This represents an important limitation reducing the efficiency of the catalyst due to its poor dispersion [48].

2.2.3 Hierarchically designed Single Atom Catalysts

From the aggregation tendency of SACs and chemical structure results in a lower density of active sites than conventional metallic benchmark catalysts. A possible strategy is to integrate organometallic compounds with electronically conductive carbon supports. In these hybrid systems, the conductive scaffold not only facilitates efficient electron transport to the active sites but also provides a high surface area platform for dispersing the molecular catalysts, preventing aggregation and maximizing accessibility. Thanks to strong $\pi - \pi$ interactions between the aromatic structures and the carbon lattice, organometallic molecules such as CoPc are anchored to graphitized materials, enhancing the stability of the active sites. This hierarchical catalyst design enables synergic effects in which the molecular-level catalytic centers are coupled with nanoscale conductive networks, resulting in improved activity and selectivity for CO_2RR.

Interaction with graphitized materials

CoPc is a planar conjugated molecule with agglomeration tendency, resulting in a low utilization of molecular catalysts [49]. Carbon materials with excellent conductivity and high surface area (graphene, Carbon Nano Tubes (CNT), Carbon Black (CB)) are usually employed as supporting material [50]. Graphitized materials show Carbon hybridization sp^2 allowing them to generate double covalent bonding creating hexagonal aromatic structures. These structures are characterized by a delocalized π electrons cloud, allowing them to bond easily with other similar organic structures.
The carbon materials with a high graphitization degree, such as CNTs, were found to be able to improve the SAC efficiency. CoPc's outer organic structure is rich in aromatic rings with sp^2-hybridized carbon atoms (Figure 2.5), which facilitate efficient electron transfer. These rings can interact with the aromatic surfaces of carbon materials via Van der Waals $\pi - \pi$ stacking non-covalent interactions between delocalized π-electron systems (Figure 2.7). This interaction ($\sim$2 kcal/mol [51]) can modulate the electronic density on the catalyst surface, promote CO_2 molecule adsorption, or stabilize intermediates, thereby enhancing the reaction selectivity and catalytic efficiency of CO_2RR [52] [53].

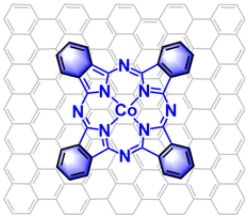

Figure 2.7: Schematization of $\pi - \pi$ stacking of CoPc on a perfect graphitized surface. [54]

The choice of CNTs and CB for the case study emerges from their commercial availability and efficiencies. The ideal choice is graphene but it is a sensible and expensive material to work with [55]. Multi Walled CNT (MWCNT) are the most available type of CNT, obtained by

a graphene layer closed on itself. MWCNT are highly graphitized surfaces arranged in concentric tubes (Figure 2.8a). They exhibit high electron conductivity and structural integrity. Alternatively, CB is an agglomeration of spherical primary particles with sizes between 10-100 nm. The spherical particles show graphitic and amorphous structures, composed of turbostratically stacked carbon polyaromatic layers. These structures are also known as "basic structural unit" (BSU). Lacking three-dimensional ordering, the term "crystallite" isn't strictly correct. The BSU show a concentricic orientation around the amorphous core creating a "onion-like" structure (Figure 2.8b) [56].

(a) MWCNT (b) Sketch of CB primary particle [57]

Figure 2.8: Schematic representation of tubular MWCNT structure and of onion-like CB BSU ordering.

MWCNT and CB are a prime example of the diversity of carbon materials and how changing specific properties and stacking of graphitic layers change materials properties. MWCNT showcase more order and conductivity, while CB doesn't show long-range order but has higher superficial area. Depending on which material is selected as the carbon support, the properties of the supported catalyst will vary.

Hierarchically designed catalysts

Supported catalysts made of organometallic compound and carbon scaffold are defined as hierarchically designed catalyst. The hierarchical effect is observed when phenomenas at a larger scale are consequence of interactions at a smaller scale. At the molecular scale, the π–π stacking between the aromatic macrocycles of the organometallic compound (CoPc) and the graphitic lattice facilitates electronic coupling, enabling efficient charge delocalization and redistribution of electronic density across the interface. This structural feature enhances the stabilization of atomically dispersed active sites while promoting strong interactions with CO_2. This facilitates its activation and improves CO_2RR activity, even at low CO_2 concentrations.
Traditional monometallic catalysts exhibit weak adsorption capability due to their inherent metallic nature. The high conductivity leads to the formation of a surface charge on the electrocatalyst, enabling charge-based interaction with ions. Most importantly, water, as a polar molecule, is also attracted to the charged surface, limiting the number of active sites. Additionally, the accumulation of OH^- near the catalyst surface forms a CO_2-consuming boundary layer that limits mass transfer and restricts access of CO_2 to the active sites (Figure 2.9).

On the other hand, hierarchically designed single-atom catalysts such as CoPc immobilized on graphitized supports exhibit stronger binding with CO_2. This enhancement leads to improved both activation and subsequent conversion efficiency. The robust CO_2 adsorption capability of these supported catalysts ensures more effective utilization of CO_2 in limited concentration conditions. To further mitigate mass transport limitations, a cross-flow electrolyte configuration

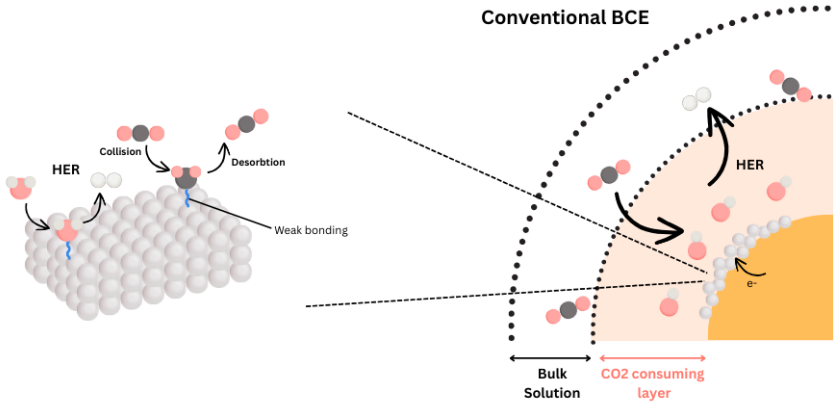

Figure 2.9: Schematization of interaction of H_2O and CO_2 molecules on an Ag catalyst surface generating a CO_2-consuming layer limiting CO_2RR. Adapted from [58]

is used, which continuously removes the CO_2-consuming layer and facilitates more efficient diffusion of CO_2 to the active catalytic centers (Figure 2.10) [58].

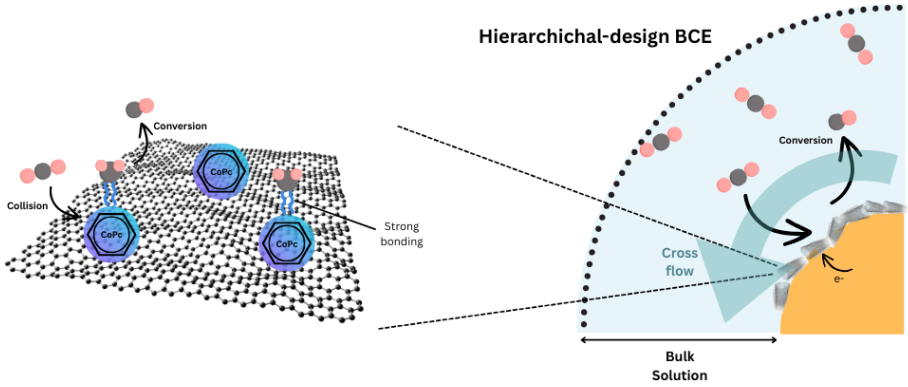

Figure 2.10: Schematization of interaction of H_2O and CO_2 molecules on a hierarchically designed CoPc@CNT catalyst surface removing the CO_2-consuming layer with a cross-flow of electrolyte.Adapted from [58]

Organometallic compounds and graphitized support cost less than traditional monometallic catalysts. Combining reduced costs consideration and the high effectiveness observed in gas-fed electrolyzer: hierarchical designed catalysts have potential to become a low-cost energy effective alternative to traditional monometallic based catalysts in electrolyzers.

2.2.4 Electrolyte

In electrochemistry, reactions occur at reaction sites and the charges are transfered to the electrode by two mechanisms: electron flow via external circuits (electronic conduction) and ion movement through electrolyte (ionic conduction). To maintain neutrality of the cell, negatively charged electrons traveling between electrodes initiate reactions, while positively charged ions (cations) migrate through the electrolyte toward the negative electrode. Similarly, negatively charged ions (anions) move toward the positive electrode, ensuring electroneutrality at both electrodes. This charge movement is crucial for the efficient operation of electrolyzers, and enhancing conductivity is a key strategy for improving their performance [59].

The role of the electrolyte is to ensure a good conductivity of dissolved ionic species. The efficiency of an electrolyte stands in the freedom of movement of the charged particles, these electrolytes are obtained from dissolution of salts in solvents like water that break the crystal lattice releasing ions. For example the dissociation of NaCl in water creating Na^+ and Cl^-, overall the system is neutral but positive and negative charges are released in water to enable conduction.

2.2.5 Ion Exchange Membrane

The role of an ion exchange membrane is to allow the flow of specific ions. In this way it is possible to separate the processes occurring at anode and cathode, while ensuring the conductivity between the two compartments. According to literature three different types of IEMs are used for CO_2 electrolyzer: Cation Exchange Membrane (CEM), Anion Exchange Membrane (AEM) and Bipolar Membrane (BPM). Ion exchange membranes achieve selective ion transport based on their chemical composition and electronic properties, rather than physical characteristics. The flow of ions is given by hopping of the charge from an electrically charged site of the polymer to another on the carbon chain [60].
Typical CEMs are made from polymers containing strong electronegatively charged atoms in the chain, allowing a cations transport and a rejection of anions. The most widely used commercial CEM is Nafion™, shown in Figure 2.11a . Its fluorine, oxygen, and sulphur atoms create a strong electronegative contrast with the carbon backbone, enabling efficient proton transfer from the anode to the cathode. On the other hand, AEM are used to transport anionic species. They are typically made by positively charged group rejecting cations. Their structures are functionalized polymers with positively charged groups such as $-NH_3^+$ with a backbone of polystyrene. The most widely used commercial AEM is Sustainion™ shown in Figure 2.11b.

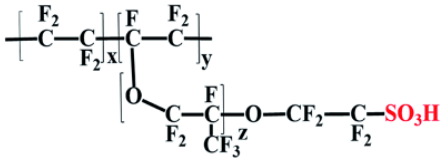

(a) Nafion

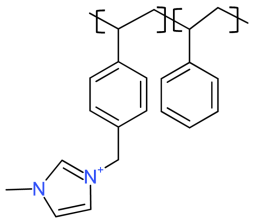

(b) Sustainion

Figure 2.11: Examples of widely used ion exchange membranes: (a) Nafion (CEM) and (b) Sustainion (AEM)

Figure 2.12 from the works of Pärnamäe et al. (2021) [61] schematizes the discussed working principle of BPM. A BPM is made by combining a CEM and an AEM pressed onto one another. In reverse-biased mode, the cation exchange layer (CEL) faces the cathode, while the anion exchange layer (AEL) faces the anode, thereby promoting the water dissociation reaction at the interface between the two layers. The CEM, containing fixed negatively charged groups, selectively facilitates the transport of protons, whereas the AEM, with fixed positively charged groups, enables the transport of hydroxide ions. Under the applied electric field, water molecules at the interfacial junction undergo heterolytic cleavage, generating H^+ ions that migrate through the CEL toward the cathode and OH^- ions that migrate through the AEL toward the anode. The efficiency of this process is influenced by the ion-exchange capacities of the individual membranes and the catalytic properties of the interface, which reduce the over potential for water dissociation. Commercially, FumaTech™ produces BPMs that integrate these

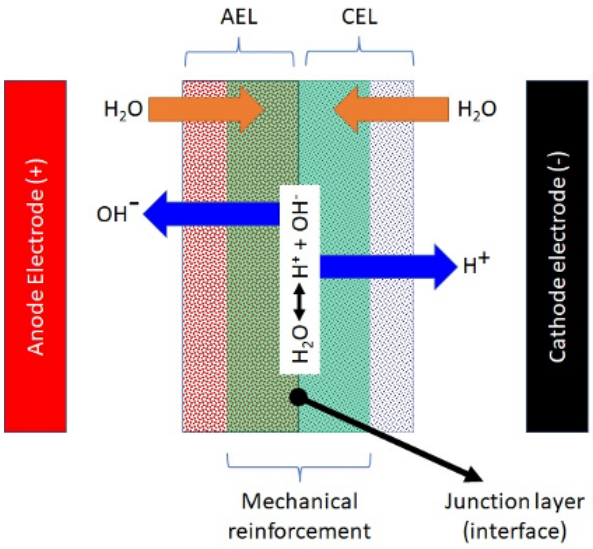

Figure 2.12: Working principle of a BPM. Water permeates through the membrane interface and dissociates into H^+ and OH^- ions, which migrate to separate compartments.

design principles, providing spatially separated acidic and basic streams for electrochemical applications.

2.2.6 Polymeric binders

Polymeric binders, also known as ionomers, have a role of binding the catalyst nanoparticle once deposited and perform several critical roles within the catalyst layer. These polymers act as surfactants during ink preparation, helping to uniformly disperse the catalyst in solvents suitable for deposition onto porous substrates. More importantly, binders facilitate ionic conduction within the catalyst layer, enabling the transport of either anions or cations depending on their ionic nature [62].
One of the primary benefits of binders is their ability to regulate electrode wettability, which plays a crucial role in determining CO_2RR selectivity. Hydrophobic binders reduce electrode wettability, thereby maintaining an optimal CO_2/H_2O ratio near the catalyst surface. This suppression of excessive water coverage minimizes the competitive HER and promotes CO_2RR selectivity towards valuable carbon-based products.
Commercially available binders are ionomers already cited in section 2.2.4 sold in an ethanol solution. Anion-conducting binders (such as Sustainion ™ or PiperION ™) primarily transport hydroxide ions (OH^-), while cation-conducting binders (such as Nafion™) transport protons (H^+). This ionic selectivity directly influences the local pH within the catalyst layer, which in turn significantly impacts the selectivity of the CO_2RR. In gas-fed electrolyzers, this pH control is critical, as it affects the competition between CO_2RR and the HER, ultimately steering product distribution [63].

2.2.7 Control Parameters

In electrochemical cells important parameters need to be defined, these control parameters are comparative tools between different setups. They quantify specific electrochemical properties and help identify the problematic systems.

Faradaic Efficiency
The **Faradaic Efficiency** (FE) is often used to describe how many electrons contribute to a desired reaction, it gives a measure of the selectivity of the electrochemical process. It is define as the fraction of the total charge flowing through the electrode and the charge used to produce a specific product expressed in percentages:

$$(FE)_{product} = \frac{\chi nF}{Q} \tag{2.5}$$

Where χ represents the number of mols of the product, n is the number of electrons transferred per mol of product, F is the Faraday constant (96485 C/mol) and Q is the total charge flowing in the system. [64]

Current Density
The **Current Density (CD)** is the total current (I) per unit of area (A) of the active area at a given potential:

$$CD = \frac{I}{A} \tag{2.6}$$

The current density is influenced by the type of electrocatalyst and the mass transport of reactants and products to and from the electrode. The partial current density can be obtained combining FE and CD giving us information about the speed of reaction of a specific product. A fundamental parameter to evaluate the dimensions of the electrolyzer and the cost-efficiency ratio.

$$j_{product} = (FE)_{product}.CD \tag{2.7}$$

High current density indicate an high reaction kinetic, while high partial current densities (of a single product) show how much current is used for a single product. Maximizing current density is essential to minimize the physical size of the electrolyzer and improve space efficiency.

2.3 Membrane Electrode Assembly

H-cell setups are not scalable exhibiting very low efficiency and primarily serve to determine whether the catalyst on the cathode surface is active for CO_2 reduction. To enable the scale-up of the CO_2 electroreduction process, a different cell configuration is employed, known as the Membrane Electrode Assembly (MEA). In this setup, the internal structure consists of an IEM sandwiched between the anode and cathode. At the cathode, a gas diffusion electrode (GDE) is used, typically composed of a porous carbon paper support coated with the catalyst. The GDE facilitates efficient gas-phase CO_2 delivery directly to the catalyst surface, enhancing mass transport and overcoming the solubility limitations present in aqueous-phase systems. At the anode, the oxygen evolution reaction (OER) takes place, serving as the counter-reaction to maintain charge balance and provide the protons or hydroxide ions required for the CO_2 reduction process. This cell design enables higher current densities and improved energy efficiency, making it more suitable for industrial-scale applications. In Figure 2.13 it is shown that at the anode water flows and is transported inside the membrane creating a thin layer of water at the interface with the cathode. At the cathode, the gaseous CO_2 flows and reaches the thin water layer where it is dissolved and reacts with the catalyst.
This type of setup is also called zero-gap cell highlighted by the contact between all components. Reducing the amount of water mitigates mass transport limitations, enabling the MEA to operate efficiently at higher current densities and increasing selectivity for CO production. In

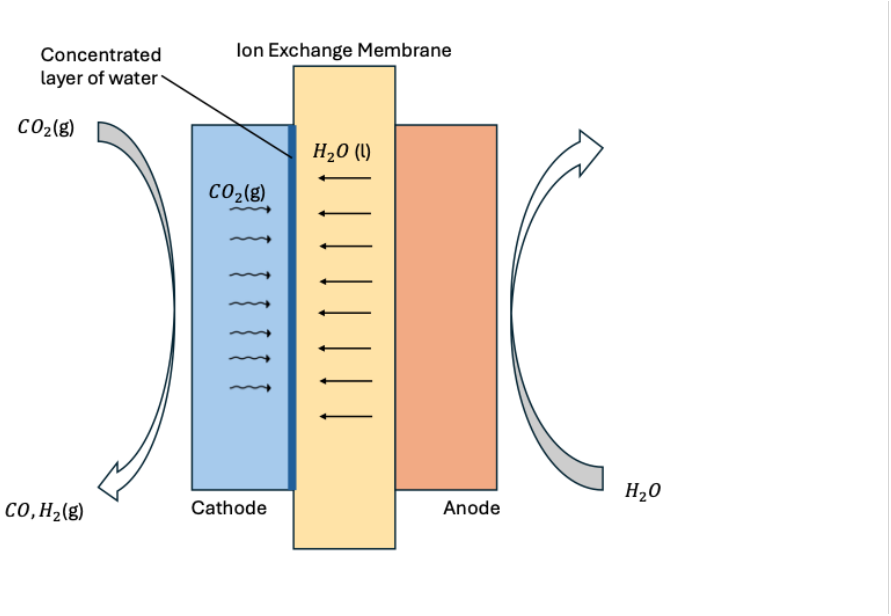

Figure 2.13: Schematic representation of transport of H_2O and CO_2 inside a MEA setup between anode and cathode

MEA-based CO_2 electrolyzers, higher local pH levels can be achieved, especially when using an AEM. The CO_2RR is known to be more efficient and selective toward desired products, such as CO, under alkaline conditions. The use of an AEM facilitates the transport of hydroxide ions (OH^-) from the cathode to the anode, leading to the accumulation of OH^- near the cathode surface. As a result, the local environment becomes more basic, creating optimal conditions for enhanced CO_2RR performance in gas-fed electrolyzer systems. Thanks to this setup, MEA-based systems achieve greater energy efficiency, primarily due to minimized ohmic losses and high selectivity at high current densities.

2.4 Reactive Carbon Capture

Until now only electrochemical setups using pure gaseous CO_2 have been reviewed. As mentioned in Section 1.4, carbon capture technologies used specific solvents such as amine-based absorbent that require a thermal step regeneration step to release CO_2 gas captured to be used. Current state-of-the-art amine capture systems require over 3.5 GJ/ton CO_2 to capture and release CO_2, making them highly energy-intensive and inefficient.In the broader context of electrifying chemical manufacturing and minimizing reliance on thermal processes, the direct electrochemical conversion of CO_2 using renewable electricity presents a highly attractive pathway. Unlike conventional thermochemical methods that require converting electricity into heat, an energetically inefficient step, electrochemical approaches allow for direct utilization of electrical energy without the intermediate transformation of a primary energy source. Considering the substantial energy losses associated with converting electricity into heat, such thermally driven processes become increasingly undesirable in a sustainable and energy-efficient future.
An alternative solution to bypass the thermal step is through the use of **Reactive Carbon Capture**. By altering the pH of a bicarbonate solution inside a CO_2 electrolyzer, it is possible to integrate the capture and the conversion in a single step. The reactive carbon capture is possible thanks to the so called **bicarbonate electrolyzer** [65]. Figure 2.14 highlights the reduced number of steps and the removal of energy consuming steps with regeneration of the solvent

without use of temperature.

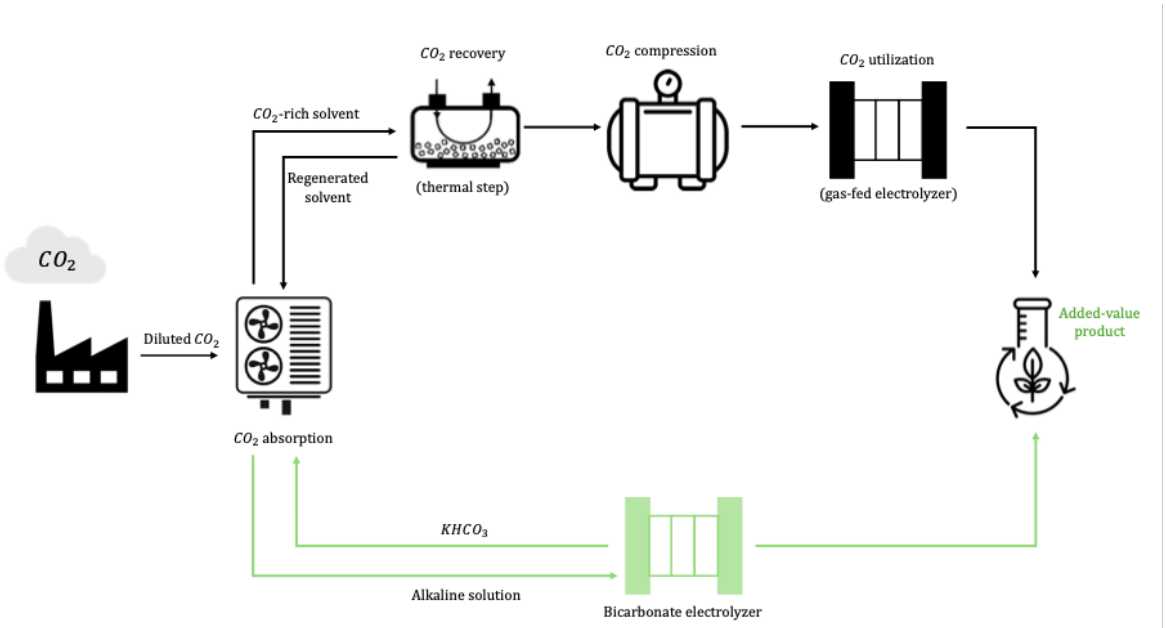

Figure 2.14: Comparison of traditional gas-fed CCU and reactive carbon capture (RCC). RCC eliminates the thermal regeneration step and simultaneously regenerates the capture solvent.

2.4.1 pH swing-based carbon capture and release

In an integrated carbon capture and valorization process through electrochemistry, the electrolyte will be directly the capture solution. The selection of the correct electrolyte has an important role in the optimizaton of high efficiency electrochemical convertion.
The main challenge for water based electrolytes is the low solubility of CO_2 in water under standard laboratory conditions, i.e. 34 mmol/L [66].
pH plays a critical role in both reactive carbon capture and the electrochemical reduction of CO_2, as it directly influences the speciation and solubility of carbonate-based ions in solution. The pH value reflects the balance between positive (H^+) and negative (OH^-, anionic species) concentrations in the solution. This relationship is effectively illustrated in the Bjerrun plot (Figure 2.15), which shows the relative concentrations of different dissolved inorganic carbon species, CO_2(aq), bicarbonate (HCO_3^-), and carbonate (CO_3^{2-}), as a function of pH. The Bjerrum plot is essential for understanding how CO_2 behaves in aqueous environments, particularly in bicarbonate-based solvents used in reactive carbon capture. At moderate pH values (around 6.3 to 10.3), bicarbonate (HCO_3^-) is the dominant species, making it highly soluble and thus ideal for transporting captured CO_2 in ionic form. As the pH increases further, the equilibrium shifts toward carbonate (CO_3^{2-}), reducing the concentration of bicarbonate ions. Conversely, at lower pH, more CO_2 is recovered in its molecular form.

From the Bjerrun plot, if the pH is reduced locally in a bicarbonate electrolyzer CO_2 would be directly in gaseous form inside the electrolyzer. Controlling the pH swing inside the cell controls the release of gaseous CO_2 directly and the possible reactions that occur. In acidic conditions CO_2RR isn't favourable compared to HER necessitating a tailoring of the pH levels guaranteeing low pH for CO_2 gas release and higher pH at the catalyst for CO_2RR.

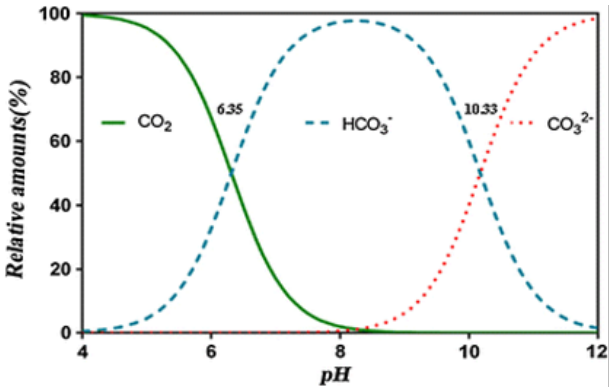

Figure 2.15: Bjerrum plot showing bicarbonate ion concentrations as a function of pH [67]

A great strength of bicarbonate electrolyzer is the possibility of regeneration during the conversion: CO_2RR in neutral solutions produces OH^- ions increasing pH during the process leading to a basic solution ready for new carbon capture. The feasibility of this process closes the carbon loop and sustainable, the liquid used for capture is converted and regenerated for new capture of CO_2 [68] .

2.4.2 Bicarbonate electrolyzer

In this subsection, a more detailed description of the structure and the composing elements of a bicarbonate electrolyzer is provided.
The optimum cell design for a bicarbonate electrolyzer is a **MEA-based zero gap cell** [69].
The electrolyte circulation is ensured by a pump which continuously renews the anolyte and catholyte at the respective electrodes. Each electrode is equipped with a flow field, typically a serpentine channel pattern, through which the electrolyte is distributed uniformly across the entire surface of the electrocatalyst and membrane within the MEA. Serpentine flow fields promote effective contact between the liquid electrolyte and the reactive surfaces, optimizing mass transport and reaction efficiency. While operating a high current, the current distribution along the flow field is not uniform [70]. Such inhomogeneities can reduce performance, lower reactant utilization, and starvation processes in the cell. Among the processes that can cause a non-uniform downstream current distribution are: (1) gas depletion along the flow field; (2) accumulation of water along the flow field; and (3) insufficient electrolyte supply [71].

Shown in Figure 2.16, the MEA constitutes the electrochemically active region of the cell, where the key redox reactions take place. Specifically, the cathode facilitates the electrochemical reduction of CO_2RR, while the anode drives the oxygen evolution reaction (OER). These reactions occur at the interfaces between the electrolyte, membrane, and electrodes, which are equipped with dedicated electrocatalysts tailored to each half-reaction. Eliminating the gap between electrodes significantly shortens ion transport distances, resulting in lower internal resistance and improved energy efficiency. Additionally, the close contact between the electrodes and the membrane allows for high reactant concentrations at the catalytic interface, particularly under pressurized conditions, which enhances reaction rates and current densities. The design is also highly scalable, making it well-suited for industrial applications such as electrochemical reactors. The fabrication of MEAs typically follows two main approaches: *Catalyst-Coated Substrate* (CCS), where the catalyst is deposited onto the porous electrode, and *Catalyst-Coated Membrane* (CCM), where the catalyst is directly coated onto the membrane surface [69].

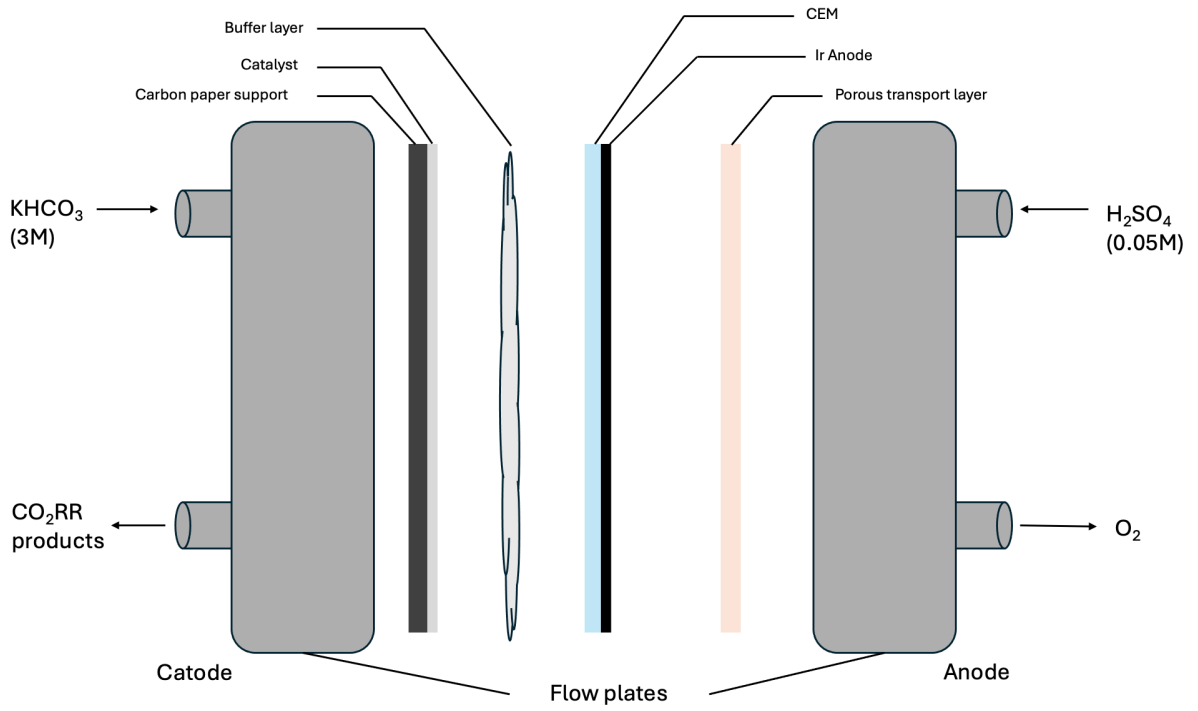

Figure 2.16: Schematic representation of a zero-gap electrochemical cell employing a MEA for CO_2RR

CEM

Within the MEA, dissolved CO_2 is regenerated into gas using the pH-swing in acidic conditions (equation 2.8) by the interaction between bicarbonate and protons. This condition is obtained with the CEM transporting protons from anode to cathode creating a proton accumulation at the membrane interface lowering the pH level. According to the Bjerrun plot the CO_2 is released as gas and having contact between membrane and catalyst the CO_2 undergoes CO_2RR.

$$HCO_3^- + H^+ \rightarrow CO_{2(g)} + H_2O \tag{2.8}$$

The CEM is fundamental to obtain the specific local acidic pH releasing CO_2 gas to be reduced at the cathode.

Gas Diffusion Electrode

Unlike gaseous CO_2-fed systems, bicarbonate electrolyzers rely on the in situ generation of dissolved CO_2 from bicarbonate (HCO_3^-) near the catalyst surface. GDEs are typically porous, multi-layered structures that facilitate efficient transport of reactants and products while ensuring optimal contact between the catalyst, electrolyte, and membrane.
Catalyst-Coated Substrate (CCS): the CCS cell design involves a catalyst layer deposited directly onto a porous substrate, which is compressed onto either side of the membrane. The substrate acts as both the current collector and the Gas Diffusion Layer (GDL), and can take different forms [72]. More recent research has involved a variety of different substrates and geometry, including porous carbon paper and porous nickel foam [73]. GDLs distribute the electrolyte from the flow plate and efficient removal of gas products.
Catalyst-Coated Membrane (CCM): the catalyst layer is directly coated onto the membrane surface. This approach minimizes interfacial losses and improves catalyst–membrane contact,

but it may pose challenges in terms of mechanical stability and uniformity of catalyst loading. In both cases, the design of the GDE is critical for maximizing CO_2 availability at the reaction interface, enhancing ionic conductivity, and maintaining electrode wetting properties under liquid-phase operation typical of bicarbonate systems.

Buffer layer

In bicarbonate-based electrolyzers, a key challenge is reconciling the conflicting pH requirements of two interconnected processes: the CO_2RR, which operates optimally under alkaline conditions, and the regeneration of molecular CO_2 from bicarbonate ions (HCO_3^-), which occurs in acidic environments (Figure 2.17). To overcome this incompatibility within a compact zero-gap MEA, a specialized interfacial component known as the buffer layer is employed [74].

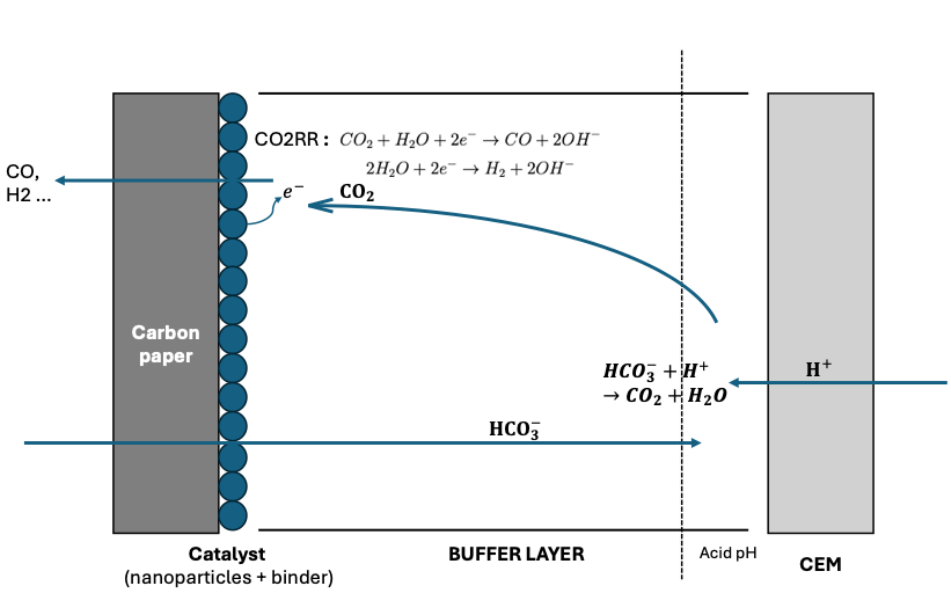

Figure 2.17: Schematic of the reaction within the buffer layer: bicarbonate ions are transported through the GDL and, upon contact with the membrane, under acidic conditions, CO_2 is released. It then flows towards the catalyst for CO_2RR.

The buffer layer is a porous, electrochemically inactive material placed between the CEM and the GDE [75]. Its function is to separate the membrane and the catalyst creating a gradient of pH where the accumulation of protons at the CEM generates a local acid condition. These conditions are fundamental for CO_2 gas regeneration (equation 2.8). Once the gas regenerated it diffuses toward the catalyst-coated GDE where the local pH becomes increasingly alkaline due to the accumulation of hydroxide ions (OH^-), a byproduct of the CO_2RR and HER (equations 2.9 - 2.10). CO_2RR is promoted in alkaline conditions, controlling the local pH controls the selectivity of CO or H_2 produced [76].

$$CO_2 + H_2O + 2e^- \rightarrow CO + 2OH^- \tag{2.9}$$

$$2H_2O + 2e^- \rightarrow H_2 + 2OH^- \tag{2.10}$$

This localized pH gradient, acidic at the membrane interface and basic at the catalyst surface, is the core functional principle of the buffer layer, enabling both CO_2 regeneration and electrochemical conversion within micrometer-scale proximity. With the production of sufficient hydroxide ions, increasing the pH, the exiting solution can capture new CO_2 for another

cycle.
An effective buffer layer must meet several design criteria: controlled porosity and permeability enabling capillary flow of bicarbonate and regenerated gas; the structure must sustain steep gradients of pH in a thin region; mechanical and chemical stability and minimal mass transport resistance to limit gas bubble accumulation.

Chapter 3

Experimental Procedures

In this chapter are discussed the primary experimental procedures and instruments that have been used in this thesis. It is divided in two sections: the first to evaluate the performance and activity of the electrolyzer in IIT laboratory, and second on materials characterization and fabrication used in the electrolyzer from PoliTO and IIT.

3.1 Bicarbonate electrolyzer assembly

This section provides a detailed overview of the bicarbonate electrolyzer components and its preparation. The electrolyzer is used for all electrochemical and chemical tests to evaluate the electrode's performance and the behavior of the bicarbonate solution under various conditions.

3.1.1 Flow plates and cell setup

The MEA is enclosed within two metallic flow plates that disperse the electrolyte evenly on the work surface and close the electric circuit. The flow plates used are from Dioxide Materials™ (Figure 3.1) composed of a stainless Steel cathode and a Titanium anode.

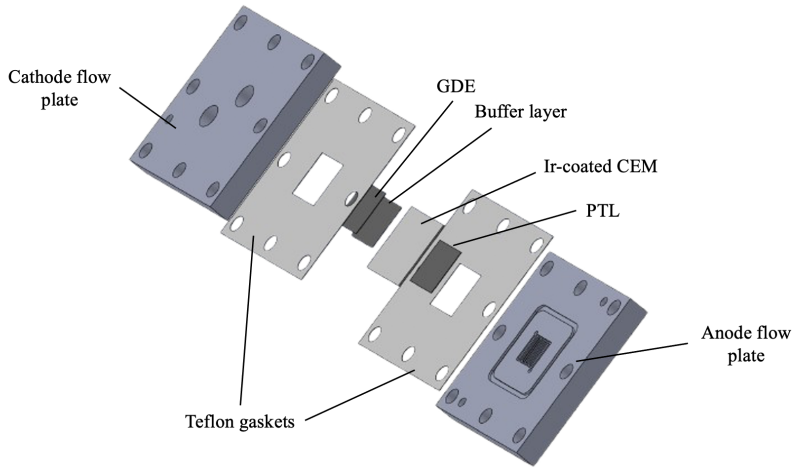

Figure 3.1: Exploded view of SolidWorks 3D model of the bicarbonate electrolyzer cell (Dioxide Materials™)

The cell is sealed with Teflon gaskets, which are non-electrochemically active material used to keep the MEA elements in place. To counter possible performance losses the flow plates are designed with serpentine flow field (Figure 3.2). This shape allows for the fluid to be homogeneously dispersed on the 5cm^2 work surface of the GDE without accumulating fluids.

Figure 3.2: Image of the serpentine flow field of a 5cm^2 electrolyzer (Dioxide Materials™)

3.1.2 Electrolyzer preparation

The MEA is composed of a CEM, a cathode and anode GDE. The CEM is made out of Nafion™ N117 (Sigma-Aldrich) coated by Ir on the anodic side. It is interposed between the cathode buffer layer (cellulose MCE MF-Millipore™ Merck) and the Platinized Titanium felt (PTL) as anode. The cathode GDE is placed in contact the buffer layer. The CEM is protonated for 15 minutes in 0.5 M H_2SO_4 (99.999%, Sigma-Aldrich) at 70°C before being tested. In acidic conditions at high temperature protons are transported inside the CEM initializing the proton transfer before inserting it in the electrolyzer. Once the CEM is protonated it is washed with distilled water and then inserted in the MEA.
Once the MEA is assembled it is placed inside the flow plates and are bolted together. Four bolts and o-rings are placed inside the holes at the corner of the plates and are tightened with a 4 N.m torque in two steps.

3.2 Electrochemical testing and measurements

This section discusses the instruments used for electrochemical tests of the bicarbonate electrolyzer. The instruments used provide information on the electrolyzer performance but also create specific conditions for the electrolyzer to be tested.

3.2.1 Generic test bench setup

The electrochemical testing is conducted on a generic test bench (Figure 3.3) composed of a peristaltic pump (Ismatec MCP) flowing the 3M $KHCO_3$ (99.5%, Sigma-Aldrich) catholyte water solution and 0.05M of H_2SO_4 (99.999%, Sigma-Aldrich) anolyte water solution at 40 $mL \cdot cm^{-1}$ into each compartment.
A potentiostat (BioLogic HCP) or a Source Measurement Unit (SMU) (Keithley 2635A) (Figure 3.4a. and b.) provide the cell with constant current and read the generated potential difference. Gases are supplied from cylinders and regulated by mass flow controllers (EL-Flow

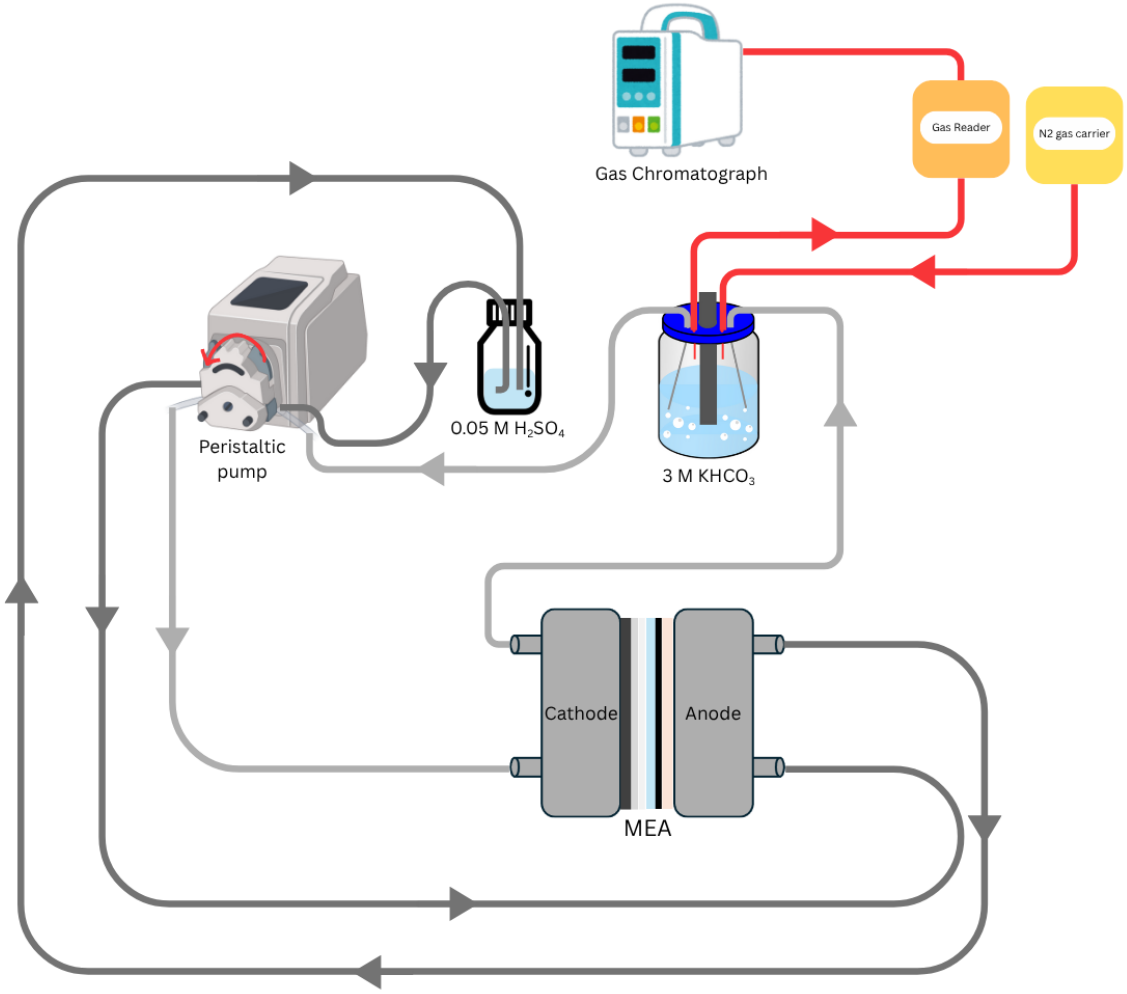

Figure 3.3: Schematic of the electrochemical test bench. Red lines indicate gas flow from the cell, light grey lines show catholyte flow, and dark grey lines show anolyte flow (both liquids).

Select, Bronkhorst) (Figure 3.4c.) , which control the flow rate (50 mL min^{-1} of N_2 gas). The gas-phase outlet flow rate from the reactor is monitored using a mass flow meter (EL-Flow Select, Bronkhorst), while the gaseous electrolysis products are analyzed online by a micro gas chromatograph (MicroGC, Fusion, INFICON) (Figure 3.4d.) positioned directly at the outlet of the mass flow meter. The MicroGC is equipped with two separate channels, featuring a 10 m Rt-Molsieve 5A column and an 8 m Rt-Q-Bond column, each ending with a micro thermal conductivity detector (micro-TCD).

(a) BioLogic HCP potentiostat

(b) Source Measurement Unit (SMU) (Keithley 2635A)

(c) EL-Flow Select, Bronkhorst mass flow controller

(d) MicroGC, Fusion, INFICON

Figure 3.4: Main electrochemical equipment used in the test bench: (a) BioLogic HCP potentiostat, (b) Keithley 2635A source measurement unit (SMU), (c) EL-Flow Select mass flow controller, and (d) MicroGC Fusion gas chromatograph.

3.2.2 Chronopotentiometry Measurements

Chronopotentiometry is an electrochemical technique in which a constant current is applied between two electrodes while the potential of one electrode is monitored over time compared to a reference electrode. In a two-electrode configuration, the counter electrode also serves as the reference electrode. This method is performed using a *potentiostat*, which applies the current and records the potential, sending the data to a computer for storage and analysis.
By analyzing potential changes in response to applied current, valuable information is obtained about the electrochemical properties of the materials under study. Furthermore, by adjusting the applied current and monitoring potential changes, the performance and long-term durability of electrode materials can be assessed.

3.2.3 Electrochemical Impedance Spectroscopy

Electrochemical Impedance Spectroscopy (EIS) is an electrochemical non-destructive characterization technique commonly used to investigate electrical properties of electrode-electrolyte interface. EIS is based on a perturbation of an electrochemical system in equilibrium, in this study the equilibrium between the electrode and the electrolyte solution. The perturbation consists of a sinusoidal alternating current, while the corresponding sinusoidal voltage response of the system is measured. From the relationship between input signal and the system's response, an impedance is defined. The results are represented with Nyquist plots, which separate the real and imaginary part of the impedance.

The characterization is conducted in laboratory applying and alternate current of 2 mA on an electrode surface of 0.2 cm^2 (10 mA cm^{-2}) variating the oscillation from 10 kHz to 10 mHz using a BioLogic potentiostat, which also recorded the response. The experimental procedure

includes an electrical contact with the electrode via copper tape. A layer of Teflon tape covers both the electrode and the copper connection leaving only the 0.2 cm^2 (equivalent to 10 mA cm^{-2}) electrode active area exposed to the electrolyte. A three-electrode setup was employed: the working electrode under study, a reference electrode (Ag wire in an AgCl casing), and a platinum counter electrode to close the circuit. The beaker cell was filled with a 3 M $KHCO_3$ solution. To keep the solution saturated, simulating the working condition of a bicarbonate electrolyzer, CO_2 is bubbled at 20 mL min^{-1} in the solution (Figure 3.5) [77].

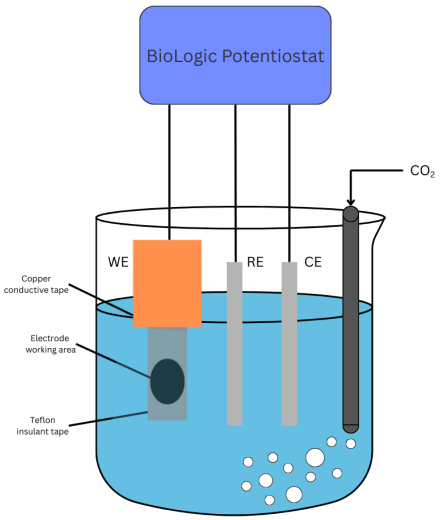

Figure 3.5: Schematic of EIS setup. CO_2 gas is bubbled during the measurement and a BioLogic Potentiostat varies the alternate current. WE: Working Electrode, RE: Reference Electrode and CE: Counter Electrode.

3.2.4 pH Monitoring of Catholyte Solution

During electrochemical testing, the pH of the bicarbonate solution changes: at low pH CO_2 is released, which then undergoes CO_2RR, increasing the solution pH generating OH^-. This evolution is monitored by placing a pH electrode in the catholyte container. The bicarbonate solution is pumped into the cell, reacts, and then flows back into the container for measurement. The pH meter measures the potential difference between two electrodes in a solution.A Vernier pH electrode was used. Inside the pH electrode is a selective glass bulb for hydrogen ion concentration. When immersed, ions exchange with the bulb, generating an electrochemical potential detected by an electronic amplifier. This potential difference is converted into pH units using the Nernst equation [78].

3.3 Electrode manufacturing and characterization

This section focuses on the manufacturing and preparation of the electrode and on the physical and chemical characterization of the material. To improve fluid management, catalysts are made out of porous material like carbon paper which is composed by carbon fibers intertwined and compacted for more structural resistance. The catalyst used is in nanopowder form, the deposition implies dispersing the nanopowders and applying it to the substrate.

3.3.1 Catalyst dispersion

For a homogeneous deposition of the catalyst on the porous substrate, the nanopowders need to be well dispersed in an organic solvent and/or acqueous solution (ink). A calculated amount of catalyst ($\sim$mg) is mixed with the according solvent ($\sim$mL) and a polymeric binder ($\sim \mu L$). For monometallic nanopowders such as Ag nanoparticles the solvent used is IPA (IsoPropylAlcohol), while for Single Atom Catalyst the solvent used is methanol. The polymeric binders (Sustainion, Nafion, PiperION) are available in 5wt% ethanol solution. Once prepared, the ink is sonicated in an ultrasonic bath for 30 minutes to ensure proper dispersion. When ready it is dispersed on the substrate using spray coating.

3.3.2 Catalyst Deposition via Spray Coating

The spraycoating instrument (Nadatech Innovation ™) is composed of a sealed ventilated chamber with inside a heated plate where the substrate is placed. Above the plate is the spray nozzle that moves on the 2D plane of the heated plate and a syringe containing the ink that controls the flow of ink in the nozzle. Spray coating is initiated via computer control. The nozzle moves to its starting position, and ink is fed from the syringe into the nozzle, where compressed air creates a fine spray. The nozzle has an ultrasound emitter ensuring the dispersion of nanoparticles inside. It moves above the plate following a programmed pattern defined for a specific deposition. For more accuracy a silicone mask is applied in the region of interest. The solvent (IPA) evaporates in contact with the heated substrate (80°C) leaving on the porous substrate the nanoparticles and the binder polymer (Figure 3.6).

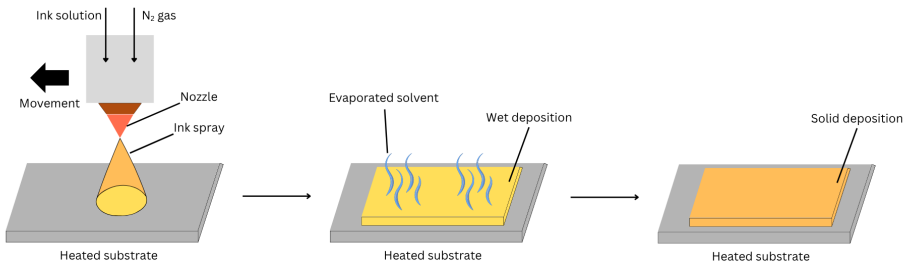

Figure 3.6: Schematic of the spray-coating process. The nozzle sprays catalyst ink using N_2 gas or air onto a heated substrate. Heat evaporates the solvent from the wet film, leaving a solid layer of dispersed catalyst particles.

The mass loading was quantified by weighing the carbon paper before and after deposition, and dividing the mass difference by the substrate area. This procedure being repeated for every deposition technique.

3.3.3 Thin Film Deposition via Sputtering

Silver electrodes for the bicarbonate electrolyzer were prepared using DC magnetron sputtering (Quorum Technologies Ltd., Lewes, UK, Q150T), a physical vapor deposition (PVD) technique that enables uniform and adherent thin film coatings under vacuum conditions. Commercial carbon papers (Freudenberg H23), each with a geometric area of 5 cm^2, were used as GDL substrates. A high-purity silver target (99.999%, Nanovision, Brugherio, Italy) in disk form

served as the sputtering source. The deposition current was maintained at 50 mA for a total of 300 seconds reaching 0.3 mg cm^{-2} silver mass loadings.

3.4 Electrode Morphological and Chemical Characterization

To further investigate the mechanisms and properties of catalysts in a bicarbonate electrolyzer, numerous characterization techniques have been used. These techniques can be divided in morphological analysis where surface information is obtained and chemical analysis to control composition of catalysts.

3.4.1 Field Emission Scanning Electron Microscopy

Field Emission Scanning Electron Microscopy (FESEM) is a highly suitable technique for morphological characterization of conductive materials. It is a non-destructive material characterization based on Scanning Electron Microscopy (SEM). From the interaction of a focused electron beam with the surface of a sample placed in a high-vacuum chamber, SEM provides structural and compositional information of the sample.
FESEM uses the same principle of electron interaction but with a different electron source. Traditional SEM instruments typically employ thermionic electron guns, FESEM employs a field emission gun (FEG), where electrons are extracted via quantum tunneling under a strong electric field. The electron beam produced is much narrower reducing the energy spread and increasing the brightness. With this technique imaging reaches resolutions up to 1 nm.
Depending on the detector used, electron microscopy can yield different types of information. Secondary electrons, generated near the sample surface, provide topographic images, while backscattered electrons, originating from deeper interactions, produce contrast related to the atomic number. In Figure 3.7 are schematized the general components of a electron microscope.

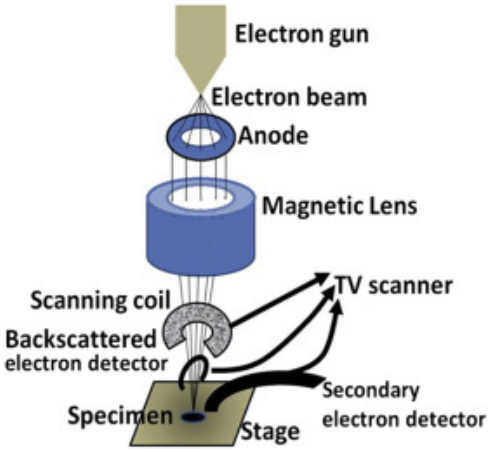

Figure 3.7: Schematic of an electron microscope. In a SEM the electron source is a heated Tungsten (W) or Lanthanum Hexaboride (LaB_6) filament. In a FESEM the electron source is a FEG composed of a W filament under strong electric field. [79]

3.4.2 X-ray Photoelectron Spectroscopy

X-ray Photoelectron Spectroscopy (XPS) is widely used for chemical surface analysis. The sample is irradiated with specific X-ray wavelengths emitting photoelectrons, internal core electrons ejected by X-ray photons. Detecting the photoelectrons kinetic energy, the electron binding energy is calculated from the incident X-ray wavelength. A plot of intensity of photoelectrons vs. binding energy identifies spectral peaks that are associated to elemental composition. Each peak is associated to a specific element and its oxidation state through XPS databases. The depth of analysis is 2-10 nm due to the reduced mean free path of photoelectrons [80]. Two types of spectra are typically acquired in XPS: a survey spectrum and high-resolution (HR) spectra. The survey spectrum, recorded over a broad energy range, providing an overview of the elemental composition of the sample by identifying the principal peaks corresponding to specific elements. Following this initial survey, HR spectra are acquired for selected peaks of interest. The key distinction lies in the energy resolution: HR spectra are recorded over narrower energy intervals with a greater number of data points, allowing for more precise separation of photoelectron signals. This increased resolution enables detailed analysis of chemical states, oxidation states, and subtle peak shifts that cannot be resolved in the broader survey spectrum. Consequently, HR spectra are essential for elucidating fine chemical information once the elemental composition has been established through the survey measurement. A schematic of an XPS instrument is depicted in Figure 3.8.

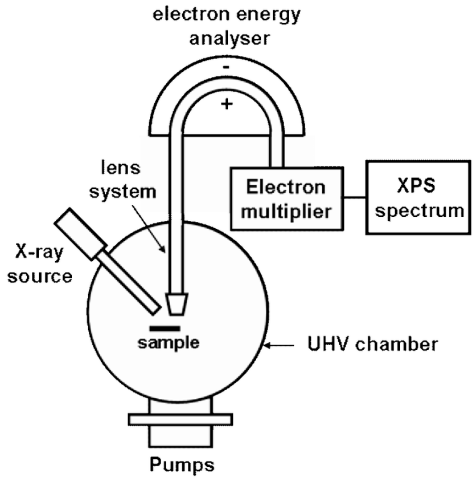

Figure 3.8: Schematic of an XPS instrument. The X-ray radiation interacts with the sample and emitted photoelectrons are focused onto the analyser which measures their kinetic energies and indirectly their binding energies.

Where the sample is placed in a ultra-high vacuum chamber exposed to X-rays. The emitted photoelectrons are separated by an electron energy analyzer and then counted for each specific binding energy obtaining the resulting spectrum.

3.4.3 X-ray Diffraction

X-ray Diffraction (XRD) is a non-destructive analytical technique widely used to obtain detailed information on the crystallographic structure and physical properties of a material. These structural properties are obtained from the diffraction image of monochromatic X-ray by the lattice and atomic planes of the sample. X-rays originated from high-energy charged particles that are decelerated, creating short-wavelength electromagnetic radiation.

In XRD analysis, the generated X-rays are collimated toward the sample. The interaction with the lattice diffracts the rays according to Bragg's law. From the analysis of the diffracted beams, the diffraction angle is measured defining the intensity of diffracted X-rays. The diffraction pattern is characteristic of the material, depending on the crystalline phase characterized by specific atomic arrangement and chemical composition. For multi-phase materials, a superposition of the individual phase patterns is observed. What characterizes the material are also the imperfections inside of the lattice. Factors such as compositional heterogeneity, crystal defects, microstrain, and crystallite size contribute to deviations from ideal diffraction behavior. This deviation is observed in the diffraction pattern affecting peak shapes, widths, and intensities. XRD data gives information not only about intrinsic crystallographic features but also extrinsic sample imperfections [81].
Beyond qualitative phase identification, XRD can also provide quantitative information about crystallite size and lattice strain. Analyzing the broadening of diffraction peaks with the Scherrer equation relates the peak width at half maximum to the average crystallite size d (equation 3.1). Peak shifts and asymmetry are indactors of microstrain or lattice distortions within the material.

$$d = \frac{K\lambda}{\beta cos\theta} \tag{3.1}$$

where λ is the X-ray wavelength, β is the corrected Full width at half maximum (FWHM) in radian, θ is the Bragg angle (degree) and K is the Scherrer constant.

3.4.4 Static Contact Angle measurements

Static Contact angle measurement is a direct technique to evaluate the hydrophilicity (wettability by water) of a surface [82]. A Biolin™ Theta Flex instrument is used dropping a single drop of water on the test surface and evaluating the contact angle via digital imagery. The higher is the contact angle the more hydrophobic is the surface. In the case of electrodes for a bicarbonate electrolyzer, hydrophobic electrodes limit the adsorption of water molecules reducing the HER. On the other hand, extremely hydrophobic electrodes block the bicarbonate solution flow, for those reasons the electrode needs to be hydrophobic within a certain range.

3.4.5 UV-visible spectroscopy

UV-visisible spectroscopy (UV-vis) is a non destructive technique widely employed to detect the formation of complex organic and inorganic molecules. Specific groups or chemical bonds absorb a specific wavelength with a specific energy equal to its absorption energy. Monitoring the absorption of wavelengths from UV to visible light (200 - 800 nm) of the sample, specific chemical groups are identified through databases [83]. Using specific absorption patterns of chemical groups and relative intensities, the molecules present in the sample are identified.

Chapter 4

Energy efficient reactive carbon capture

This chapter will discuss the experimental methods and results for an energy efficient Reactive Carbon Capture. The purpose of these experiments is to indentify optimal working conditions of the bicarbonate electrolyzer, where CO production selectivity is maximized while energy consumption remains low. From literature, the most used catalyst for CO_2-to-CO conversion is monometallic silver (Ag) nanoparticles [84]. Employing monometallic Ag catalyst, a series of energetic optimizations have been conducted to understand its behaviour in a Reactive Carbon Capture with a bicarbonate electrolyzer. The optimizations are focused on the composition of the spray-coated ink, including the polymeric binder, the silver mass loading and the implementation of a sputtered layer on the carbon paper. With future scale-up in mind, the influence of operating temperature and pressure on the electrolyzer's performances are also investigated.
For all electrochemical measurements, due to GC limitations, FE values are approximated with limited amount of error.

4.1 Influence of the binder on the bicarbonate electrolyzer performance

This section investigates the influence of polymeric binders in a bicarbonate electrolyzer's performances. The polymer binder present in the ink is crucial for dispersion of nanoparticles and for binding them once spraycoated. Depending on its chemical nature, the ionomer in the binder can transport either positive or negative electric charges while repelling the opposite. The binders selected are commercially available under the names Nafion, Sustainion and PiperION. They represent two classes of binders, Nafion is cation-conducting ionomer, whereas Sustainion and PiperION are anion-conducting ionomers.

4.1.1 Materials and methods

To compare the binders influence on the electrolyzers performances, similar GDEs are prepared and characterized.

Electrode preparation

Three elecrodes with different binders are prepared to be compared using Nafion, Sustainion and PiperION for each one. The electrode is a porous Freudenberg H23 carbon paper cut into 5cm^2 squares with spraycoating of Ag nanoparticle ink. H23 carbon paper shows hydrophilicity allowing the water-bicarbonate solution to flow easily inside the GDE. The ink is prepared by

mixing 15 mg of Ag nanoparticles (< 150 nm Sigma Aldereich 99%), 38.9μL of binder 5 wt% solution, and 4 mL of isopropanol (IPA, 99.5% Sigma Aldrich). After sonication, the catalyst ink is spray coated on the carbon paper till a mass loading of 1.5 mg cm^{-2} is achieved. The resulting mass of binder accounts for 10% of the total mass deposited on the GDE.

Characterization

The obtained electrodes are characterized through FESEM and contact angle measurements. Each electrode is tested using the generic electrochemical bench setup (section 3.2.1). To guarantee consistent and reliable data, a new electrode, buffer layer and electrolyte solution were used for each test. An EIS analysis (section 3.2.3) is conducted on all samples for better understanding of the dynamics at the interface between catalyst and electrolyte.

4.1.2 Results and Discussion

Electrochemical tests and product analyses

As described in section 3.2.1, the bicarbonate catholyte and the acid anolyte are prepared, and the electrolyzer is assembled with the GDE inside. The cell is connected to a potentiostat applying a 1 A (200 mA cm^{-2}) constant current to cell and measuring the resulting tension. The gasses are measured and analysed by a FlowMeter and a Gas Chromatograph (GC). The calculated FE of CO production through CO_2RR (FE$_{CO}$) and measured cell voltage are plotted for each GDE with a different binder in Figure 4.1.

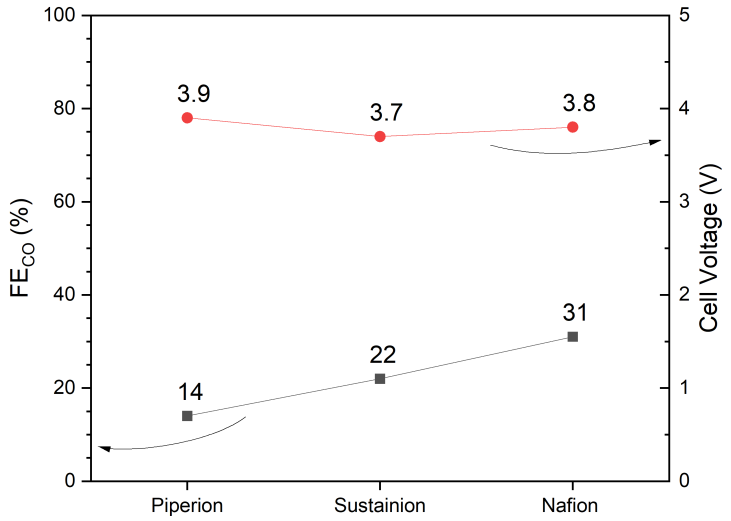

Figure 4.1: Cell voltage (red) and calculated FE for CO (black) for GDEs with different binders at 200 mA.cm^{-2}.

The cell voltage is not significantly affected by the binder, remaining around 3.9 V and 3.7 V, while the FE of CO changes drastically. The Nafion-based GDE exhibits a FE$_{CO}$ of 31%, more than double of the PiperION-based GDE. Sustainion-based GDE shows also reduced FE$_{CO}$ compared to the Nafion-based GDE. This difference can be attributed to the chemical structure of the polymeric binder, having that Nafion is cation-conducting while Sustainion and PiperION

are anion-conducting. When the Ag nanoparticles are deposited on the carbon paper, they are bound by the binder. With the binder dispersed on the surface, it can be assumed that the charges of the ionomer are also dispersed.
Given its cation-conductive nature, the GDE containing Nafion will have negative charges on its surface. While Sustainion and PiperION-based GDE's surface will have positive charges. This difference in surface charge leads to different interaction between the ions present in the bulk solution and the catalyst surface:

- Negative superficial charges will repel OH^- ions, allowing more CO_2 to be adsorbed on the catalyst.
- Positive superficial charges will accumulate OH^- ions near the surface, creating a CO_2-consuming layer limiting CO_2 adsorption.

The interaction of ions and molecules of the bulk solution with differently charged surfaces is schematized in Figure 4.2.

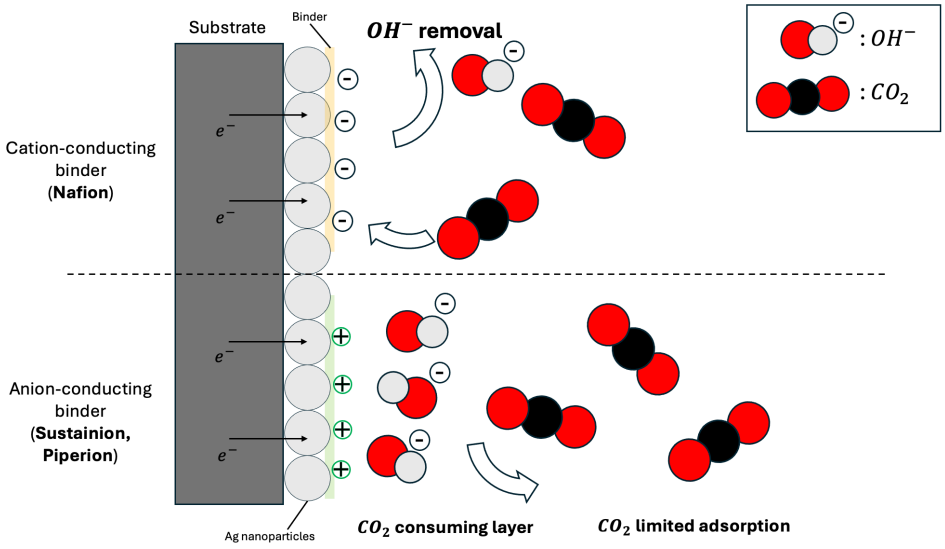

Figure 4.2: Schematic representation of bulk ions and molecules interacting with charged catalyst surface. Nafion allows for better circulation of OH^- ions limiting their accumulation.

Nafion-based GDE's high FE_{CO} can be attributed to its superficial chemical charge and resulting superficial interactions. More GDE characterizations are conducted to understand more specifically Nafion's high results. FESEM morphological images are taken to observe the distribution and binding of the nanoparticles. Additionally, Nafion's high FE_{CO} can also be described by its hydrophobicity: the more hydrophobic is a GDE's surface less water goes in contact, limiting the HER and thus the production of H_2. To evaluate this hypothesis, the various GDEs contact angles are compared. Finally, an EIS analysis is made all GDEs to describe exactly the surface interaction with the bulk and validate the charge repulsion supposition.

FESEM

A high precision image of the spraycoated surface is obtained using FESEM analysis to evaluate the nanoparticles distribution. FESEM images in secondary electrons of the cross section of the GDE prepared with Nafion binder are shown in Figure 4.3. The tubular like structure are the carbon fibers of the H23 carbon paper.

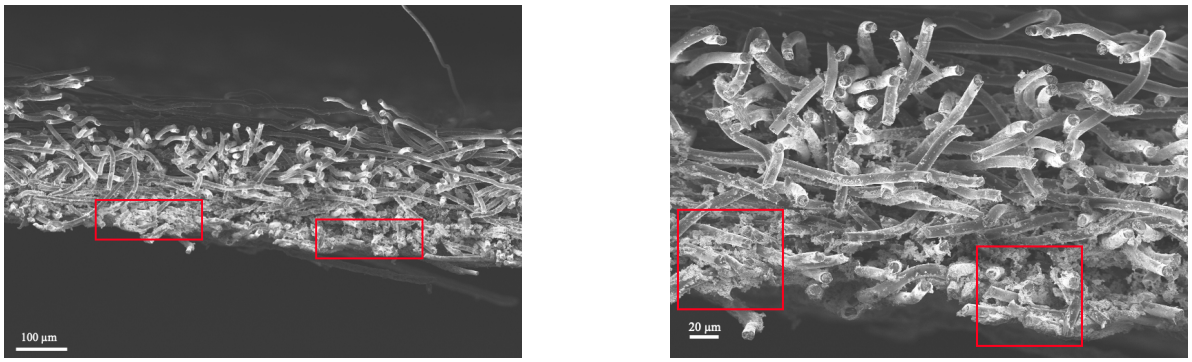

(a) 100X (b) 250X

Figure 4.3: FESEM cross-sectional images (secondary electron mode, 5 kV) of Ag nanoparticles dispersed in IPA and Nafion, spray-coated onto H23 carbon paper. The porous structure ensures good catalyst distribution and penetration into the carbon fiber network, enhancing active surface area.

In the red squares of Figure 4.3a. it is evident that only the superficial part of the cross-section presents nanoparticles, while Figure 4.3b. shows that the binder creates agglomerates of nanoparticles in very localized regions on the carbon fibers. The presence of agglomeration is a good sign because the binder is effective and the agglomerate is distributed on all the carbon paper. Sustainion and PiperION based inks showed similar distributions of nanoparticles on the spraycoated surface.
While the formation of catalyst aggregates is observed; a significant fraction of the carbon substrate remains directly exposed to the catholyte. Unlike Ag, carbon does not possess intrinsic catalytic activity for the targeted reaction and instead facilitates the HER. A better superficial covering needs to implemented to address this limitation of the electrode.

Static contact angle measurements

To investigate the influence of different binders on the electrode's behavior, contact angle measurements were performed to assess the hydrophobicity of the electrode's surface. A higher degree of hydrophobicity corresponds to an increased tendency of the surface to repel water. Since a CO_2RR-selective surface is desired, one strategy to suppress the competing HER is to minimize the extent of water interaction with the substrate surface. Also hydrophobicity limits the presence of hydroxide ions formed during the CO_2RR by repelling water, ensuring a maximum adhesion of CO_2 to the surface.
The different results of contact angle measurements for each electrode compared to a blank H23 carbon paper support are reported in Figure 4.4.

For more precise results, three contact angle measurements are made on different locations of the electrode sample. In Figure 4.5 are plotted the resulted measurements with calculated standard deviation.

From these measurements, the Nafion-based electrode results the most hydrophobic. Sustainion exhibits a very similar contact angle to the blank H23 carbon paper, while PiperION has a lower contact angle than the blank. This indicates that chemical differences of the polymeric binder change the overall electrode behaviour. The calculated error show little variations in the blank measurements being an industrial product with strict manufacturing control. While the errors for the lab produced electrodes increase indicating variations of the electrode behaviour on its surface caused by imperfections on the deposition. The measured higher hydrophobicity

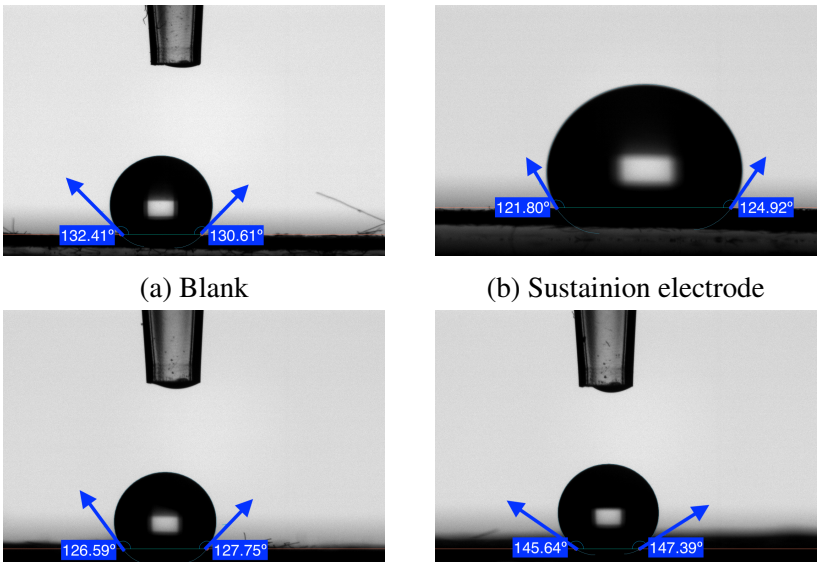

(a) Blank (b) Sustainion electrode

(c) Piperion electrode (d) Nafion electrode

Figure 4.4: Contact angle measurements image capture for all electrodes with different binders compared to a blank.

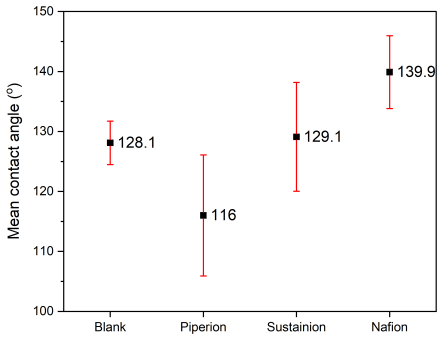

Figure 4.5: Measured static contact angles of electrodes with different binders compared to blank with errors.

can be linked to the increased electrolyzers performance. Considering the OH^--repelling surface of the Nafion-based GDE, limiting the contact with water limits also the HER. To have the certainty of this effect, additional EIS is performed on the electrodes.

EIS analysis

EIS analysis is made to verify the effectiveness of Nafion binder. The EIS is carried out as described in Section 3.2.3, and the results define a Nyquist plot from which different parameters can be obtained. The first is the **Charge Transfer Resistance** (R_{ct}) corresponding to the resistance to charge flow across the interface, directly related to the electrochemical reaction kinetics, obtained from the diameter of the semicircle. Then is the **Double Layer Capacitance** (C_{dl}) that defines the electrical double layer at the interface acting like a capacitor storing charge, it is directly related to the effective surface area of the electrode. The Nyquist plots obtained for the different binder electrodes are shown in Figure 4.6 and values resumed in Table

4.1.

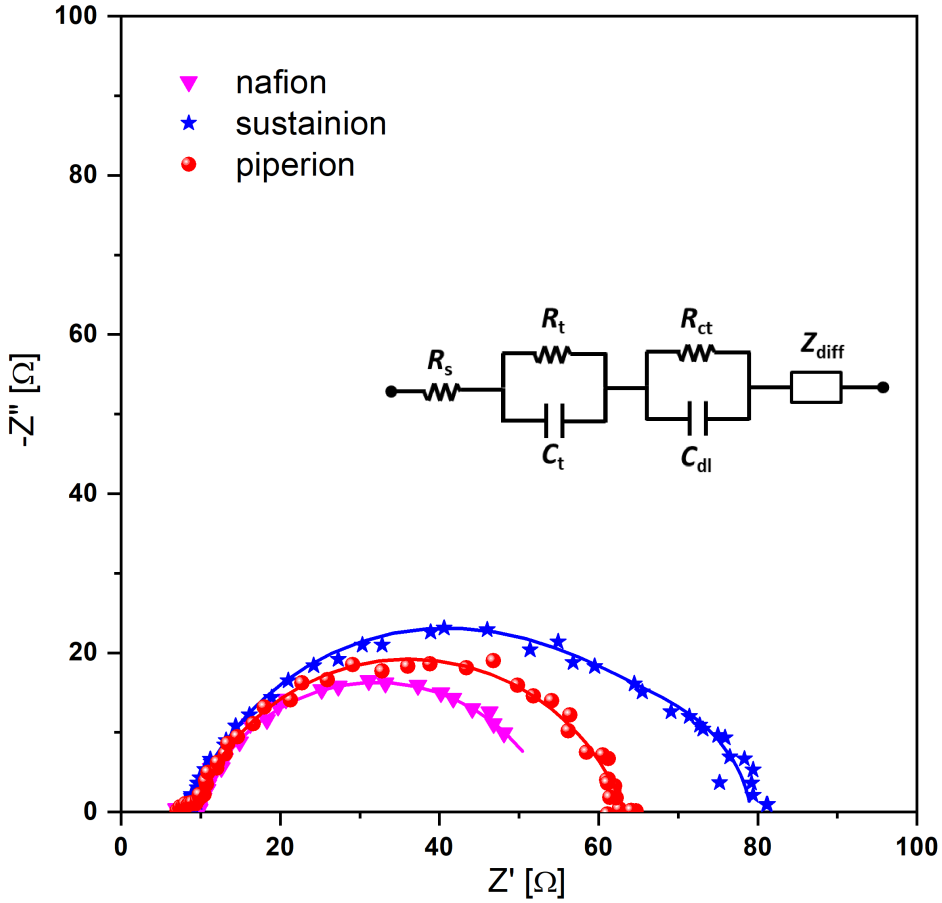

Figure 4.6: Nyquist plots of the measured EIS analysis with curve fittings to measure equivalent circuit parameters.

Table 4.1: Measured EIS parameters for different binder electrodes in the same working conditions.

Binder	R_{ct} (Ω)	C_{dl} (F)
Piperion	54.07	1.49E-5
Sustainion	58.33	7.21E-6
Nafion	45.39	1.23E-4

The most significant outcome is the difference in the orders of magnitude of C_{dl}. Nafion-based GDE exhibits a C_{dl} nearly ten times the value of PiperIONbased GDE and seventeen times the value of Sustainion-based GDE. Observing such high differences in C_{dl} values indicates substantial increase in the effective surface area of the electrode. Nafion-based GDE's greater active surface area can be a possible reason for its high performance. In addition to that observation, a drastic reduction in the R_{ct} is also noticeable with the Nafion-based GDE having almost 10 Ω difference with the PiperION-based GDE, and 13 Ω difference with the Sustainion-based GDE. Lowering R_{ct} indicates faster reaction rates, allowing for CO_2 to undergo CO_2RR

more quickly on the Nafion-based GDE respect to the other electrodes.
From these results and discussion, the hypothesis made in Figure 4.2 can be explained. The Nafion-based GDE has an higher active area from the OH^- repulsion by the surface and allows for reduced resistance in the charge transfer removing the ions. While the formation of the CO_2-consuming layer in Sustainion/PiperION-based GDEs can be observed with the reduced effective active surface area and the high charge transfer resistance.

Conclusion

The first optimization of the spray-coating ink is made on the polymeric binder due to its selective nature and effect on particle dispersion. Two different types of polymeric binders have been tested, cation-conducting and anion-conducting. From the electrochemical tests cation-conducting binders, such as Nafion, show increased conversion performances. These performances can be explained by the binders chemical nature: showing negative charges on its surface it repels OH^- ions allowing for more catalytic active surface and better charge transfer. These results have been highlighted by EIS analysis showing the highest active area and the lowest resistance to charge transfer. While anion-conducting binders show a CO_2-consuming layer that limits the adsorption of CO_2 on the catalyst surface and limits the charge transfer.
Contact angle measurements also highlight a strong hydrophobicity of the Nafion-based GDE. Controlling the hydrophobicity of the surface limits the contact between water and the electrode. In presence of an electric potential, water reacts by undergoing HER generating H_2 lowering the desired CO production. Combining hydrophobicity of the electrode and its electrochemical behaviour in a bicarbonate electrolyzer, the **Nafion**-based GDE results the most effective. Even though the electrochemical results are good, a reduced covering of the GDE can be observed using FESEM imagery. The limited FE_{CO} can be explained by the uneven covering of the GDE, where exposed carbon paper facilitates undesired HER. Future optimization must mitigate this uneven substrate covering to improve the electrolyzers performance.

4.2 Influence of the Ag loading on the bicarbonate electrolyzer performance

In this section is examinated the effect of increased Ag loading on the electrode surface properties and catalytic activity. According to Hussain N. et al. [85], augmenting the number of metallic sites directly enhances catalytic performance. Given the previously observed an uneven surface covering of the electrode, two stategies are evaluated: (1) increasing the nanoparticles loading and (2) employing silver sputtering to achieve a more homogeneous deposition.
The first alternative involves an increase in the concentration of nanoparticles dispersed on the surface. The second alternative introduced a different deposition technique: sputtering generates a uniform layer of atomic Ag on the substrate, ensuring a more complete and even surface coverage. To evaluate these hypothesises, the loading of Ag nanoparticles is doubled (3.0 mg cm^{-2}) and tripled (4.5 mg cm^{-2}) keeping Nafion as binder. A hybrid electrode is produced by sputtering silver on the substrate and spraycoating Ag nanoparticles over it, designed to isolate and evaluate the specific contribution of sputtering.

4.2.1 Materials and methods

Three electrodes are prepared from 5cm^2 square pieces of Freudenberg H23 carbon paper depositing Ag nanoparticles using spray-coating at different loadings. A fourth hybrid electrode was created by first sputtering silver onto the carbon paper's surface and then depositing a layer of silver nanoparticles via spray-coating over it.

Electrode preparation

Three GDEs are prepared by increasing the catalyst loading within the spraycoating ink. For each electrode, the binder concentration is maintained at 10wt.% relatove to the total deposited mass. Each ink is made from 4 mL of IPA in which are added the precise compositions shown in Table 4.2.

Table 4.2: Composition of inks used for electrode manufacturing at increasing catalyst loading

Ag NP loading	Quantity of Ag nanoparticles (mg)	Nafion dispersion volume (μL)
1.5 mg cm^{-2}	15	38.9
3.0 mg cm^{-2}	30	77.8
4.5 mg cm^{-2}	45	114.4

The obtained inks are sonicated and subsequently spraycoated onto the H23 carbon paper substrates until the desired catalyst loading is acheived. These electrodes, featuring only nanoparticles dispersion, are designated as **single layer electrodes**.

For the sputtering process, the H23 carbon paper substrate is placed in a Q150T ES sputtering machine. Sputtering is performed at 50 mA in $2{\cdot}10^{-4}$ mbar of pressure for 300 s. After the sputtering process, the resulted covered substate is spraycoated with the previously described ink, containing a 3.0 mg cm^{-2} Ag nanoparticle loading. The resulting electrode, with both a sputtered layer and a nanoparticle layer is referred as a **double layer electrode**.

Characterization

The obtained electrodes are characterized through FESEM and contact angle measurements. Each electrode is tested using the generic electrochemical bench setup (section 3.2.1). To guarantee consistent and reliable data, a new electrode, buffer layer and electrolyte solution were used for each test. An EIS analysis (section 3.2.3) is conducted on all samples for better understanding of the dynamics at the interface between catalyst and electrolyte.

4.2.2 Results and discussion

Single layer electrodes

To evaluate the effect of catalyst loading, the fabricated single layer electrodes are tested under identical experiment conditions using the generic bench setup. The calculated FE of CO production through CO_2RR (FE_{CO}) and measured cell voltage are plotted for each GDE with a different loading in Figure 4.7.

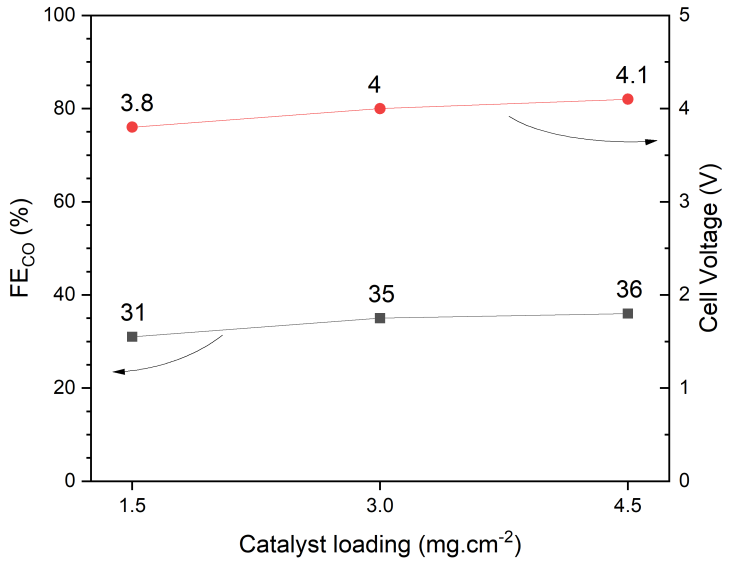

Figure 4.7: Cell voltage (red) and calculated FE of CO (black) for GDEs with varying Ag nanoparticle loadings at 200 mA.cm^{-2}. Higher loadings enhance selectivity of CO but also slightly increase cell voltage due to greater catalyst layer thickness.

The electrochemical measurements revealed an increase of cell voltage up to 4V, indicating that a higher nanoparticle loading introduce greater resistance to current flow within the cell. This suggests that depositing more material onto the electrode increases the ohmic resistance of the cell, thereby raising the overall potential. When the surface loading is doubled, it resulted in a 4 percentile points increase of the FE of CO. However, tripling the loading only yielded an additional 0.5 percentile increase. This trend suggests a non linear dependance of conversion efficiency and material loading. For the next part of the work, the 3.0 mg cm^{-2} Ag nanoparticle loaded GDE will be considered as the single layer electrode.

Double layer electrode

Electrochemical tests and product analyses

Identical tests following the same procedure as for the single layer electrode are conducted on the double layer electrode. The results of both electrodes are graphed in Figure 4.8.

The double layer electrode showed moderate selectivity improvement, with a 6 percentile points increase. The presence of sputtering shows a reduction of the cell voltage to 3.8 V lowering the power consumption of the cell. Even if the cell voltage decrease is minimal, it's particularly noteworthy given that the double-layer electrode's loading ($\sim$ 3.3 mg cm^{-2}) is higher than the single-layer's. Despite the increased mass, the cell voltage didn't rise like

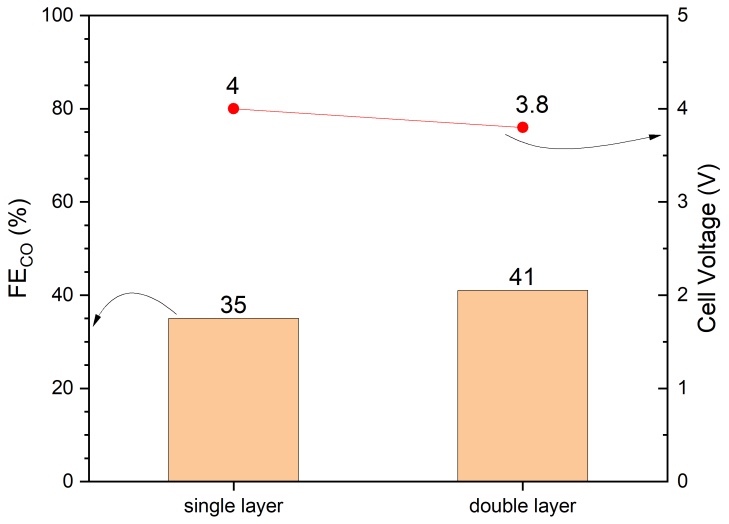

Figure 4.8: Cell voltage (red) and FE of CO (black) for single and double layer electrodes at 200 mA cm^{-2}. Sputtering improves CO selectivity and slightly lowers voltage, indicating enhanced mass transport and electronic contact.

described earlier. This result can suggest that the sputtering process may help reduce the ohmic resistance of the cell.

FESEM

To explain the electrochemical and GC results, the double layer electrode is analyzed using FESEM analysis. First, a H23 carbon paper with silver sputtering is observed through FESEM to evaluated the substrate covering, shown in Figure 4.9.

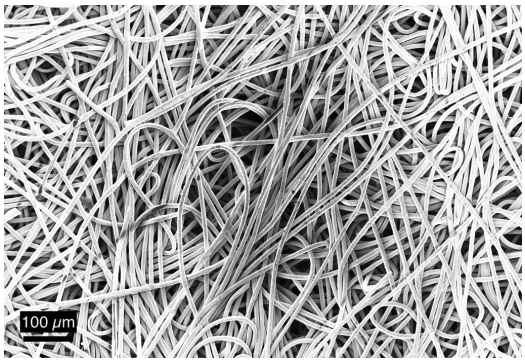

(a) 100X

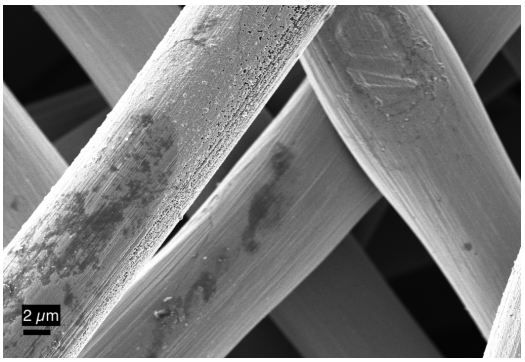

(b) 2500X

Figure 4.9: FESEM images (secondary electron mode, 5 kV) of Ag sputtered onto H23 carbon paper, showing uniform thin-film coverage on carbon fibers, which can improve catalyst adhesion and electrical conductivity.

The surface morphology of the electrode after sputtering shows a uniform and continuous coating. The composing fibers of the carbon paper are still distinguishable and evenly covered

with no observable defects. This even deposition confirms achieving optimal sputtering coverage conditions. Given this successful and uniform sputtering layer, it can be compared to the double layer electrode in Figure 4.10.

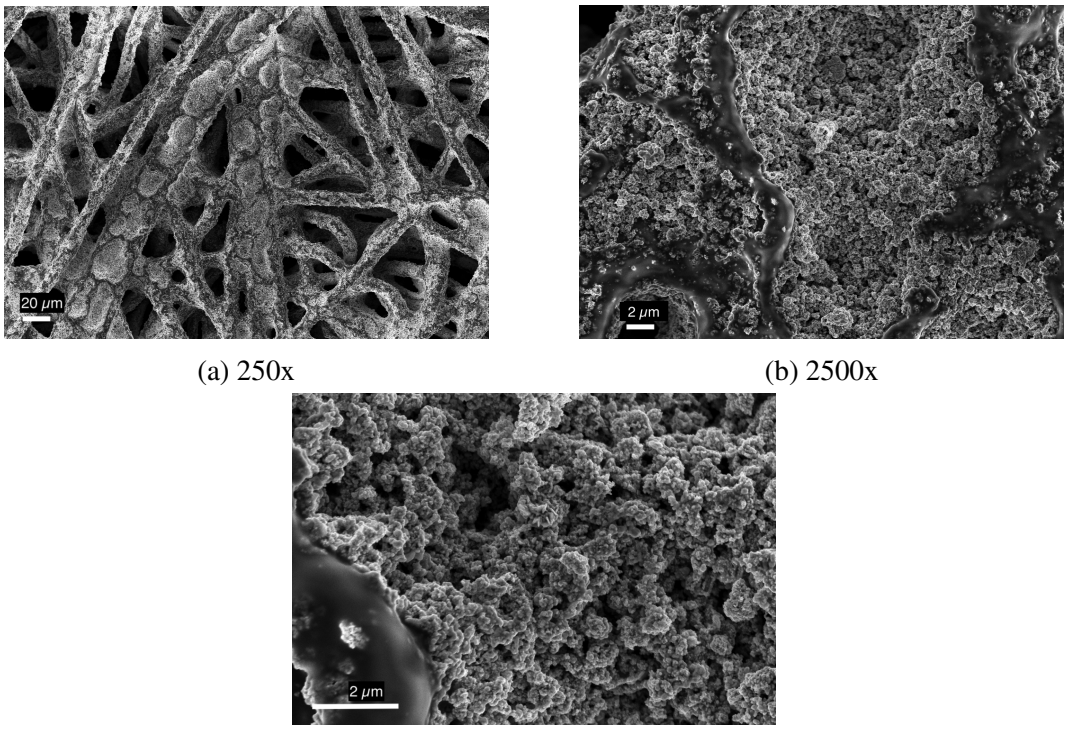

(a) 250x (b) 2500x

(c) 10 000x

Figure 4.10: FESEM images (secondary electron mode, 5 kV) of Ag spray-coated onto Ag-sputtered H23 carbon paper.

A significant modification in the electrode's surface is observed on the double layer electrode. At low magnification, the composing fibers of the carbon paper are discernible (Figure 4.10a.). However, as magnification increases, these fibers become less distinct. The resulting structure is complex, at high magnifications (Figure 4.10b.) rough agglomerates of nanoparticles are distinguishable over a smooth sputtering deposition. This layered structure maximizes interaction between the carbon paper and the catalyst with the sputtering layer supporting the nanoparticles aggregate. Increased interaction between catalyst and support suggests the increased conversion efficiency and reduced cell voltage in the electrochemical measurements.

Static contact angle measurements

The contact angle measurements investigate the influence of sputtering in the double layer electrode compared to the single layer electrode are shown in Figure 4.11.

For more precise results, three contact angle measurements are made on different locations of the electrode sample. The resulted measurements with the calculated standard deviation are plotted in Figure 4.12.

Both single and double layer show reduced hydrophobicity compared to low loading electrode. Despite having lower contact angles, the two modified electrodes exhibit superior electrochemical properties. While the measured contact angle remains high at over 130 °, indicating a hydrophobic surface, the new electrode designs prove effective even with this limited hydrophobicity. A lower contact angle implies less resistance to the flow of the water-based bicarbonate

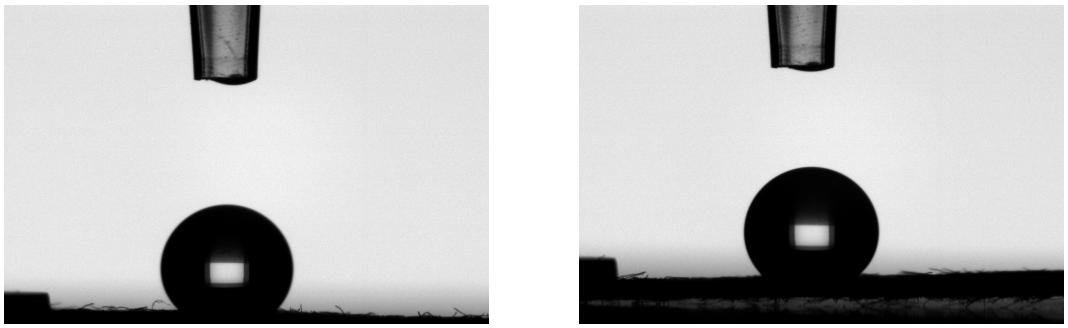

(a) single layer (b) double layer

Figure 4.11: Contact angle measurements image capture for single and double layer electrodes.

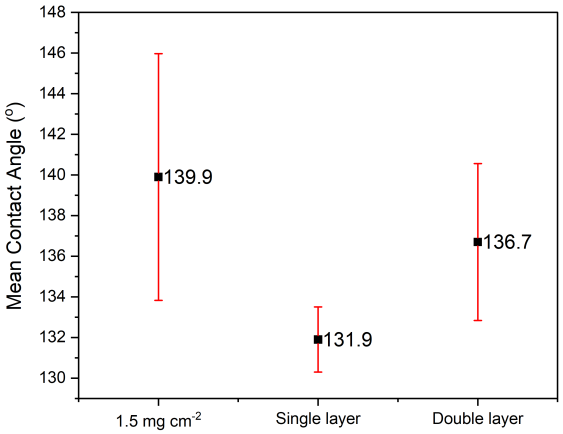

Figure 4.12: Measured static contact angles of single and double layer electrodes compared to Nafion binded 1.5 mg cm^{-2} loading of Ag nanoparticles electrode.

solution, which may explain the observed reduction in cell voltage within the cell. This suggests that the structural modifications not only modify the surface wetting properties, but are key to enhancing performance.

EIS analysis

An EIS analysis is performed on the single and double electrode compared to the low-loading electrode to evaluate and quantify the effective covering of sputtering. The procedure follows the methodology described in Section 3.2.3. The results produce a Nyquist plot, from which key electrochemical parameters are extracted. As described earlier, the parameters determined are R_{ct} and C_{dl}. They give us insight on the effective active area and reaction kinetics at the surface of the electrode. The corresponding Nyquist plot are shown Figure 4.13 and calculated parameters R_{ct} and C_{dl} are transcribed in Table 4.3

From the results it is clearly shown that C_{dl} value increases with loading and sputtering implementation. Specifically, the double layer electrode's C_{dl} is 2.7 times greater than the low-loading electrode's and 1.3 times greater than the single layer electrode's, consistent with an enlarged electrochemically active surface area.
The overall R_{ct} remains comparable with the three electrodes, with the single layer electrode

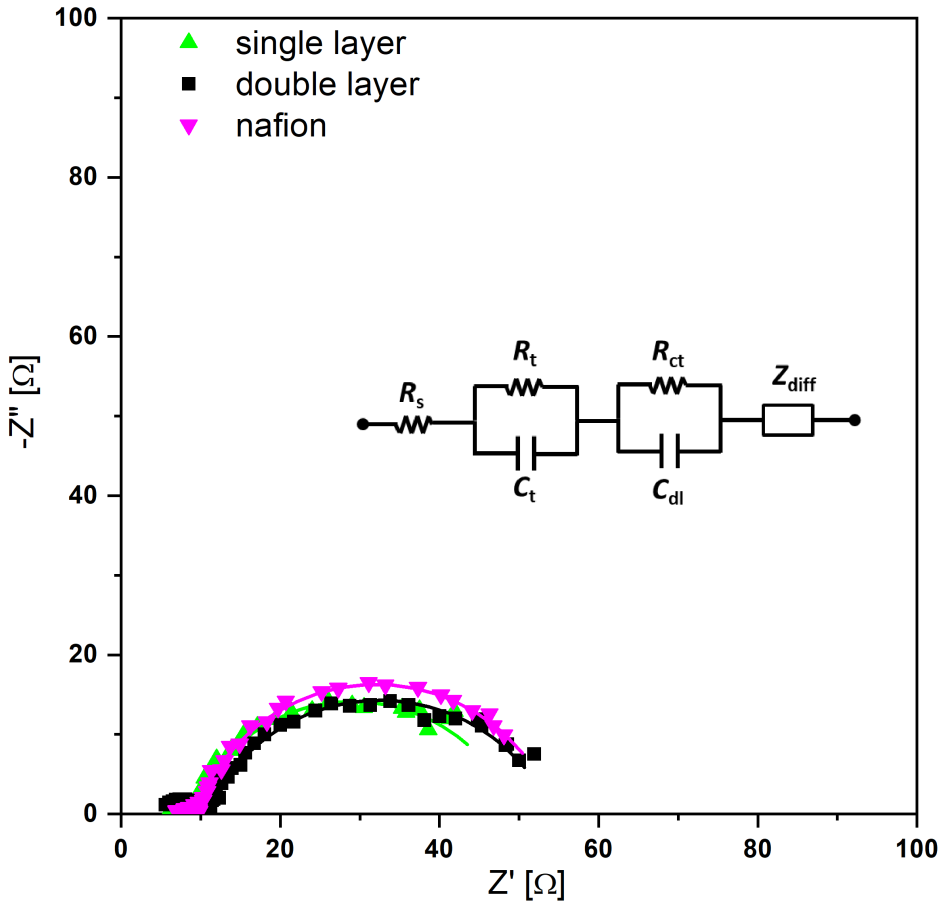

Figure 4.13: Nyquist plot of measures for different loading electrodes with curve fitting to calculate equivalent circuit parameters.

Table 4.3: Measured IES parameters for single and double layer electrode compared to the initial Nafion-binded electrode.

Electrode	R_{ct} (Ω)	C_{dl} (F)
1.5 mg cm^{-2}	45.39	1.23E-4
Single layer	40.82	2.53E-4
Double layer	43.57	3.31E-4

showing the lowest value (40.82 Ω). This suggests that the reaction kinetics are similar under the same working conditions.
The electrochemical results can be described with the EIS parameters. The double layer combines a larger effective area with favourable reaction kinetics, creating an optimal surface for catalytic activity.

Conclusions

To resume, the implementation of sputtering proves to be effective in enhancing the double layer electrode's performance. Under identical working conditions, the double layer electrode reaches FE_{CO} of 41% with a reduced 3.8 V cell voltage. FESEM images reveal a synergic

effect between the Ag nanoparticles and underlying sputtered layer, highlighting a maximum interaction between Ag catalyst and support. The uniform substrate coverage is also determined by the high electric double layer capacitance, indicative of a large number of active sites. Both single and double layer electrodes exhibit reduced contact angles relative to the low-loading electrode, which may influence the reduction in cell voltage.
By combining optimal covering, the correct catalyst loading and binder content to preserve catalytic activity, **the Ag based electrode is optimized**.

4.3 Role of pressure and temperature

This section will discuss the effect of external conditions on the bicarbonate electrolyzer. Gaining a precise understanding and control of these parameters at a laboratory scale is crucial for the successful future scale-up of this system. In larger-scale applications, the electrolyzer is subjected to several significant external factors. It will experience Joule heating due to the high electrical currents and will operate with increased electrolyte flow rates for extended periods of time, exceeding 100°C [86]. These conditions can significantly influence the overall performance of the system. Therefore, to ensure a consistent performance on the cathode side of the electrolyzer, two key parameters must be carefully managed: temperature control and pressure monitoring, which includes the use of back pressure modules.
To understand the effects of external parameters, we used the standard bicarbonate electrolyzer described earlier, equipped with the double-layer electrode from Section 4.2. Two key parameters are investigated: liquid pressure and temperature. The effect of liquid pressure is examined first. It is controlled by a back-pressure module, increasing the liquid pressure in the electrolyzers channels, affecting the residence time of both the solution and CO_2 within the system. This extended residency time of the reactants is expected to increase the reaction rates at the cathode. This could maximize the regeneration of iCO_2 and the conversion into CO. Next is explored the impact of temperature on the electrolyzers performance. Increasing the reaction temperature introduces more thermal energy into the system, allowing for faster reaction rates and increased agitation of the species involved.

4.3.1 Materials and methods

Electrode preparation

The employed double layer electrode is fabricated by first sputtering Ag on a Freudenberg H23 5cm^2 square piece carbon paper, then spray-coating it with 3.0 mg cm^{-2} Ag nanoparticles. The final electrodes exhibits an overall 3.3 mg cm^{-2} loading of Ag. To guarantee consistent and reliable data, a new electrode, buffer layer and electrolyte solution were used for each test.

Backpressure implementation

To evaluate the pressure effect on a laboratory scale, the generic bench setup is modified by adding a **backpressure** module. This device creates pressure within the fluid channels by restricting the outflow of the solution. It is inserted on the cathodic side of the electrolyzer as shown in Figure 4.14.

The backpressure module used is a Bronkhorst El-Press ™ model (Figure 4.15), a digital electronic pressure meter and controller. This device is ideal for backpressure applications because it can maintain a certain pressure within the tubing while reading the generated pressure.

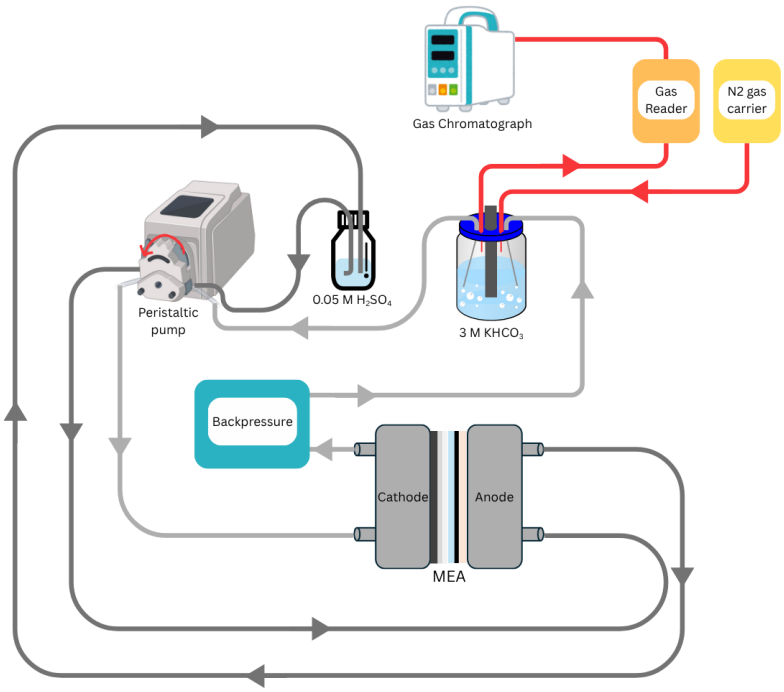

Figure 4.14: Schematic of the electrochemical bench setup with a backpressure module installed on the bicarbonate solution outlet, enabling evaluation of pressure effects on CO_2RR performance.

Its operation is based on a diaphragm that opens and closes in response to pressure values given by the operator and the real-time pressure readings by the controller.

Figure 4.15: Bronkhorst El-Press™ digital electronic pressure meter/controller used to regulate and monitor backpressure during bicarbonate electrolysis experiments.

The backpressure test uses the same catholyte and anolyte solutions as the generic bench setup. Electrochemical tests are conducted at three different current densities (100, 200, 300 mA cm^{-2}) and increasing back-pressure conditions: 0 bar (no backpressure), 0.6 bar and 1 bar. The pressure is monitored using the FlowDDE software and the resulting gasses analyzed by a micro-GC.

Temperature control

To control the temperature of both the catholyte and anolyte solution, their respective containers are placed in a temperature controlled bain-marie. The electrolyzer cell is heated at the desired temperature using two 50 W 110 V heaters (Dioxide Materials™), which are mounted on each

flow plate. The heaters are set to match the temperature as the bain-marie and regulated with an external control module. (Figure 4.16)

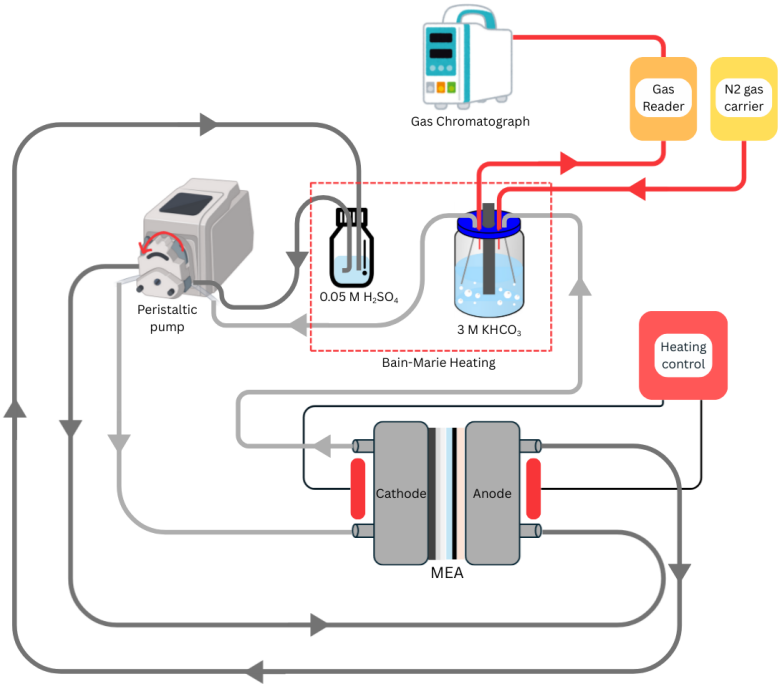

Figure 4.16: Schematic of the electrochemical bench setup with a temperature control module and a bain-marie for solutions.

The temperature test use the same catholyte and anolyte solutions as the generic bench setup. Electrochemical tests are run at constant current density of 200 mA cm^{-2} under two different temperature conditions: 40 °C and 60 °C. These two temperature condition are chosen being temperatures that industrial electrolyzers reach when working. The product gasses are analyzed with a micro-GC. The results from the tests are compared to the double layer test at ambient temperature (25 °C), as reported in section 4.2.2.

4.3.2 Results and Discussion

Influence of pressure

The backpressure module increases the residence time of the bicarbonate solution inside the electrolyzer. To observe the influence of pressure the tests have been conducted at increasing current densities and reported in Figure 4.17.

Increasing the current density the fraction of CO follows a decreasing trend. Under high current densities, a combination of intense electroosmotic water flow and cation migration from the anode leads to electrode flooding. This phenomenon impedes the transport of CO_2 by creating a thicker diffusion layer, thereby intensifying the mass transport limitation. The restricted supply of CO_2 then causes a shift in the reaction pathway, with the HER becoming the predominant process. [86]

When applying back-pressure, two conditions emerge: low back-pressure reduced the electrolyzers performance, while higher back-pressure improved it. At a back-pressure of 0.6 bar, a drastic decrease of performance is highlighted with the FE_{CO} dropping to 35% at 200 mA cm^{-2}. This decline suggests that under low CO_2 partial pressures, the high current rapidly consumes

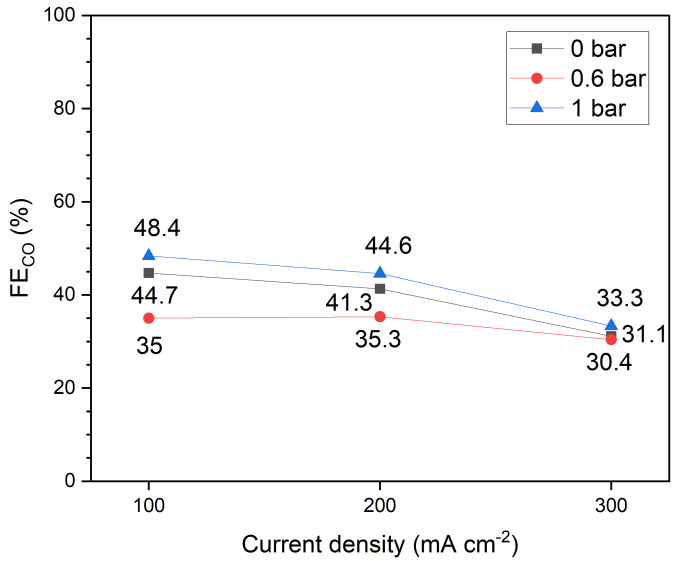

Figure 4.17: Calculated FE of CO produced from regenerated CO_2 at increasing current densities in backpressure conditions of 0 bar (black), 0.6 bar (red) and 1 bar (blue).

CO_2, intensifying mass transport limitations and reducing conversion efficiency. Increasing the back-pressure to 1 bar partially mitigates of the mass transport limitations, increasing the performances. However the improvement is limited, suggesting that higher pressures are likely needed to effectively overcome these limitations.

Influence of temperature

Increasing the reaction temperature typically enhances CO_2RR kinetics, often exponentially. This is a critical consideration since industrial electrolyzers are expected to operate under elevated temperatures potentially reaching 100°C, primarily due to Joule heating. In literature it is shown that the solubility of CO_2 in aqueous solution decreases with temperature whereas HER accelerates [87]. To evaluate this trade-off, the electrolyzers performances are compared in two moderate temperature condition at 40 $°C$ and 60 $°C$. These were tested against a room temperature (25 $°C$) condition, all at 200 mA cm^{-2} current density. Gas chromatography results are plotted in Figure 4.18.

The results show that the electrolyzer's performance improved at 40 $°C$, reaching FE_{CO} of 48%. Nonetheless, at 60 $°C$, the performance declined. These findings indicate that the optimal operating temperature for this bicarbonate electrolyzer is 40 $°C$. This aligns with existing literature, which suggests that while moderate temperature can improve performance, higher temperatures lead to a decline. Which can be related to a reduced solubility of CO_2 in bicarbonate over 60 $°C$ [87], limiting the effective regeneration of iCO_2 in the cathodic compartment. Therefore, for an optimized bicarbonate electrolyzer, it is crucial to maintain a moderate operating temperature.

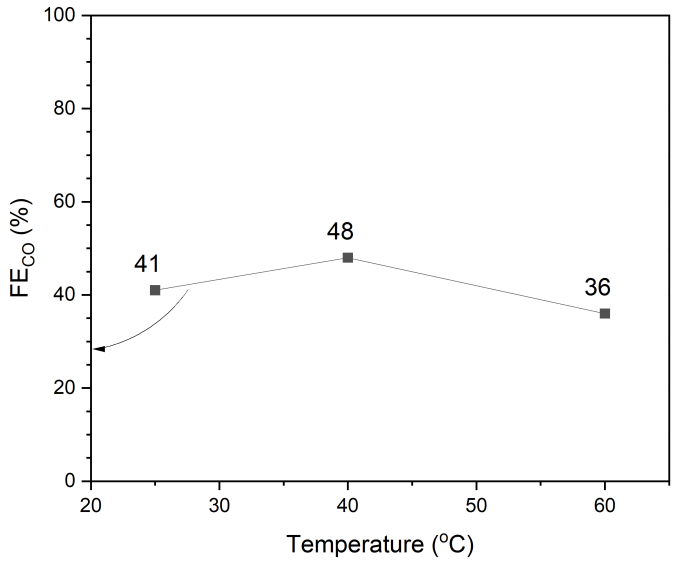

Figure 4.18: FE of CO (black) at increasing operating temperature maintaining a current density of 200 mA cm^{-2}.

Conclusions

The performance of the electrolyzer is directly dependent on its external operating conditions. While backpressure increases the residence time of reactants, giving them more opportunities to react, it must be high enough to overcome the mass transport limitations that occur at higher current densities. The experiments showed that these limitations require elevated partial pressures of CO_2, which were not achievable with the current laboratory setup. Therefore, at the present scale of the prototype, the application of backpressure did not have a significant impact on performance.
Temperature proved to be effective at enhancing electrolyzer performance, but with clear limitations. Performance improved in a small window of moderate temperatures, with optimal results observed at 40 °C. However, increasing the temperature beyond this point caused a decline in performance. This suggests that while moderate temperatures can be beneficial, high temperatures could be detrimental to the overall efficiency of the electrolyzer.
Considering the conducted tests and considerations the optimal condition for the bicarbonate electrolyzer with a double layer Ag electrode is at **40 °C**.
The obtained results are comparable to what is found in literature (Table 4.4).

Table 4.4: Results of FE towards CO from different works in literature of bicarbonate electrolyzers using Ag nanoparticles electrodes binded with Nafion at 200 mA cm^{-2}.

Work	Catalyst loading (mg cm^{-2})	FE$_{CO}$ (%)
Xiao et al. (2023) [41]	3	46
Kim et al. (2024) [65]	2	37
Fu et al. (2025) [88]	5	33.3
This work	3.3 (40 °C)	48*

*: the FE reported is an approximated value due to GC limitations.

Chapter 5

Low cost energy efficient reactive carbon capture alternative

In this chapter, a low-cost, energy-efficient alternative to Ag-based electrodes in bicarbonate electrolyzers will be examined. Noble metals, such as silver, have demonstrated high catalytic efficiency but remain impractical due to cost and scalability limitations for industrial appliactions. To enable large-scale deployment of electrolyzers, it is essential to explore and evaluate more affordable alternatives.
As discussed in Section 2.2.2, transition metals represent one such option. Eventhough transition metals on their own exhibit limited catalytic activity, their metal–organic derivatives can display augmented performances. In particular, cobalt and its derivative, cobalt phthalocyanine (CoPc), have been tested and analyzed in the literature. When combined with suitable carbon supports, these compounds achieve high catalytic efficiencies, with gas-fed electrolyzers reaching FE_{CO} values of up to 92% [89]. Observing good performances in gas-fed electrolyzers, these modified single atom catalysts (SACs) are tested and optimized to be implemented in a bicarbonate electrolyzer. CoPc can be applied either as a homogeneous electrocatalyst, dissolved directly in the electrolyte, or as a heterogeneous electrocatalyst, immobilized on the electrode surface. For large-scale applications, the heterogeneous approach is preferred, as it enables the utilization of a GDE. The following sections focus on studying and optimizing the performance of heterogeneous CoPc catalysts.

5.1 Hierarchically designed MWCNT-supported CoPc

This section discusses the production and effectiveness of MWCNTs as a carbon support, comparing their performance with that of bare CoPc and optimized Ag-based electrodes examined in Chapter 4.

5.1.1 Materials and methods

Catalyst fabrication

Carbon supported SACs are produced and deposited on a carbonic gas diffusion layer to get a GDE that is then tested in the bicarbonate electrolyzer. Different ratios of MWCNT (Sigma Aldrich) and CoPc particles (Sigma Aldrich 97%) are mixed in N,N Dimethylformamide (DMF, Sigma Aldrich 99.8%) to allow the catalyst and the support to interact with $\pi - \pi$ bonding. The ratios are defined from literature and the quantities are reported in Table 5.1

Table 5.1: Ratios and quantities of CoPc and MWCNT used for supported powder production.

Sample	m_{CoPc} (mg)	m_{MWCNT} (mg)	Article
CoPc-CNT 1:3	13	30	Wang et al. (2017) [90]
CoPc-CNT 4:6	20	30	Choi J. et al. (2019) [91]

The CoPc-MWCNT 1:3 is obtained combining 13 mg CoPc nanoparticles dispersed into 20 mL of DMF, and 30 mg of previously sonicated MWCNT dispersed in 30 mL of DMF. The ultrasound waves expand the MWCNT structure allowing for more graphitic structure to be exposed, maximizing the interaction with CoPc. Therefore maximizing $\pi - \pi$ interactions between the catalyst and the support.
The CoPc-MWCNT 4:6 is obtained combining 20 mg CoPc nanoparticles dispersed into 20 mL of DMF, and 30 mg of previously sonicated MWCNT dispersed in 30 mL of DMF. The combined solutions are stirred at 140 °C for 24h under a fume hood. The reaction temperature allows the reduction of the energetic barrier for interaction between MWCNT and CoPc.

After the final solutions are cooled with ice, the resulting powder is precipitated using a centrifuge. The remaining DMF solvent is then analyzed with UV-vis spectroscopy to identify any residual, unreacted CoPc.
The precipitated powder is washed with methanol, to remove any remaining DMF, and centrifuged until the solution runs clear. The resulting powders are dried in a Buchi vacuum oven at 60°C for one hour. Figure 5.1 schematically illustrates the synthesis process for these powders.

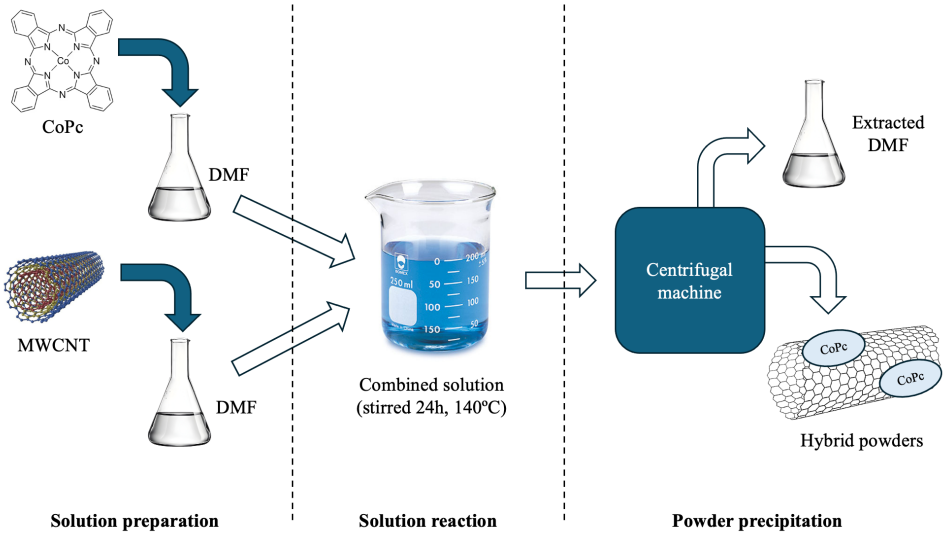

Figure 5.1: Schematic diagram of the synthesis process for producing MWCNT-supported CoPc powder via solution preparation and precipitation.

Electrode Manufacturing

The MWCNT-supported CoPc powder is spray-coated onto a 5 cm^2 Freudenberg H23 carbon paper substrate. The spraycoating ink is prepared by dispersing 12 mg of the powder and 270 μL of a 5 wt% Nafion binder solution in 10 mL of methanol. Strong particle interaction within

the catalyst makes it difficult to disperse in methanol. To overcome this, a 1:1 mass ratio of catalyst to binder is necessary. The resulting ink is then sonicated for three hours to create a uniform, well-dispersed system.
Spraycoating is performed using a Nadatech Innovation™ spraycoating machine. To ensure a uniform deposition and minimize particle aggregation, the inks are deposited in 2 mL increments, while the remainder of the ink is kept in an ultrasound bath. This process yields two CoPc-MWCNT electrodes with catalyst loadings of 2.0 mg cm^{-2}, one at a 1:3 ratio and the other at a 4:6 ratio.

For comparison, a bare CoPc electrode (b-CoPc) is also manufactured following the Ag nanoparticle electrode recipe. The coating ink for this electrode is composed by 4 mL of IPA, 30 mg of CoPc particles (Sigma Aldrich 97%) and 77.8 μL and 5 wt% Nafion solution. The ink is sonicated for 30 minutes and spraycoated on a 5cm^2 square Freudenberg H23 carbon paper, obtaining a catalyst loading of 2.9 mg cm^{-2}.

Electrochemical tests and characterization

The b-CoPc electrode and CoPc-MWCNT 1:3 and 4:6 electrodes are tested on the generic test bench (section 3.2.1). The setup utilized a zero-gap MEA setup with 3M $KHCO_3$ as catholyte and 0.05M H_2SO_4 as anolyte. Chronopotentiometry is performed on the cell applying a constant current of 200 mA cm^{-2} and monitoring the cell voltage. During these tests, gaseous products were analyzed using a Micro-GC. Additionally, EIS and the calculated parameters (section 4.1.2) are used quantify interfacial electronic properties.
To characterize the synthetized material, FESEM images are obtained to evaluate the catalysts morphology and role of the carbon supports. XPS provides a superficial chemical analysis, enabling a quantification of each element and their characteristics. In particular, detailed observation of the Carbon C1s peak and shifts of peaks offer information about the $\pi - \pi$ interactions and possible defects. To complete chemical and physical characterization, XRD measurements are also conducted on the produced powders compared to commercial CoPc. XRD allows for the determination of composing phases of the material but also the determination of possible defects and crystallinity of the system. Residual DMF from the centrifugation of the solution is analyzed using UV-vis spectroscopy to identify the amount of CoPc that hasn't bonded with MWCNTs.

5.1.2 Results and Discussion

Electrochemical results

The CoPc-MWCNT 1:3 and 4:6 electrodes are tested inside the bicarbonate electrolyzer and compared to the b-CoPc electrode on the generic bench setup described in Section 2.2.2. They are tested at constant 200 mA cm^{-2} applied current density, changing electrolyte solution and buffer layer between each test. Calculated FEs are plotted in Figure 5.2

A distinct difference in performance is observed: the b-CoPc electrode showed no catalytic activity, whereas the CoPc-MWCNT electrodes achieved a FE_{CO} of up to 7%. Although this performance remains below that of Ag-based electrodes, it demonstrates the effectiveness of carbon supports. One possible reason to explain such results, is the $\pi - \pi$ bonding between CoPc and the MWCNTs limits aggregation and helps stabilize adsorbed CO_2. However, as noted during the Electrode Manufacturing section, the CoPc-MWCNT catalyst exhibits strong intermolecular interactions, which required a large quantity of binder for efficient dispersion.

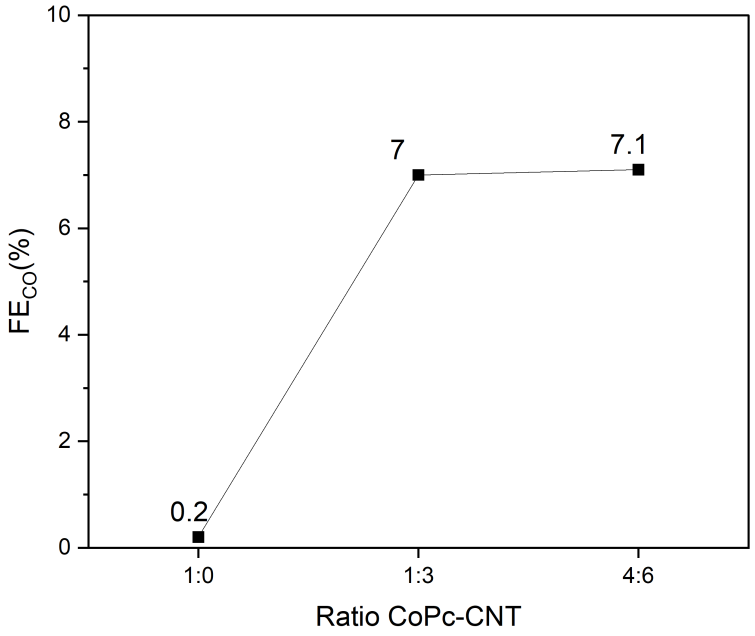

Figure 5.2: FE of CO of CoPc-MWCNT electrodes tested at 200 mA cm^{-2}.

Given that the binder itself has no catalytic activity, a high concentration of it can limit the electrode's overall effectiveness. Further characterizations are conducted to investigate the effects of the excessive binder and the properties of the CoPc-MWCNT catalyst.

UV-visible spectroscopy

UV-visible spectroscopy was used to determine the amount of unreacted CoPc lost in the solvent (i.e. DMF) after the precipitation has been forced through centrifugation. This step helps define the effective quantity of CoPc that reacted with the MWCNTs, to confirm the production of the desired product. CoPc exhibits a strong blue color when dissolved in a solvent such as DMF, which can be monitored using UV-visible spectroscopy.
To quantify the remaining CoPc in the solvent, serial dilutions of a mother solution were prepared. Considering a saturation concentration of 0.11 mg mL^{-1} of CoPc in DMF, the mother solution is made by mixing 50 mL of DMF and 1.16 mg of CoPc. This solution was then diluted to 1/2, 1/5, 1/10, 1/20, and 1/50 of its initial concentration. The maximum absorbance for each dilution was measured and plotted against its relative molarity [M]. A linear fitting is obtained from the low-molarity points, shown in Figure 5.3. The measured absorbance of the DMF sample from the CoPc-MWCNT 1:3 solution is reported in Figure 5.3, along with its molarity determined from the linear fitting.

From the maximum absorbance, the molarity of the solution ($M_{CoPc-MWCNT}$) is determined through the linear fitting. The mass of unreacted CoPc ($m_{unreactCoPc}$) is obtained using the following equation:

$$m_{unreactCoPc} = M_{CoPc-MWCNT} \cdot V_{sample} \cdot M_{CoPc} \tag{5.1}$$

Where V_{sample} is the volume of the sample and M_{CoPc} the molecular weight of CoPc. The result is that **0.55 mg** of CoPc didn't react. Considering the initial mass of pure CoPc being 13

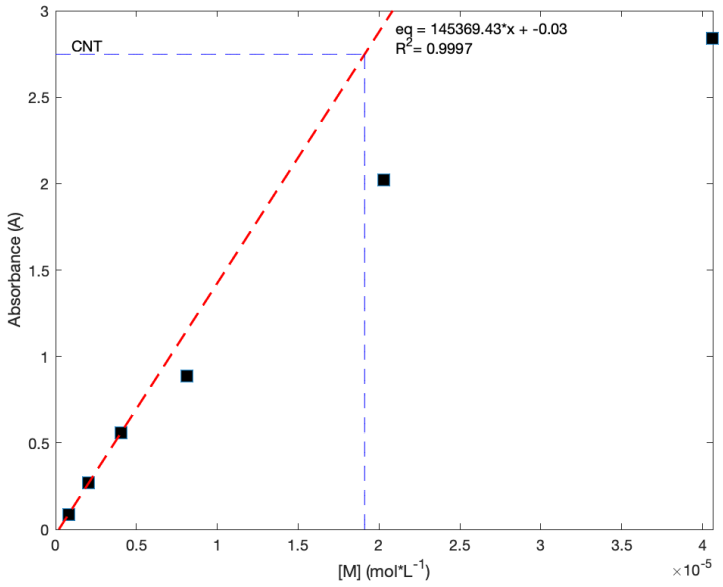

Figure 5.3: Linear fitting (dotted line) of the maximum absorbance of each CoPc-DMF dilution (black) with the maximum absorbance of the DMF solvent of the CoPc-MWCNT 1:3 powder. Equation and R^2 value are reported in the graph.

mg, only 4% of the mass was lost in the solvent. The UV-vis spectroscopy allows us to say that the produced powders have indeed the correct ratios and that the laboratory procedure doesn't generate significant material losses.

FESEM characterization

FESEM characterization is carried out to compare the surface morphology of pure CoPc with that of the produced supported catalyst. Initially, the spray-coated pure CoPc GDE is analyzed to observe the intrinsic aggregation of CoPc, as shown in Figure 5.4.

The intrinsic aggregation of CoPc is evident by the formation of organized shard-like structure. At lower magnifications (Figure 5.4a.), the powder covers the fibers and the empty space between them. These results differ significantly from the observed Ag-based electrodes in previous sections, a consequence of organized CoPc structures. This strong aggregation can be linked to very low electrode's performance, intermolecular bonding is prioritized creating aggregated structures.

To demonstrate different spatial conformation, the produced CoPc-MWCNT 1:3 catalyst is also observed with FESEM technique. The obtained results (Figure 5.5b) are compared with FESEM imagery of pristine MWCNT powder (Sigma Aldrich) shown in Figure 5.5a.

MWCNT are highly graphitic and anisotropic material. FESEM results of the pristine MWCNT sample show tubular-like structures, that form extended networks due to strong particle interaction. The supported catalyst displayed similar extended structures, with no sign of phase separation or structural changes. This suggests that CoPc molecules cover the MWCNT support rather than forming a separate phase.

Overall, the integration of MWCNT supports limits the aggregation of CoPc in organized shard structures. Given the anisotropic nature of MWCNTs, the formation interlacing tubular-like structures is observed in the powder. This structural arrangement may be an initial insight into the limited electrochemical performance, as the interlacing could reduce the number of acces-

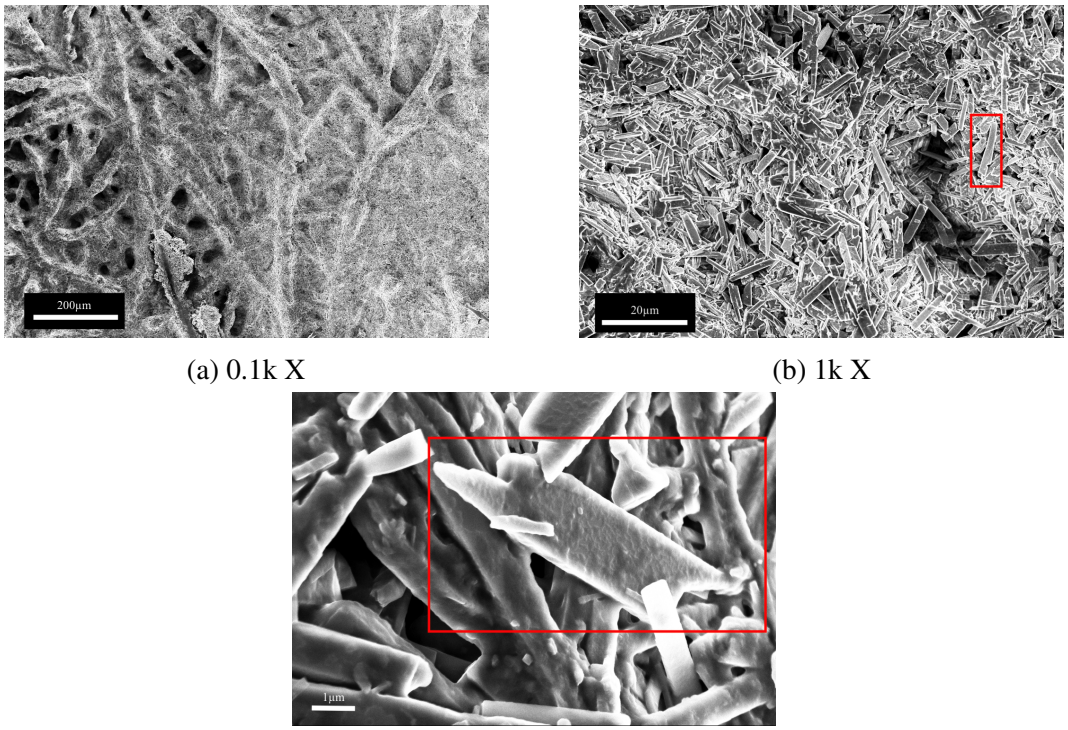

(a) 0.1k X

(b) 1k X

(c) 10k X

Figure 5.4: FESEM images (secondary electron mode, 5 kV) of CoPc spraycoated onto H23 carbon paper. In the red squares are highlighted the agglomerated structures.

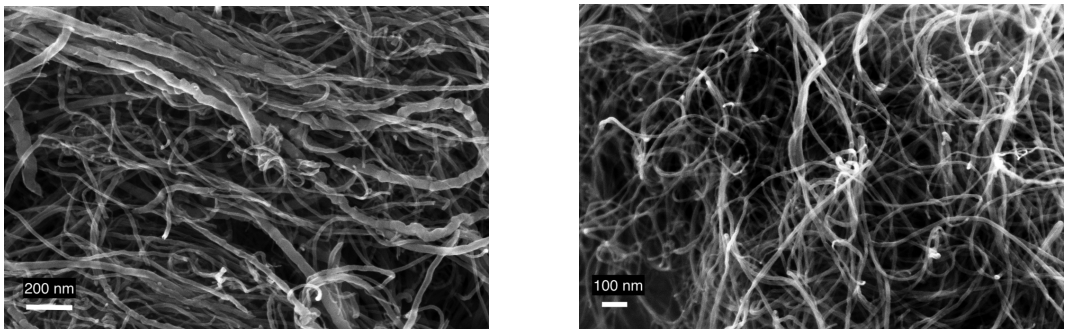

(a) MWCNT sample at 50k X

(b) CoPc-MWCNT 1:3 sample at 50k X

Figure 5.5: FESEM images (secondary electron mode, 5 kV) of pristine MWCNT and CoPc-MWCNT 1:3 samples at 50k X magnification.

sible active sites, despite the efficient interaction between the catalyst and the graphitic support.

XPS analysis

XPS analysis is a useful technique to study the surface chemical composition of a sample by measuring the interaction of X-rays with core electrons. The resulting spectra correspond to the binding energies of specific atoms, which makes it possible to determine the surface elemental composition. A closer examination of individual peaks also provides information on atomic interactions. In this case study, XPS is used to verify the correct elemental composition of the produced powders and investigate possible $\pi - \pi$ interaction. An initial survey spectra is collected of both pure CoPc powder and the CoPc-MWCNT 1:3 catalyst Characteristic peaks

are identified using the NIST (National Institute of Standards and Technology) database and the Handbook of X-ray Photoelectron Spectroscopy [92].
The survey spectra of pure CoPc with the identified elements as labels is reported in Figure 5.6.

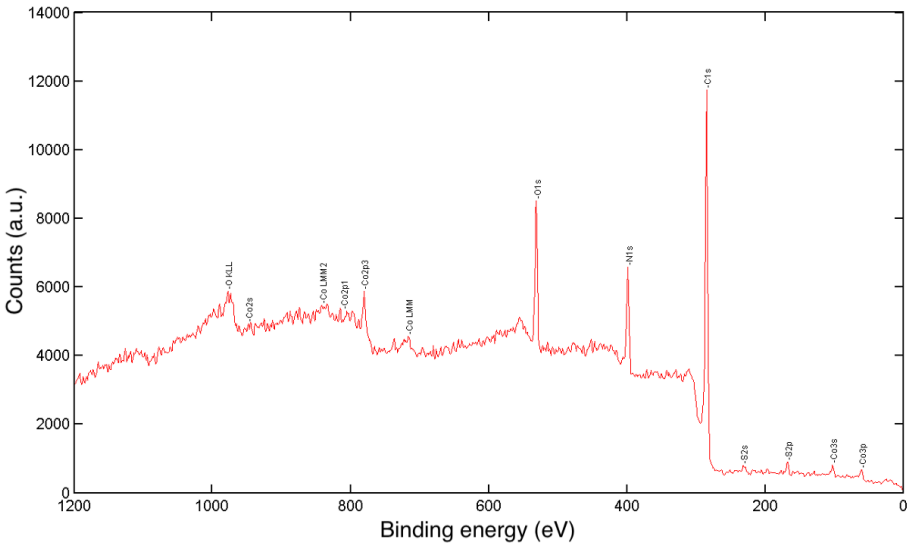

Figure 5.6: Labelled survey spectra of CoPc obtained via XPS analysis.

From this wide range analysis, the main elements of CoPc are identifed: cobalt, nitrogen, oxygen and carbon with traces of sulphur. Cobalt is identified by its signature 2p, 3s and 3p electronic orbitals peaks. Carbon is clearly visible as the primary element in the molecule structure. Oxygen is also detected through its 1s electronic orbital and Auger energy peaks. Since oxygen is not part of the intrinsic composition of CoPc, this indicates surface oxidation or oxygen bonding. The signal isn't perfectly sharp likely due to possible disturbances on the surface and the fact that the sample is analyzed in powder form.
Based from the survey, a more in detail High Resolution (HR) analysis is performed on specific peaks. The HR scans the emitted photoelectrons with a smaller energy interval allowing for more precise peaks. The selected analyzed peaks are carbon C 1s at 284.5 eV, oxygen O 1s at 532.1 eV , nitrogen N 1s at 398.9 eV and cobalt Co 2p at 780.1 eV and 796.1 eV, shown in Figure 5.7

After substracting the identified baseline for the HR spectra, the area of the peaks is calculated through the trapezoid method (equation 5.2). The equation considers an integration range [a,b] and n number of intervals :

$$\int_a^b f(x)dx \approx \frac{b-a}{n}\left(\frac{f(a)+f(b)}{2} + \sum_{k=1}^{n-1} f\left(a + k\frac{b-a}{n}\right)\right) \tag{5.2}$$

The calculated areas of each HR peak are normalized using identified RSF (Relative Sensitivity Factors) from The Handbook of X-ray Photoelectron Spectroscopy [92]. The fraction of normalized areas represents the atomic concentration of the specific element, transcribed in Table 5.2.

Given the chemical formula of CoPc ($C_{32}H_{16}CoN_8$), the results are coherent with the expected atomic concentration. Oxygen, which is not part of the formula, was detected at 11.7% and can be attributed to surface contamination. The measured cobalt concentration was relatively low at 2.9%, suggesting that the catalytic activity is largely linked to the organometallic structure rather than the metal content alone. The absence of strong contamination and low

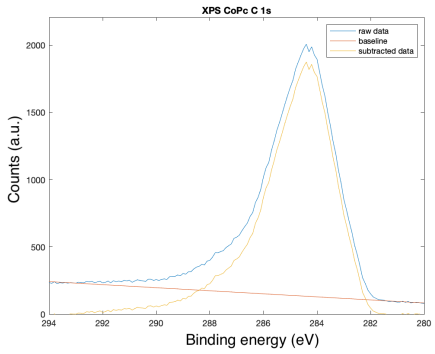

(a) HR spectra of C 1s

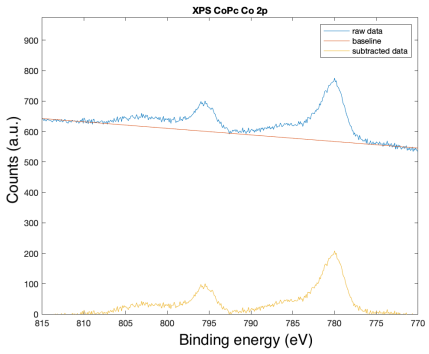

(b) HR spectra of Co 2p

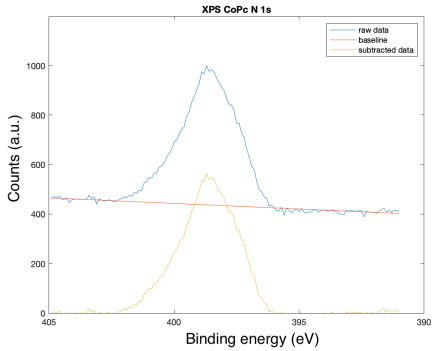

(c) HR spectra of N 1s

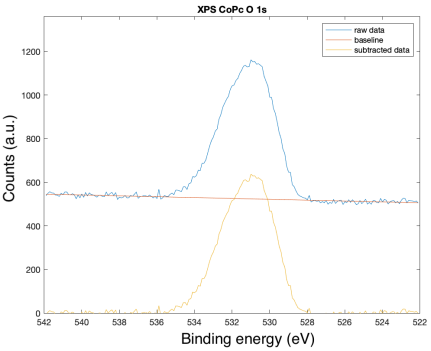

(d) HR spectra of O 1s

Figure 5.7: HR spectra of CoPc sample. C 1s, Co 2p, O 1s and N 1s plotted with the measured data, the calculated baseline and the subtracted baseline.

Table 5.2: Atomic concentration of each identified element of the CoPc sample obtained from the areas of HR peaks normalized with RSFs.

Element	Area (-)	RSF (-)	Atomic concentration (%)
C 1s	5840	0.314	73.6
Co 2p	1530	2.113	2.9
N 1s	1490	0.499	11.8
O 1s	2160	0.733	11.7

oxygen concentration suggest high purity of the pristine powder as reported by Sigma Aldrich. To evaluate the influence of the MWCNT carbon support, the CoPc-MWCNT 1:3 sample is analyzed and compared with pure CoPc. The labelled survey spectra of the CoPc-MWCNT 1:3 sample is reported in Figure 5.8:

The survey spectra identifies the same elemental species of CoPc but the carbon C 1s peak is noticeably more intense. Oxygen is also detected as for the pure CoPc sample indicating here too a possible superficial oxidation or oxygen interaction. Comparing to the CoPc sample survey spectra, 3s and 3p orbitals are hardly discernible but the 2p orbital is still observable.
To elementally quantify the sample, a HR analysis is conducted on the same peaks as for the b-CoPc sample. The resulting HR peaks with the calculated baseline are reported in Figure 5.9.

After subtracting the baseline, the area of the peaks is obtained through the trapezoid method (equation 5.1). The fraction of RSF normalized areas define the atomic concentrations, shown in Table 5.3.

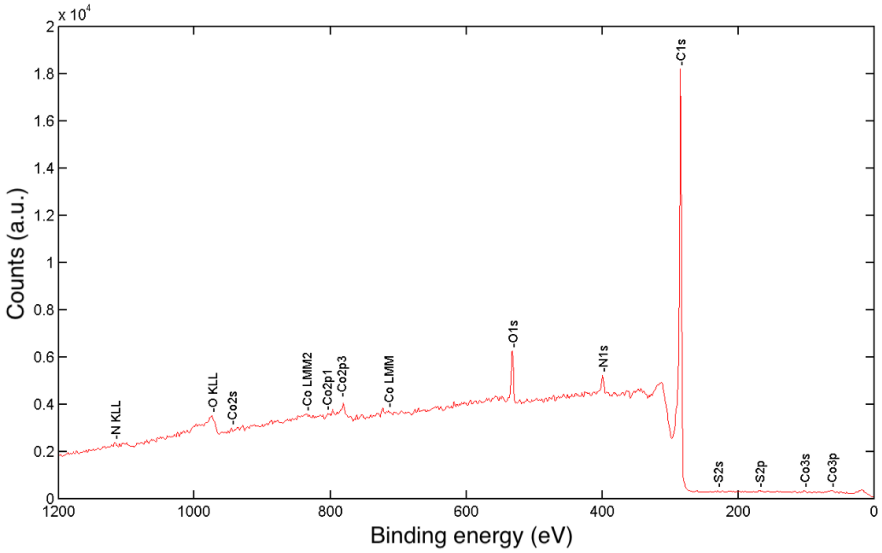

Figure 5.8: Labelled survey spectra of CoPc-MWCNT sample obtained via XPS analysis.

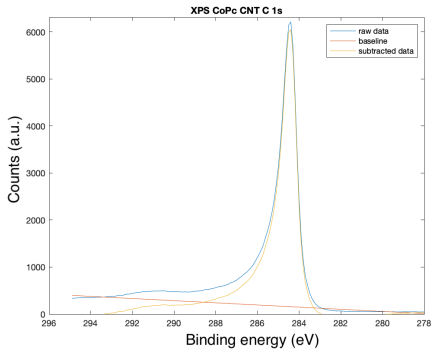

(a) HR spectra of C 1s

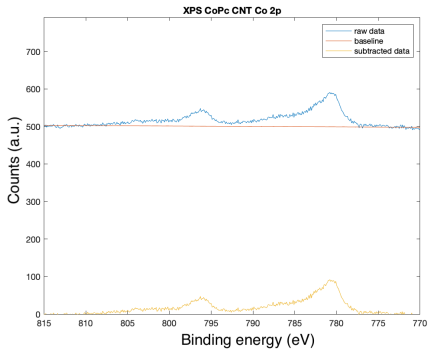

(b) HR spectra of Co 2p

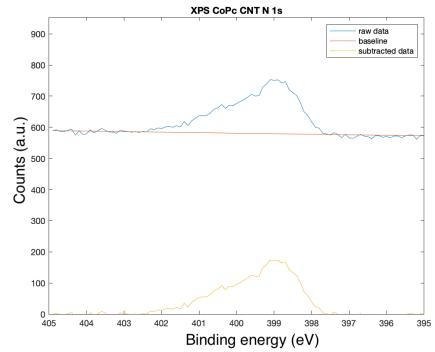

(c) HR spectra of N 1s

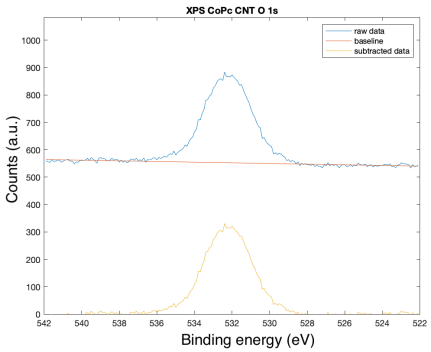

(d) HR spectra of O 1s

Figure 5.9: HR spectra of CoPc-MWCNT sample. C 1s, Co 2p, O 1s and N 1s plotted with the measured data, the calculated baseline and the subtracted baseline.

As observed with the survey spectra: the carbon concentration reached 91.9% while the cobalt concentration dropped to 1.2%. Also, the oxygen concentration is lower, a possible indicator that the surface interacts less with oxygen.
The XPS analysis is quantitative in its nature, however measured spectra are the result of complicated overlapping signals from different oxidation states, deviating from ideal behaviour.

Table 5.3: Atomic concentration of each identified element of the CoPc/MWCNT sample obtained from the areas of HR peaks normalized with RSFs.

Element	Area (-)	RSF (-)	Atomic concentration (%)
C 1s	8770	0.314	91.9
Co 2p	780.9	2.113	1.2
N 1s	357.4	0.499	2.4
O 1s	1020	0.733	4.5

The presence of defects or other bonds alter the core electrons shifting and broadening the signal peaks [93]. Comparing the HR spectra of Co 2p 1/2 and 3/2 of both pristine CoPc and CoPc-MWCNT sample it is possible to observe differences between the two peaks distance (Figure 5.22).

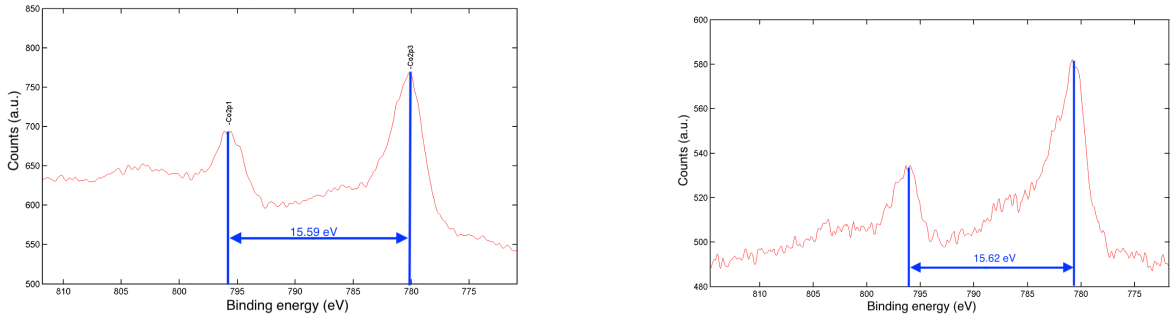

(a) CoPc sample

(b) CoPc-MWCNT 1:3

Figure 5.10: Comparison between the Co 2p 1/2 and 3/2 distance in the HR spectra of both pristine CoPc and CoPc-MWCNT sample.

Schmid et al. [94] have demonstrated that a multilayer of CoPc molecules showed a 15.7 eV gap between Co 2p 1/2 and 3/2 maxima, and a submonolayer of CoPc molecules exhibited only a 14.8 eV gap. Desiring a reduced agglomeration of CoPc molecules, the ideal result should be a gap comparable to 14.8 eV. Pristine CoPc exhibits multilayer structure, with a 15.59 eV gap between the peak's maxima, in agreement with literature. In the CoPc-MWCNT 1:3 sample, the measured gap is 15.62 eV, suggesting a multilayer of CoPc considering the literature works. These results suggest a stacking of CoPc molecules on the MWCNT and not obtaining an even distribution. However, a positive shift of the peaks values is observed, that can be related to Co and O bonds and $\pi - \pi$ interactions between CoPc and MWCNT [95].

Peak fittings of the HR spectra, called **deconvolutions**, allow for precise observation of peak alterations. These deconvolutions are various from simple symmetric Gaussian distribution to more complex asymmetrical Doniach–Sunjic model [96]. In this case study, the most impactful results can be obtained from the C 1s peak. In the works of Briggs and Beamson (1992) [97], it has been noted how different bonds between carbon and heteroatoms shifts the XPS signal and modifies the peak. In more recent studies [98], it is observed that a deconvolution the C 1s peak identifies sp^2 carbon bonds with a narrow peak at 284.4 eV, sp^3 carbons and defects with a second peak near 285.5 eV, and $\pi - \pi*$ transitions with a third peak at higher energies.
Following these considerations, the obtained HR C 1s peak of both CoPc and CoPc-MWCNT 1:3 are studied. The peaks are deconvoluted with a specific XPS program using gaussian dis-

tribution (equation 5.3) where a is the height of the curve, b is the position of the center of the peak and c is the standard deviation.

$$f(x) = ae^{-\frac{(x-b)^2}{2c^2}} \tag{5.3}$$

The resulting deconvolution of both C 1s peaks are shown in Figure 5.11.

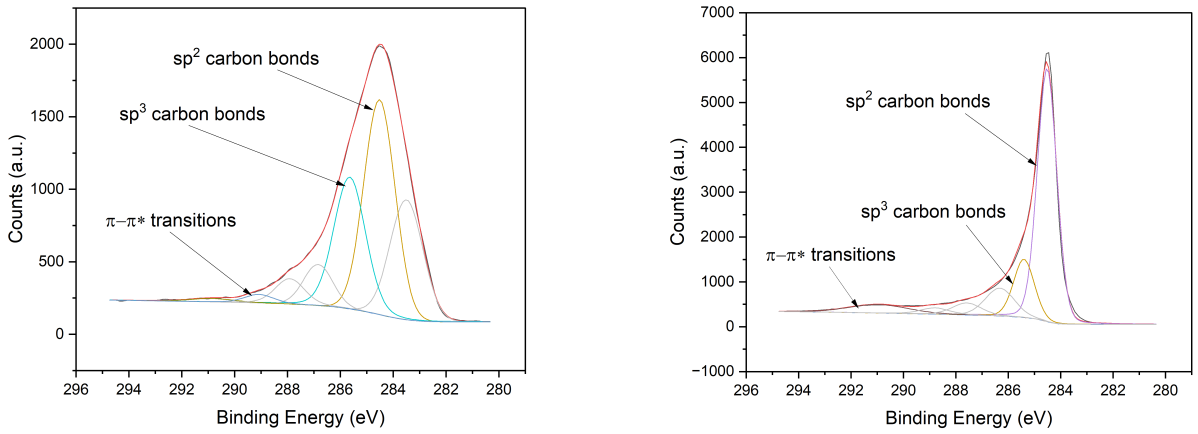

(a) CoPc sample

(b) CoPc-MWCNT 1:3

Figure 5.11: Deconvolution of HR spectra of C 1s peaks of CoPc sample and CoPc-MWCNT 1:3. Three peaks are obtained relative to sp^2 carbons, to sp^3 carbons and defects, and to $\pi - \pi*$ transitions.

In the CoPc-MWCNT sample, the sp^2 carbon peak appears narrower and more intense, consistent with the introduction of MWCNTs, which are highly graphitized materials. A second important information concerns the extension of the $\pi - \pi*$ electron transition peak. In the CoPc-MWCNT 1:3 sample, the peak becomes more intense shifting to higher energies modifying the curves shape, which reflects stronger π–π interactions. While such interactions are already present in CoPc due to its aromatic structure, they are further enhanced when MWCNTs are incorporated.
In graphitic structures, the presence of sp^3 hybridized carbons are sign of defects, being reactive carbons and can bond with different atoms or molecules. The peak associated with defects remains essentially unchanged. In pure CoPc, it originates from sp^3 carbons bonded to nitrogen, while in the CoPc-MWCNT 1:3 sample it also includes contributions from sp^3 carbons located at the MWCNT tips. A slight increase in intensity is observed, consistent with this additional contribution. To conclude, the XPS analysis allowed to quantify the elemental composition but also revealed atomic interactions. HR analysis of the Co 2p peak highlights the presence of CoPc molecule stacking, indicating the presence of ordered structures on the carbon support. A close description of C 1s peak defined the π–π interactions and intensity in the CoPc-MWCNT 1:3 which can be related to intermolecular bonding between catalyst and MWCNTs and also to the observed molecules stacking.

XRD Analysis

In this study, XRD is used to determine the crystalline phase of pure CoPc, helping to explain the organized structures observed with FESEM. The results are compared with the produced catalyst powder to evaluate the effect of MWCNT supports on the material.

In Figure 5.12 are shown the XRD spectra of pure CoPc (Sigma Aldrich 97%) plotted using a MatLab program.

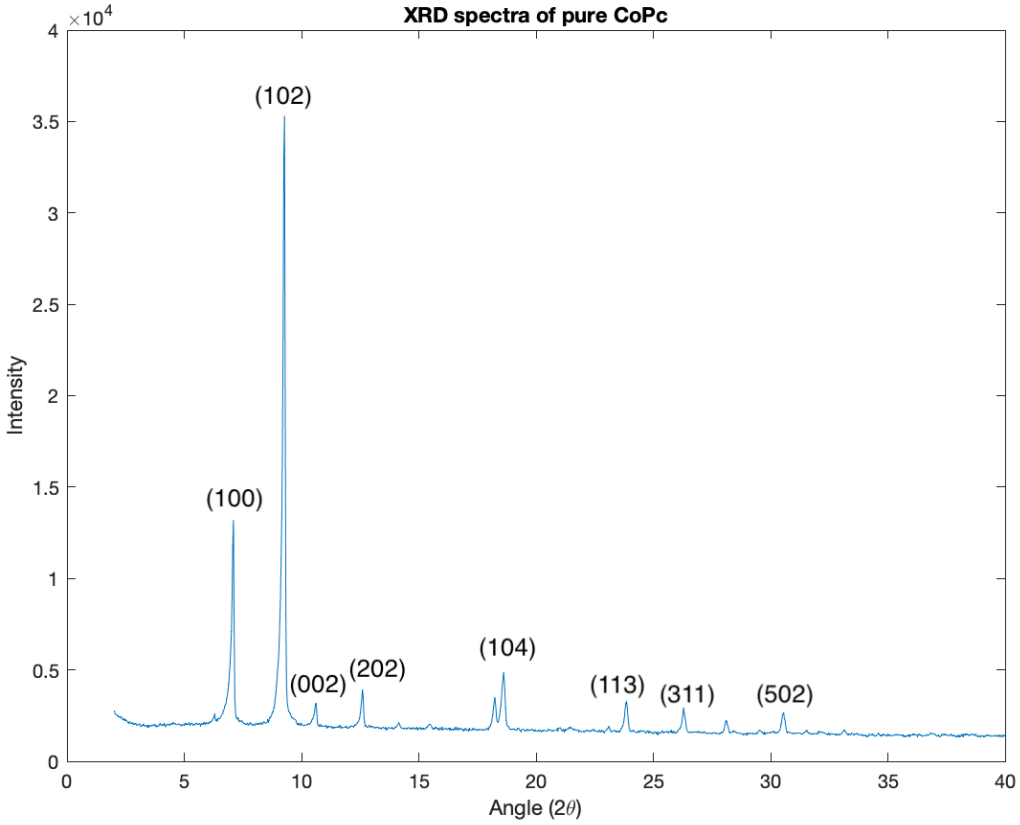

Figure 5.12: XRD measurement results of pure CoPc.

To determine the composing phase of the CoPc sample, the measured peaks are analyzed with a MatLab program and Fityk software. The resulting data is then compared with ICCD cards (International Centre for Diffraction Data). These cards provide the characteristic peak angles and the relative intensity for a specific crystalline phase, allowing for phase identification. CoPc is characterized by two main crystalline phase: α-CoPc (ICCD card No. 44-1994) and β-CoPc (ICCD card No. 14-0948) [99].
The corresponding cards for each phase and the measured relative intensity peaks at specific angles are transcribed in Table 5.4.

Comparing the results with the specific phases it appears that the pure CoPc sample is composed of a single β-CoPc phase. It is characterized by a monoclinic structure with cell parameters: a=14.5982 Å, b=4.7937 Å, c=19.4348 Å, β =120.782°, and Z=2 [100]. In Figure 5.13 is represented how CoPc molecules stack in the β crystalline phase.

The XRD pattern of pure CoPc was then compared with that of the CoPc–MWCNT 1:3 powder to evaluate the effect of the carbon support on crystallinity and structural properties, shown in Figure 5.14. The resulting measurements and relative crystallographic orientation are plotted using a Matlab program.

The most intense β-CoPc peaks remain visible at 7.09° and 9.28° but the relative ratio between the peaks isn't the same as in pristine CoPc. Variations in the peaks shape and intensity are sign of a modified crystallographic structure. Both peaks are compared on a normalized scale respect to the maximum intensity peak at 9.28° reported in Figure 5.15.

Table 5.4: Experimental Braggs angles with relative intensity compared to ICCD card No. 44-1994 for α-CoPc and 14-0948 for β-CoPc.

ICCD card No. 44-1994 for α-CoPc		ICCD card No. 14-0948 for β-CoPc		Experimental results	
2Θ	I/I_0	2Θ	I/I_0	2Θ	I/I_0
6.8	1	-	-	-	-
-	-	7.072	0.95	7.097	0.374
7.3	0.72	-	-	-	-
-	-	9.26	1	9.275	1
-	-	10.607	0.16	10.621	0.089
-	-	11.582	0.06	-	-
-	-	12.591	0.3	12.598	0.111
-	-	14.102	0.06	14.145	0.059
-	-	15.464	0.06	15.491	0.057
15.6	0.26	-	-	-	-
16.2	0.24	-	-	-	-
-	-	18.254	0.45	18.242	0.099
-	-	18.68	0.4	18.614	0.138
-	-	21.102	0.4	-	-
-	-	21.622	0.1	-	-
-	-	22.337	0.02	-	-
-	-	23.162	0.08	-	-
-	-	23.92	0.4	23.857	0.092
24.1	0.29	-	-	-	-
24.8	0.14	-	-	-	-
25.3	0.2	-	-	-	-
-	-	26.368	0.3	26.292	0.082
26.8	0.46	-	-	-	-
27.8	0.58	-	-	-	-
-	-	28.24	0.16	-	-
-	-	28.517	0.06	28.526	0.045
-	-	29.679	0.04	29.758	0.04
-	-	30.724	0.2	30.761	0.046

The CoPc-MWCNT 1:3 sample shows different ratios between the 7.09° and 9.28° peaks and different shapes compared to pristine CoPc sample. This indicates a different crystalline structure compared to pure CoPc. The CoPc-MWCNT 1:3 sample (100) and (102) peaks are characterized by a wider shape given by multiple contributions, measuring a FWHM of 0.14 and 0.157 respectively. While pristine CoPc exhibits peaks with FWHM of 0.054 and 0.057 at the same angles. The widening of the peaks and modification in the ratios between observed peaks in XRD analysis is as a sign of reduced periodicity in the system modifying the diffraction results.

The CoPc-MWCNT 1:3 sample is also characterized by the broad peak at 26°, which can be associated with the MWCNT support [101]. This peak has a FWHM of 0.974, and the mean crystallite size, calculated using the Scherrer equation, is **9.05 nm**, compared to 19.12 nm for

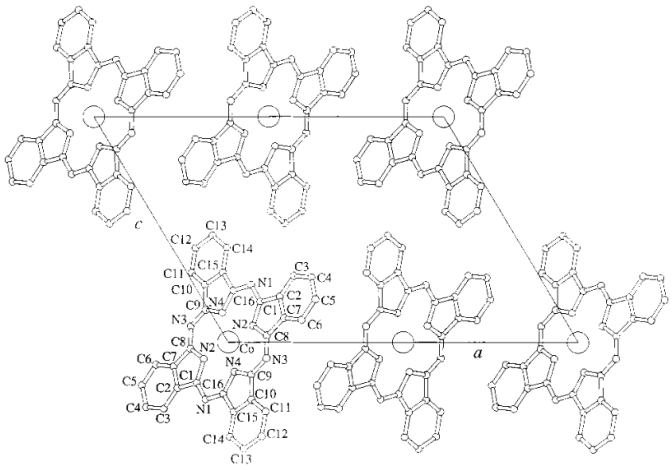

Figure 5.13: Molecular arragement and atomic numbering of β-CoPc along [010] Miller plane. A unit cell is indicated. [100]

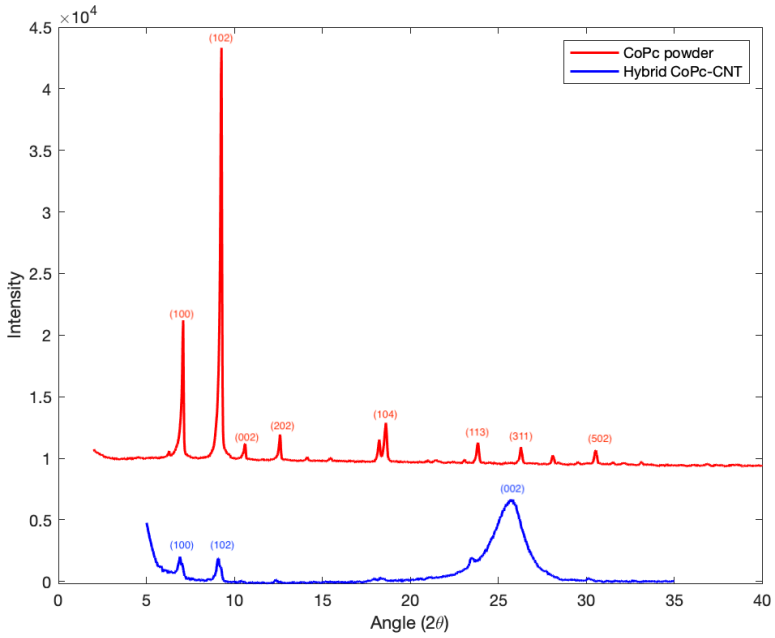

Figure 5.14: XRD measurements of CoPc-MWCNT 1:3 catalyst (blue) compared to pristine CoPc powder (red). β-CoPc signal are still distinguishable in the produced powder with the presence of a wide peak at 26°.

the pure CoPc powder.
Smaller crystallite sizes with modified peak shapes and ratios suggest a reduced crystalline order with loss of periodicity. In pure CoPc, the large crystallites are linked to the shard-like structures observed in the FESEM images. Whereas, in the CoPc-MWCNT 1:3 powder, the covering of the MWCNT with CoPc molecules generated reduced agglomeration. The presence of smaller crystallites in the CoPc-MWCNT 1:3 is supported by previous XPS multilayer observation.

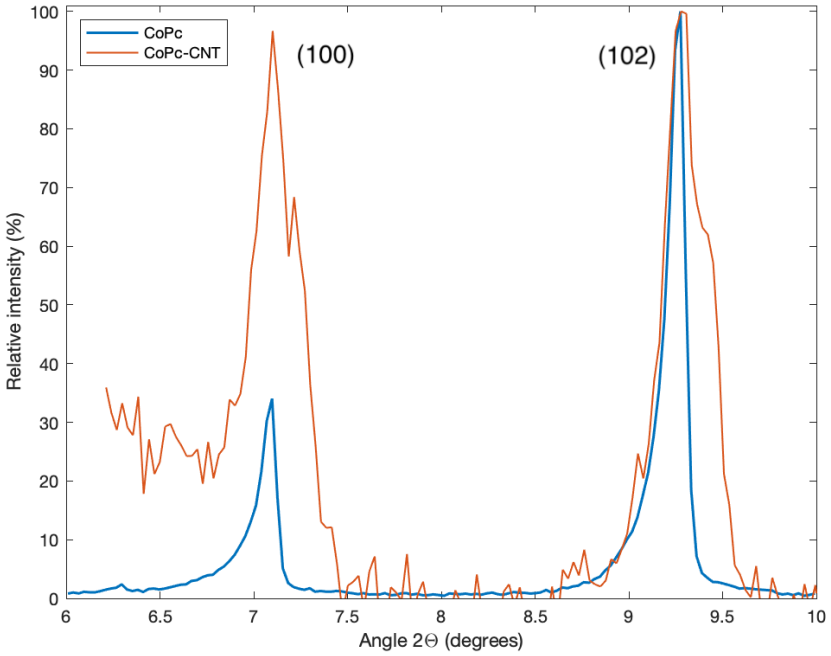

Figure 5.15: Comparison of the 7.09° and 9.28° peaks of both CoPc and CoPc-MWCNT samples on a normalized intensity scale.

EIS analysis

Previous characterizations show an efficient production of supported catalyst but do not completely explain the low catalytic efficiency. A detailed EIS analysis is performed on the CoPc-MWCNT 1:3 electrode to evaluate the effect of excessive binder necessary for the electrode's manufacturing. The procedure follows the methodology described in Section 3.2.3. The resulting spectra are plotted on a Nyquist plot, from which key electrochemical parameters are extracted. As described in previous chapter, the determined parameters are R_{ct} and C_{dl}. They give us insight on the effective active area and the reaction kinetics at the surface of the electrode. The corresponding Nyquist plot are shown Figure 5.16 and calculated parameters R_{ct} and C_{dl} are transcribed in Table 5.5 compared to Ag-based electrodes.

Table 5.5: Measured IES parameters for CoPc-MWCNT 1:3 catalyst compared to Ag-based electrodes.

Electrode	R_{ct} (Ω)	C_{dl} (F)
CoPc-MWCNT 1:3	29.08	1.35E-4
Single layer	40.82	2.53E-4
Double layer	43.57	3.31E-4

The CoPc-MWCNT electrode exhibits a distinct performance compared to previous Ag-based electrodes. The measured R_{ct} value is 10 Ω lower than Ag-based electrodes, an indicator of efficient electron transfer and faster reaction kinetics given by the graphitized support. However, a decreased C_{dl} suggesting a lower density of active sites on the GDE's surface. Notably, the C_{dl} value for the CoPc–MWCNT 1:3 corresponds to only one-third of the effective active area available in the double-layer electrode.

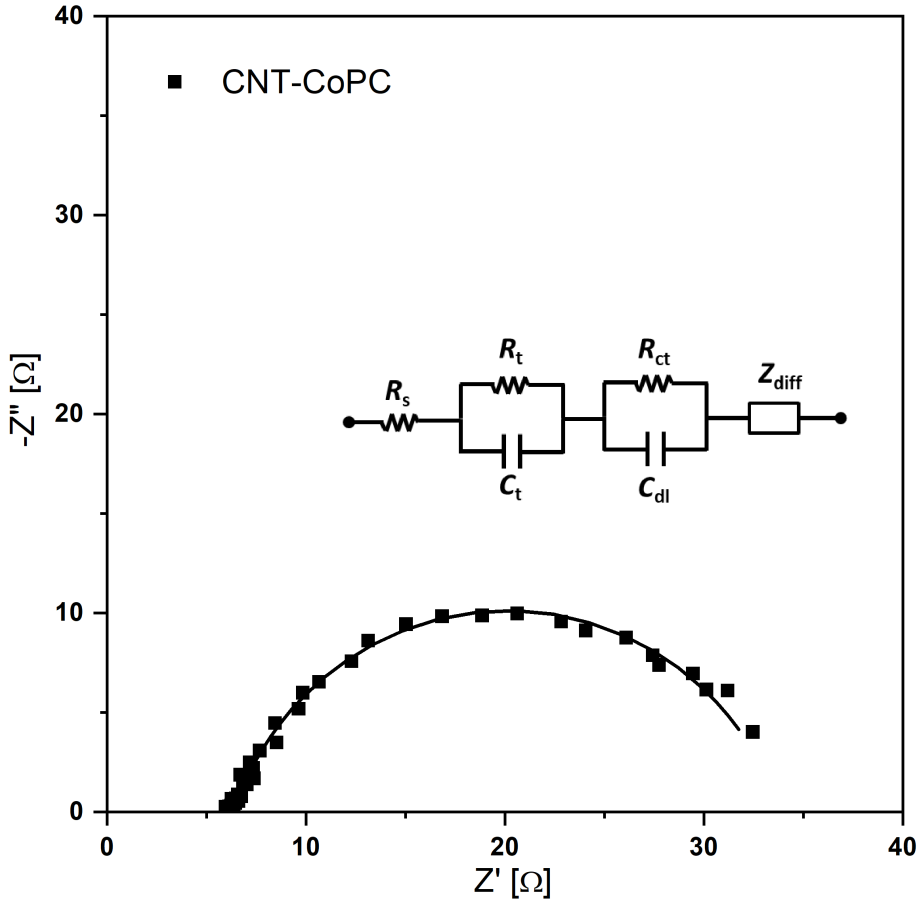

Figure 5.16: Nyquist plot of measures for CoPc-MWCNT 1:3 electrode with curve fitting to calculate equivalent circuit parameters.

This reduction of effective active area is given by the excessive binder coverage, catalytically inactive, on the surface limiting the performances of the electrodes in terms of FEs. In contrast, the strong reduction of R_{ct} indicates fast reaction kinetics and electron transfer, characteristic of the MWCNT high conductivity.

5.1.3 Conclusions

The hierarchically designed CoPc–MWCNT catalyst has proven to be a more efficient option compared to pure SACs. Pristine CoPc exhibited no catalytic behaviour, which was attributed to its intrinsic agglomeration into organized structures. To mitigate this effect, MWCNTs have been used has a support to help redistribution of the CoPc molecules through $\pi - \pi$ interactions. FESEM images showed no phase separation of CoPc, confirming a reduced agglomeration of the CoPc molecules. This observation is confirmed with XPS analysis of the C 1s peak, which not only confirmed the presence of $\pi - \pi$ interactions but also revealed an increased carbon atomic concentration. Combined XRD and XPS analyses have highlighted the presence of a multilayer of CoPc molecules on the MWCNTs support with small crystallites. Even if the molecules aren't perfectly distributed in a monolayer, the characterizations still confirm the efficient synthesis of the supported catalyst.
Despite its desirable characteristics, the hierarchically designed catalyst was inefficient when

tested in the bicarbonate electrolyzer. The low performances of the electrode are linked to the excessive quantity of binder employed. This led to the covering of the electrode with polymeric binder, a catalytically inactive material, reducing the effective active area observed through EIS. Not reaching the Ag-based electrodes results and observing the limitation of the CoPc-MWCNT catalyst, CB can be considered as a possible alternative support.

5.2 Hierarchically designed CB-supported CoPc

This section will discuss the effectiveness of CB used as an alternative carbon support to MWCNT in hierarchically designed SAC. CB is considered as a suitable alternative to MWCNT exhibiting particle form allowing for better dispersion in the ink solution requiring less binder material. Limiting the binder usage should increase the effective active area allowing for better performances of the electrode. This effect is combined with a turbostratic structure allowing for $\pi - \pi$ interactions with CoPc. The newly produced supported catalysts are tested to compare their performances with that of simple CoPc and Ag-based electrodes.

5.2.1 Materials and methods

Catalyst fabrication

To compare the different carbon supports, CoPc-CB powders are produced with the same ratios as MWCNT-supported CoPc. CB (Cabot Vulcan XC 72R) and CoPc nanoparticles (Sigma Aldrich 97%) are mixed in N,N Dimethylformamide (DMF, Sigma Aldrich 99.8%) to allow the powders to interact with $\pi - \pi$ bonding.

Following the MWCNT-supported CoPc recipe, two batches of CB-supported CoPc have been produced:

- **CoPc-CB 1:3**: 13 mg CoPc nanoparticles are dispersed in 20 mL of DMF and reacted with 30 mg of CB are dispersed in 30 mL of DMF.
- **CoPc-CB 4:6**: 20 mg CoPc nanoparticles are dispersed in 20 mL of DMF and reacted with 30 mg of CB are dispersed in 30 mL of DMF.

The particle form of VXC 72R CB shows great dispersion in DMF requiring only a few minutes of sonication before reacting with CoPc. CoPc solution is added drop by drop into the CB solution. The combined solution is stirred for 24h under a fume hood at 140°C.

Powder precipitation

The powder precipitation follows the same scheme explained in Figure 5.1 but replacing the MWCNT with VXC 72R CB. The final solutions are cooled with ice and powder is precipitated with a centrifuge machine. The resultant DMF is again investigated by UV-vis to monitor residual CoPc.
The precipitated powder is washed with methanol to remove residual DMF and centrifuged until the solution is clear. The final powders are dried in a Buchi Vacuum oven set at 60°C for 1 hour. The results are CB-supported CoPc powders.
The different powders obtained are used to produce a bicarbonate electrolyzer GDE. A simple CoPc reference electrode is also produced to compare the results. They are tested in the same conditions as for Ag based electrodes.

Electrode Manufacturing

CB-supported CoPc powders are deposited on a 5cm^2 square Freudenberg H23 carbon paper substrate using spraycoating. The spraycoating ink is composed of 10 mL methanol in which are dispersed 12 mg of the CoPc-CB catalyst and 77.8 μL of a 5 wt% Nafion binder solution. Only 10% of binder compared to the total deposited mass is required given its particle nature. To have a well dispersed system, the inks are sonicated for 30 minutes.
Spraycoating is carried out on a Nadatech Innovation™ spraycoating machine. For a uniform deposition and limiting aggregation, the inks are deposited 2 mL at the time leaving the remaining ink in the sonication bath. The two electrodes of CoPc-CB 1:3 and 4:6 ratios are obtained with a 2.0 mg cm^{-2} catalyst loading.

For comparison, a pure CoPc electrode is also manufactured using the Ag nanoparticle electrode recipe. The coating ink for this electrode is composed of 4 mL of IPA in which is dispersed 30 mg of CoPc nanoparticles (Sigma Aldrich 97%) with 77.8 μL of a 5 wt% Nafion binder solution on a 5cm^2 square Freudenberg H23 carbon paper. The ink is sonicated for 30 minutes and spraycoated obtaining a catalyst loading of 2.9 mg cm^{-2}.

Electrochemical tests and characterization

The pure CoPc electrode and both CoPc-CB 1:3 and 4:6 electrodes are tested on the generic test bench (section 3.2.1) using a zero-gap MEA setup with 3M $KHCO_3$ as catholyte and 0.05M H_2SO_4 as anolyte. Chronopotentiometry is performed on the cell applying a constant current of 200 mA cm^{-2} and monitoring the cell voltage. During these tests, gaseous products were analyzed using a Micro-GC. Additionally, EIS and the calculated parameters (section 4.1.2) are used quantify interfacial electronic properties.
To characterize the synthetized material, FESEM images are obtained to evaluate the catalysts morphology and role of the carbon supports. XPS provides a superficial chemical analysis, enabling a quantification of each element and their characteristics. In particular, detailed observation of the Carbon C1s peak and shifts of peaks offer information about the $\pi - \pi$ interactions and possible defects. To complete chemical and physical characterization, XRD measurements are also conducted on the produced powders compared to commercial CoPc. XRD allows for the determination of composing phases of the material but also the determination of possible defects and crystallinity of the system. Residual DMF from the centrifugation of the solution is analyzed using UV-vis spectroscopy to identify the amount of CoPc that hasn't bonded with CB particles.

5.2.2 Results and Discussion

Electrochemical results

The produced CoPc-CB electrodes are tested inside the bicarbonate electrolyzer compared to standard CoPc electrode on the generic bench setup described in Section 2.2.2. Calculated FEs and measured voltage cell are plotted in Figure 5.17

A significant improvement in catalytic performance is observed: simple CoPc show little to none catalytic activity while the CoPc-CB GDE achieve up to 56% FE_{CO} at 1:3 ratio. The FEs in this case are much higher than previous MWCNT-supported CoPc in the same conditions, surpassing also the 48% FE_{CO} of optimized Ag-based GDE at 40°C (section 4.3.2). VXC 72R CB is a partly amorphous carbon-based material with short-range order in particle form. Its high

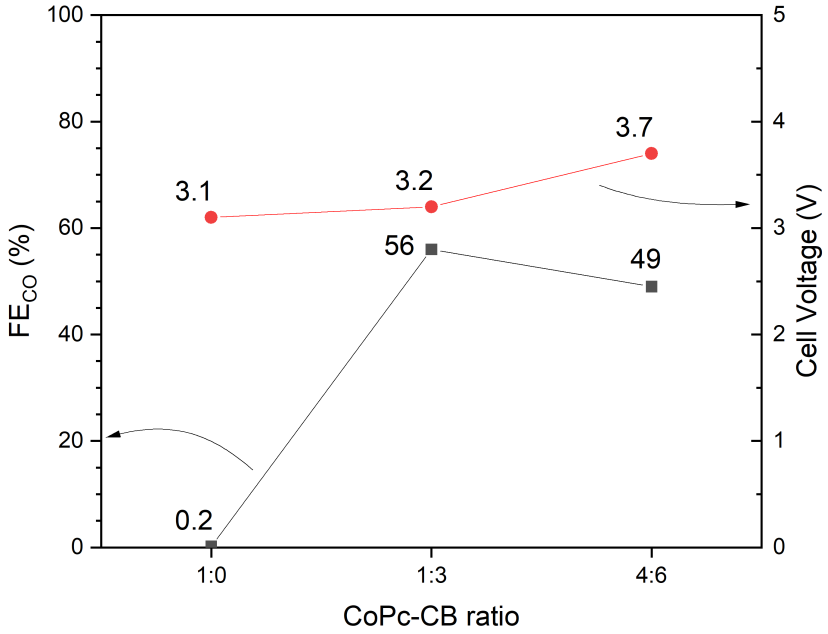

Figure 5.17: FE of CO (black) and cell voltage (red) of CoPc-CB electrodes at different ratios maintaining a current density of 200 mA cm^{-2}.

dispersibility in the ink solution allows for the use of less binder in the electrode's composition. This frees up more of the electrode's surface area for catalytic activity, resulting in improved performance.
To verify this hypothesis, further characterizations are performed on the efficient CoPc-CB 1:3 sample. UV–Vis spectroscopy on the extracted DMF, then FESEM, XRD and XPS on the produced catalyst are carried out to determine the correct production and interactions between CoPc and CB. Once the properties of the CoPc-CB catalyst defined, an EIS analysis is conducted on the electrode to observe the effective increase of active area comparing the results to previous electrodes.

UV-visible spectroscopy

UV-visible spectroscopy is performed on the extracted DMF solvent of the CoPc-CB 1:3 catalyst to detect possible unreacted CoPc. Other than defining the effective quantity of CoPc that reacted with CB supports, it can be compared with the results in the previous section.
From the UV-vis spectra no other species than CoPc can be determined, guaranteeing no side reactions. The unreacted CoPc mass is obtained using the same mother solution and dilutions of section 5.1.3, measuring the maximum absorbance of the DMF solvent and using the linear fitting. In Figure 5.18 are plotted with a MatLab program the maximum absorbance of each dilution with their linear fitting, with CoPc-MWCNT 1:3 and CoPc-CB 1:3 measured absorbance maximum.

Using equation 5.1, it results that the unreacted mass of CoPc is **0.17 mg**. Considering the initial mass of CoPc being 13 mg, only 1.3% of mass was lost in the solvent. Comparing this result with the 0.55 mg of unreacted CoPc using MWCNT in the same conditions, it suggests a better reaction with CB. CB exhibits much higher dispersion in DMF compared to MWCNT,

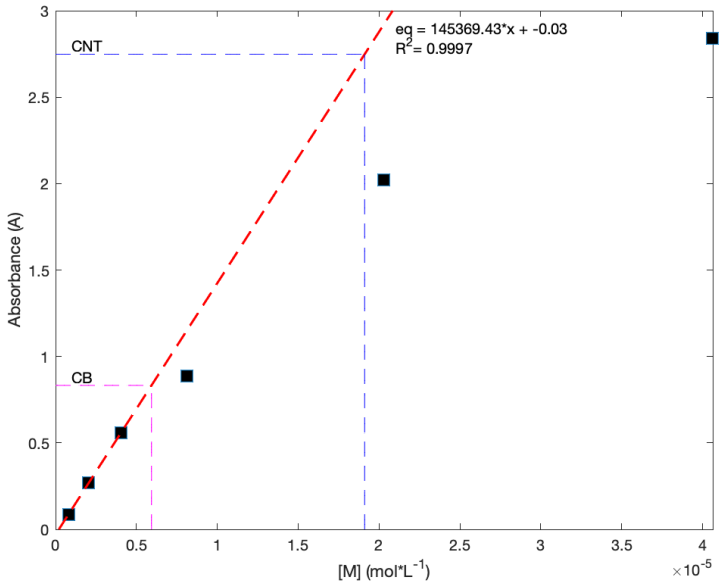

Figure 5.18: Linear fitting (dotted line) of the maximum absorbance of each CoPc-DMF dilution (black) with the maximum absorbance of the DMF solvent of the 1:3 ratio CoPc-MWCNT and CoPc-CB powder. Equation and R^2 value are reported in the graph.

which may explain a higher reaction rate leading to better bonding with CoPc.

FESEM Characterization

FESEM characterization is carried out in Figure 5.19 to observe the morphology of the produced CoPc-CB 1:3 catalyst and comparing it to pure CoPc and CoPc-MWCNT 1:3 catalyst.

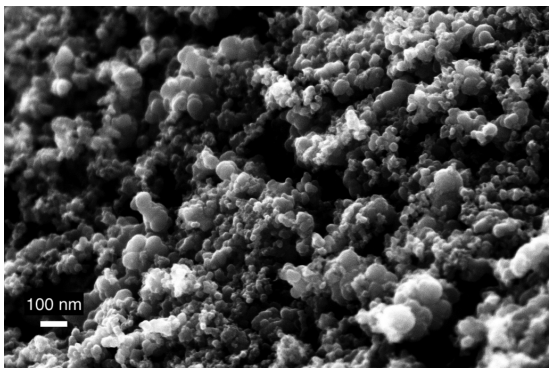

(a) VXC 72R CB sample at 50k X

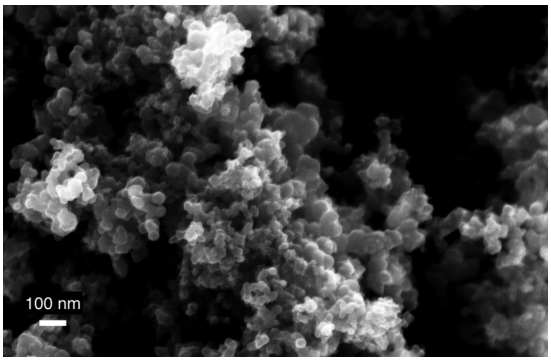

(b) CoPc-CB 1:3 at 50k X

Figure 5.19: FESEM images (secondary electron mode, 5 kV) of pristine VXC 72R CB and CoPc-CB 1:3 samples at 50k X magnification.

FESEM images revealed the spherical primary particle structure of CB. The pristine VXC 72R CB sample shows spherical particles evenly distributed on the inspected surface with 10-100 nm diameter distribution, displaying no long-range order. The CoPc-CB 1:3 sample exhibits the same morphology without any observable CoPc agglomeration. This suggests that the CoPc effectively reacts by binding itself to the turbostratic structure of the CB surface.

To confirm these observations, detailed physical and chemical characterizations are conducted on the CoPc-CB 1:3 catalyst.

XPS Analysis

An initial survey spectra is obtained to determine superficial elemental composition using the NIST and Handbook of X-ray Photoelectron Spectroscopy [92], reported in Figure 5.20.

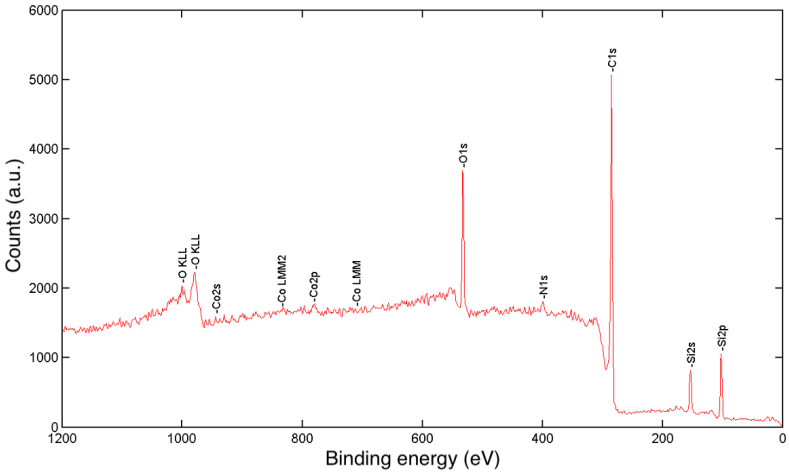

Figure 5.20: Labelled survey spectra of CoPc-CB 1:3 obtained via XPS analysis.

From the survey can be determined the composing elements of CoPc: cobalt, nitrogen, oxygen, silicon and carbon. The carbon peak is the most intense but comparable to the measured carbon peak of CoPc. Oxygen is also present, indicating possible surface interactions with oxygen molecules or oxidized material. The low-range order and high surface of CB can be responsible for oxidation of the surface increasing the superficial active sites. Another peculiarity is the presence of silicon observing the Si 2p and 2s peaks at 99 eV and 153 eV respectively. Observing silicon and oxygen could indicate the presence of silica SiO_2, an inert material without catalytic properties. It can be considered as a glass vial contamination, originating from the manufacturing process.
From the composition determined by the survey spectra, HR spectra are obtained of carbon C 1s, nitrogen N 1s, oxygen O 1s and cobalt Co 2p, shown in Figure 5.21.

The chemical composition of the produced powder obtained from the area of the subtracted baseline HR peaks using the trapezoid method (equation 5.2) normalized with the identified RSF is reported in Table 5.6.

Table 5.6: Atomic concentration of each identified element of the CoPc-CB sample obtained from the areas of HR peaks normalized with RSFs.

Element	Area (-)	RSF (-)	Atomic concentration (%)
C 1s	1610	0.314	77.7
Co 2p	90.8	2.113	0.58
N 1s	52.5	0.499	1.6
O 1s	975	0.733	20.2

The CoPc-CB 1:3 catalyst shows very low atomic concentration of cobalt at 0.58% and high concentrations of oxygen at 20.2%. The high atomic concentration of oxygen can be

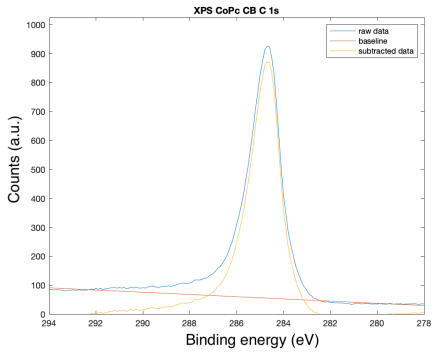

(a) HR spectra of C 1s

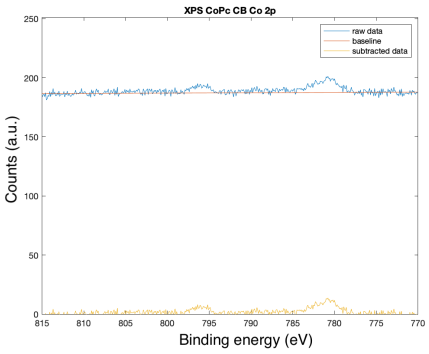

(b) HR spectra of Co 2p

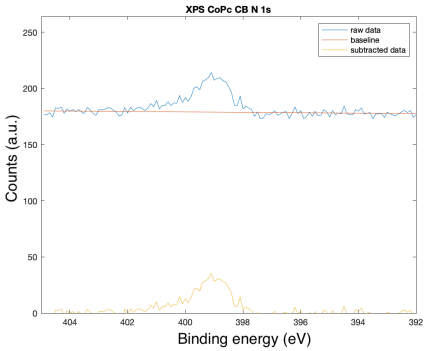

(c) HR spectra of N 1s

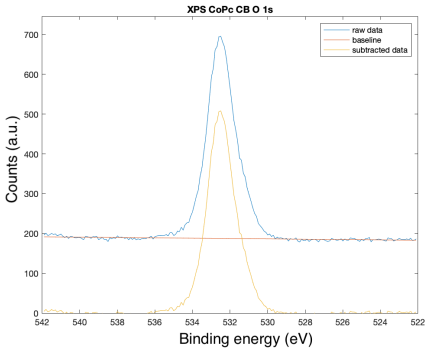

(d) HR spectra of O 1s

Figure 5.21: HR spectra of CoPc-CB sample. C 1s, Co 2p, O 1s and N 1s plotted with the measured data, the calculated baseline and the subtracted baseline.

linked to the high surface area of CB facilitating the adsorption of oxygen molecules and the possible presence of SiO_2 contamination. The CoPc-CB 1:3 catalyst showed excellent catalytic performances with this chemical composition, a clear indicator that the most important factor for efficiency is how the catalysts behaves with the support.
XPS not only allows for a quantitative study but also understanding molecular interactions. Comparing the Co 2p 1/2 and 3/2 of both pristine CoPc and CoPc-CB sample it is possible to observe differences between the two peaks distance (Figure 5.22).

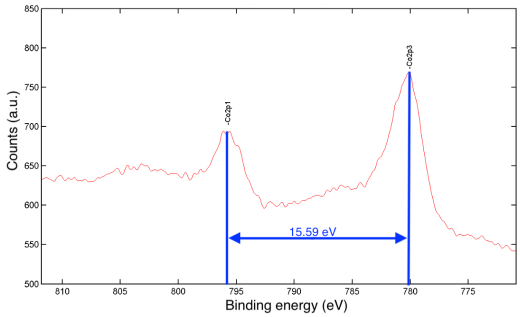

(a) CoPc sample

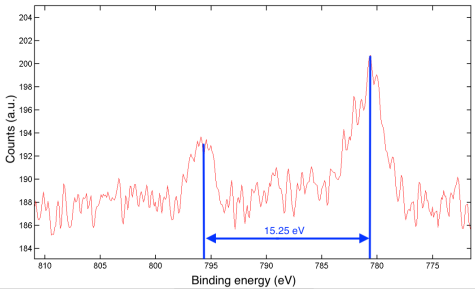

(b) CoPc-CB 1:3

Figure 5.22: Comparison between the Co 2p 1/2 and 3/2 distance in the HR spectra of both pristine CoPc and CoPc-CB sample.

Based on the considerations from Schmid et al. [94], a Co 2p inter-peak distance of 15.25 eV is measured in the CoPc-CB 1:3 sample. Compared to the previous CoPc-MWCNT 1:3

sample's 15.62 eV peak gap, this smaller distance indicates an improvement from a multilayer to a more efficient monolayer structure. This suggests that the CoPc molecules are more effectively covering the carbon support, reducing the multilayer structure. A higher energy shift can also be observed, which may be a sign of possible Co and O bonding and $\pi - \pi$ interactions between CoPc and CB [95].
To investigate the effective $\pi - \pi$ interaction, a detailed deconvolution is performed on the C 1s peak. A deconvolution with gaussian distributions separate the contribution of sp^2 carbons, sp^3 hybridized carbons (defects) and the $\pi - \pi*$ transition. The deconvolutions of the previously studied CoPc-MWCNT 1:3 sample and the CoPc-CB 1:3 sample are compared in Figure 5.23.

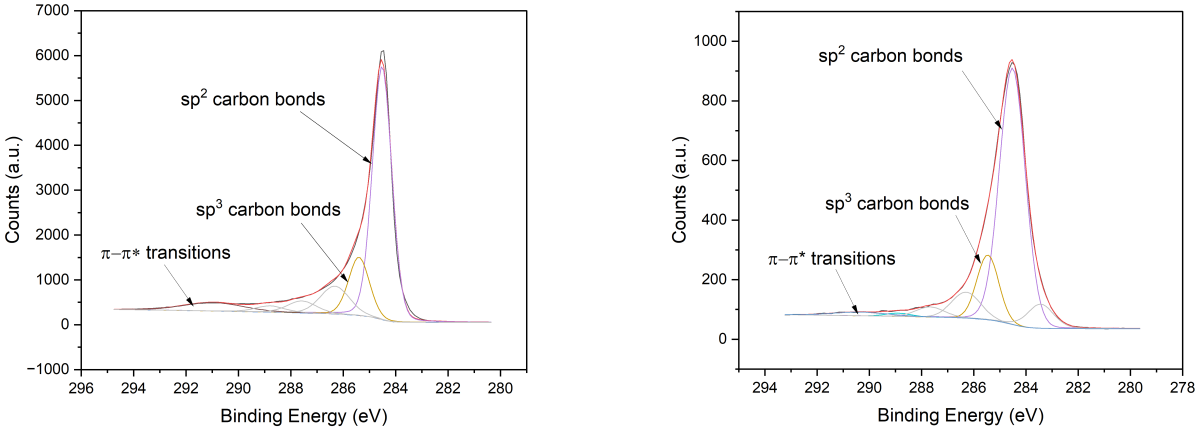

(a) CoPc-MWCNT 1:3 sample

(b) CoPc-CB 1:3 sample

Figure 5.23: Deconvolution of HR spectra of C 1s peaks of CoPc-MWCNT 1:3 and CoPc-CB 1:3 sample. Three peaks relative to sp^2 carbons, sp^3 carbons and defects, and to $\pi - \pi*$ transitions are observed.

VXC 72R CB is characterized by a turbostratic structure, a graphitic plane close upon itself. This structure can be observed by the peak deconvolution (Figure 5.23b.) having a strong sp^2 carbon contribution. Defects and sp^3 carbons bonds are limited observing a reduced peak. A strong $\pi - \pi*$ transition contribution is also visible at the origin of the interactions between catalyst and support. The transition peak is shifted to higher energies and is more dispersive, indicator of efficient interactions but isn't as evident as the one present in the CoPc-MWCNT 1:3 sample. Overall, the presence of graphitic structures combined with high superficial area are key aspects to the effectiveness of CB. Effective $\pi - \pi$ interaction can be observed combined with a reduced multilayer suggesting a more uniform covering of the carbon substrate.

XRD Analysis

XRD analysis is carried out to further investigate the effective reduction of particle agglomeration. Different XRD results of pristine CoPc, CoPc-MWCNT 1:3 and CoPc-CB 1:3 are compared in Figure 5.24 using a MatLab program.

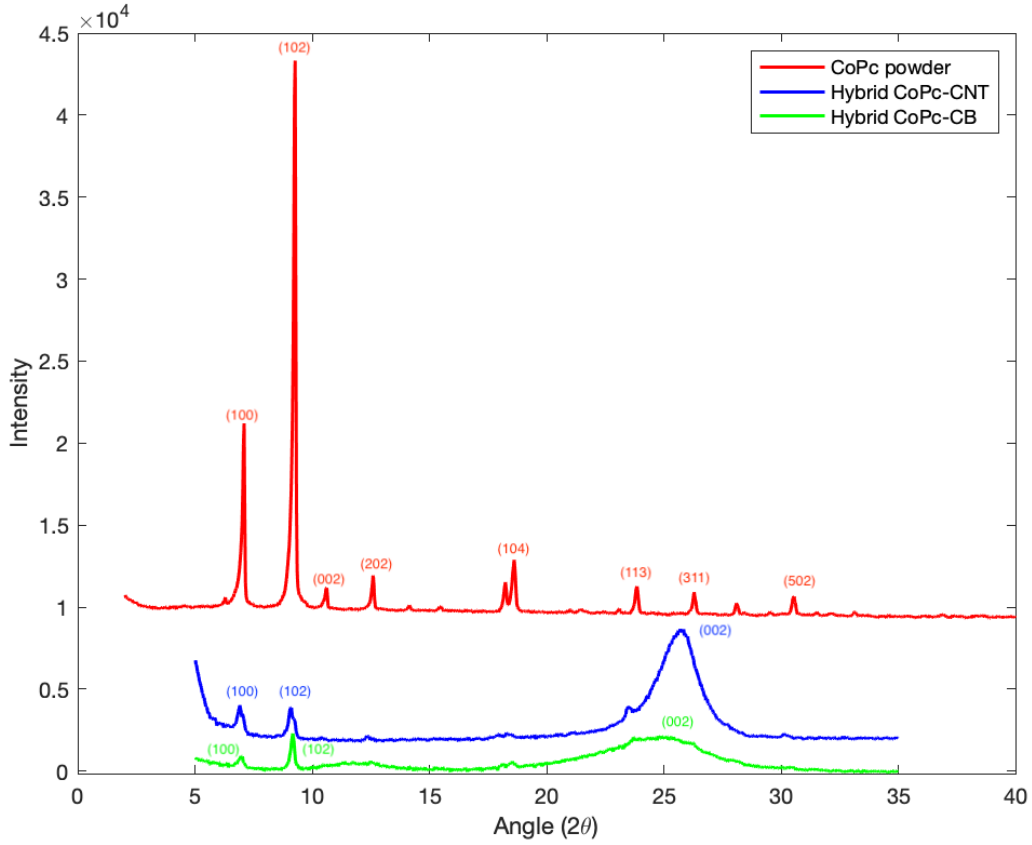

Figure 5.24: XRD measurements of pristine CoPc powder (red), CoPc-MWCNT 1:3 (blue) and CoPc-CB 1:3 (green).

The results show the presence of β-CoPc characteristic peaks and of carbon support broader peak at 25° in the supported catalysts. Comparing the width of the carbon (002) peak: the FWHM for CoPc–CB 1:3 is 2.34, while for CoPc–MWCNT is 0.974. A wider peak relative to the carbon support indicates reduction of preferential orientation of the material, sign of reduced periodicity in the CB-supported structure compared to MWCNT supports. Spherical particles do not exhibit preferential orientation while MWCNT exhibit orientation along its axis. The characteristic 7.09° and 9.28° peaks show also some variations from the pristine CoPc, as shown in Figure 5.25.

It is observed that both supported catalysts exhibit wider (102) peaks compared to pristine CoPc but the CoPc-CB shows similar ratios between peaks. Similar ratios of XRD peak can be related to the presence of possible CoPc aggregation, but the widening of peaks and reduced intensity define small crystalline regions.
The average crystallite size of the CoPc–CB 1:3 catalyst, obtained using the Scherrer equation (equation 3.1) is **6.85 nm**. For comparison, the CoPc–MWCNT 1:3 catalyst had an average crystallite size of 9.05 nm. Considering these observations, it is possible to say that CoPc-CB 1:3 showed reduced aggregation originating from the particle form of CB and interaction

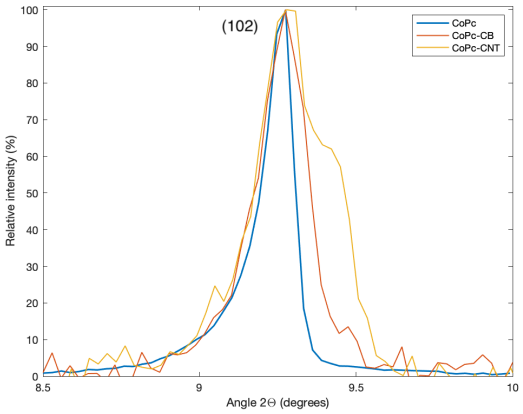

Figure 5.25: Comparison of CoPc, CoPc-CB and CoPc-MWCNT (102) peak on a normalized scale respect to the maximum.

between catalyst and support.

EIS analysis

Having demonstrated the successful functionalization of the carbon support, the EIS will focus on evaluating the effective active area of the electrode. As noted previously, the CoPc-CB 1:3 electrode required small amounts of Nafion binder, which is expected to result in increased active area and contribute positively to the electrode's performance. The procedure follows the methodology described in Section 3.2.3. The corresponding Nyquist plot are shown Figure 5.26, with the calculated parameters R_{ct} and C_{dl} are transcribed in Table 5.7 compared to CoPc-MWCNT 1:3 catalyst and the double layer electrode.

Table 5.7: Measured IES parameters for CoPc-CB 1:3 and CoPc-MWCNT 1:3 catalysts compared to double layer electrode.

Electrode	R_{ct} (Ω)	C_{dl} (F)
CoPc-CB 1:3	21.14	6.03E-4
CoPc-MWCNT 1:3	29.08	1.35E-4
Double layer	43.57	3.31E-4

The CoPc-CB sample exhibits a lower R_{ct} with an almost doubled C_{dl} compared to the double layer electrode. Interpreting the results, the CoPc-CB shows almost twice active sites respect to the double layer electrode and very high kinetics with efficient electron transfer. The R_{ct} value is even lower than the one of the CoPc-MWCNT sample, an indicator of efficient electron transfer between the particles increasing the reaction kinetics. The observed increase in the density of active site can be related to the efficient dispersion and particle shape of CB. The faster reaction kinetics can be explained by the presence of carbon supports, as it being expressed in the supported catalysts. Comparing with the MWCNT contribution, CB has a more desired behaviour increasing the effective site density with high reaction kinetics and electron transfer. This effect creates a preferential pathway for electrons to be transported on the electrodes surface, reaching efficiently catalytic active sites.

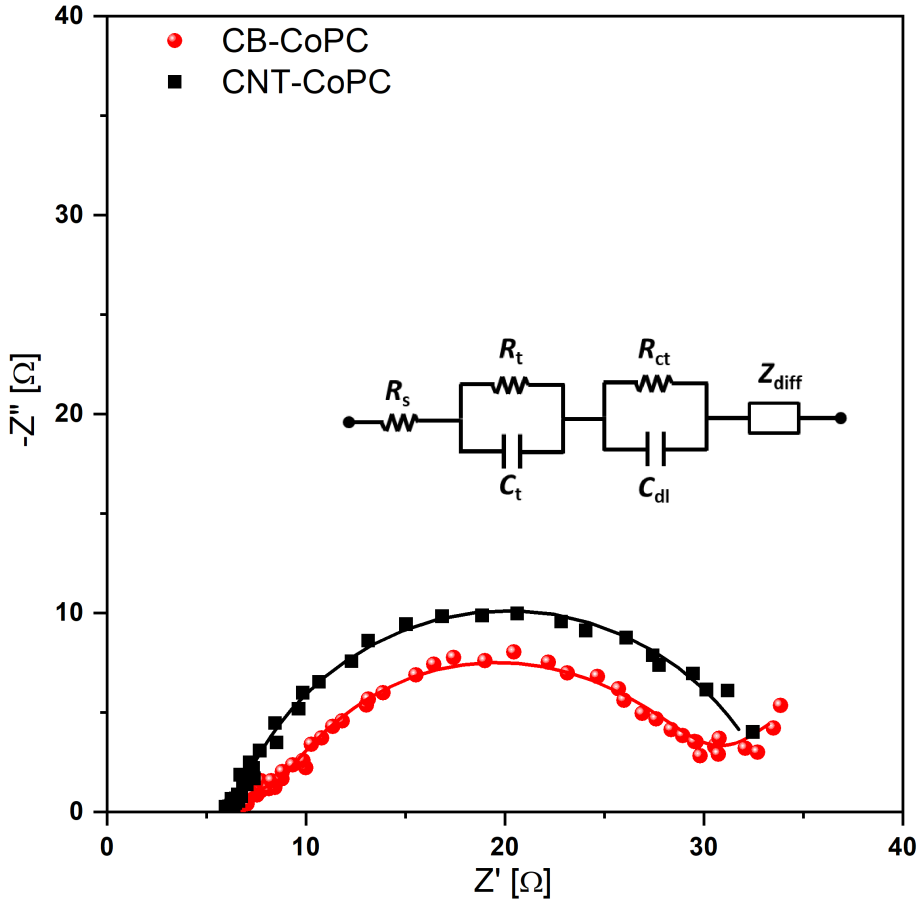

Figure 5.26: Nyquist plot of measures for CoPc-CB 1:3 and CoPc-MWCNT 1:3 electrodes with curve fitting to calculate equivalent circuit parameters.

5.2.3 Conclusions

The use of VXC-72R CB as a support for hierarchically designed CoPc catalysts significantly improved electrolyzer performance, reaching up to 56% FE_{CO}. These results exceed those of previously studied MWCNT-supported catalysts and even optimized Ag-based electrodes under controlled conditions. Having a turbostratic structure, CB displayed comparable π–π interactions to MWCNT-supported catalysts. This is attributed to the highly graphitic structure and the small size of the spherical CB particles (10–100 nm), providing a large surface area. This high surface area enhances contact between the catalyst and the support, ensuring an effective coating of the carbon support. In addition, the spherical morphology reduces aggregation and improves dispersion when deposited on the carbon paper substrate. XRD analysis confirmed that CB-supported catalysts form smaller crystallites than both MWCNT-supported and pristine CoPc, indicating reduced agglomeration. The effective design of the CoPc-CB catalyst is combined with the advantage of using less binder due to its excellent dispersion in the ink. The produced electrode exhibits high active area, reduced agglomeration of catalyst and fast kinetics with high electron transfer. All these properties combined define a high performance electrode.

Chapter 6

Conclusions and final remarks

This thesis has explored the strategies to optimize conversion in integrated CCU through a bicarbonate electrolyzer. Integrated CCU combines carbon capture with electrochemical valorization, where CO_2 is recovered in gaseous form inside the cell and directly converted into products. This approach lowers energy demand compared to traditional CCU but introduces new challenges. The main objective of this work was to increase the electrochemical conversion from CO_2-to-CO while reducing costs related to materials through the use of innovative catalyst materials.

The study addressed two main aspects: (1) the electrode design of a CEM-based zero-gap cell, and (2) the influence of operating conditions, in view of potential industrial scale-up. The research began with Ag-based monometallic catalysts, currently the most established benchmark. Optimization focused on selecting the correct polymeric binder, silver mass loading and integration of a sputtered layer. Electrochemical tests and material characterization showed that the double layer electrode combining Ag sputtering with Ag nanoparticles deposition showed 41% FE_{CO}. To evaluate the electrolyzer's performance in pressure, a partial pressure was created inside the electrolyzer's tubes, increasing the solution's residence time. However, no significant improvements were observed with pressures up to 1 bar. In contrast, temperature showed moderate improvements, with performance peaking at around 40 °C, where it reached 48% FE_{CO}, before declining at higher temperatures.

Despite their catalytic efficiency, noble metals like silver are too expensive and scarce for large-scale industrial use. This has prompted a search for a low-cost, energy-efficient alternative. Single-atom catalysts, such as CoPc, have emerged as a possible solution with catalysts. CoPc has very little catalytic properties due to its strong agglomeration, but its properties can be improved by dispersing the molecules on carbon supports through π–π interactions. Highly graphitic multi-walled carbon nanotubes (MWCNTs) supports were initially used as a support, demonstrating an increase in performance but were limited by large amounts of binder for effective dispersion. The binder directly reduces the active surface area reducing the catalytic properties. As an alternative, carbon black (CB) particles combined a high surface area and a better dispersion in the ink, reducing the quantity of binder required. The creation of CB-supported CoPc led to excellent performances up to 56% of FE_{CO}, surpassing Ag-based electrodes.

To conclude, this work presented potential pathways for improving the efficiency of bicarbonate electrolyzers and explored new and innovative catalytic materials. The synthetized catalysts open the way to large scale electrolyzer usage to convert capture CO_2 waste into valuable

products. The integrated utilization of the bicarbonate capture solvent and operating with low-voltage cell supports an energy-efficient process. This research provides a vision of circular carbon economy using low-cost electrochemical processes, where CO_2 is no longer a pollutant but instead a valuable resource for sustainable production of value-added products, closing the carbon loop.

Bibliography

[1] *Can Climate Affect Earthquakes, Or Are the Connections Shaky?* 2019. URL: https://science.nasa.gov/earth/climate-change/can-climate-affect-earthquakes-or-are-the-connections-shaky/.

[2] Christina Nunez. "Carbon dioxide levels are at a record high. Here's what you need to know." In: *National Geographic* (2019). URL: https://education.nationalgeographic.org/resource/carbon-dioxide-levels-are-record-high-heres-what-you-need-know/.

[3] Nils-Axel Mörner. "Anthropogenic Global Warming (AGW) or Natural Global Warming (NGM)". In: *Scientific Research Publishing* 4 (2018), pp. 51–59. DOI: 10.4236/vp.2018.44005. URL: https://doi.org/10.4236/vp.2018.44005.

[4] Nils-Axel Mörner. *The Greatest Lie Ever Told*. P and P print, 2007.

[5] D. J. Easterbrook. *Evidence-Based Climate Science*. Elsevier, 2011.

[6] IEA. *World Energy Balances Highlights*. IEA Highlights, 2023.

[7] G.J.M Velders. "Effect of greenhouse gas emissions on stratospheric ozone depletion". In: *PBL Netherlands Environmental Assessment Agency* (1997). URL: https://www.pbl.nl/uploads/default/downloads/722201011.pdf.

[8] John Houghton. *Global Warming*. Institute of physics publishing, 2005.

[9] Howard Herzog. "An Introduction to CO 2 Separation and Capture Technologies". In: *MIT laboratory report* (1999).

[10] A.I. Osman, M. Hefny, and M.I.A Abdel Maksoud. "Recent advances in carbon capture storage and utilisation technologies: a review". In: *Environmental Chemistry Letters* (2021). URL: https://doi.org/10.1007/s10311-020-01133-3.

[11] Sifat N. and Haseli Y. "A critical review of CO2 capture technologies and prospects for clean power generation". In: *Energies* (2019). URL: https://doi.org/10.3390/en12214143.

[12] M.M. Jaffar et al. "Comparative techno-economic analysis of the integration of MEA-based scrubbing and silica PEI adsorbent-based CO2 capture processes into cement plants". In: *Journal of Cleaner Production* 414 (2023). URL: https://doi.org/10.1016/j.jclepro.2023.137666.

[13] Zhongde Dai and Liyuan Deng. "Membrane absorption using ionic liquid for pre-combustion CO2 capture at elevated pressure and temperature." In: *Int. J. Greenh. Gas Control* (2016). URL: https://doi.org/10.1016/j.ijggc.2016.09.001.

[14] Jiawei Zhang et al. "Closing the Anthropogenic Chemical Carbon Cycle toward a Sustainable Future via CO2 Valorization". In: *Advanced Energy Materials* (2021). URL: https://doi.org/10.1002/aenm.202102767.

[15] Ahmed Al-Mamoori et al. “Carbon Capture and Utilization Update”. In: *Energy Technology* (2017). URL: https://doi.org/10.1002/ente.201600747.

[16] H. Sarafraz et al. “Economic and Efficient phosphonic functional groups mesoporous silica for uranium se- lective adsorption from aqueous solutions”. In: *Sci. Rep.* 9.1 (2019), pp. 1–10. URL: https://doi.org/10.1038/s41598-019-46090-2.

[17] L. Irlam. “GLOBAL COSTS OF CARBON CAPTURE AND STORAGE 2017 Update”. In: *Global CCS Institute* (2017). URL: https://www.globalccsinstitute.com/archive/hub/publications/201688/global-ccs-cost-updatev4.pdf.

[18] S. Samanta and R. Srivastava. “Catalytic conversion of CO2 to chemicals and fuels: The collective thermocatalytic/photocatalytic/electrocatalytic approach with graphitic carbon nitride”. In: *Royal Society of Chemistry* (2020). URL: https://doi.org/10.1039/D0MA00293C.

[19] Georgios Varvoutis et al. “Support-induced modifications on the CO2 hydrogenation performance of Ni/CeO2: The effect of ZnO doping on CeO2 nanorods”. In: *Journal of CO2 Utilization* (2022). URL: https://doi.org/10.1016/j.jcou.2022.102057.

[20] Michele Aresta, Angela Dibenedetto, and Antonella Angelini. “Catalysis for the valorization of exhaust carbon: From CO2 to chemicals, materials, and fuels. technological use of CO2”. In: *Chemical reviews* (2014). URL: https://doi.org/10.1021/cr4002758.

[21] Chery Déborah, Lair Virginie, and Cassir Michel. “Overview on CO 2 valorization: Challenge of molten carbonates”. In: *Frontiers in energy research* (2015). URL: https://www.frontiersin.org/journals/energy-research/articles/10.3389/fenrg.2015.00043.

[22] Wenlei Zhu et al. “Active and selective conversion of CO2 to CO on ultrathin Au nanowires”. In: *J Am Chem Soc* (2014). URL: https://doi.org/10.1021/ja5095099.

[23] Mikael Höök et al. “Hydrocarbon liquefaction: viability as a peak oil mitigation strategy”. In: *PHILOSOPHICAL TRANSACTIONS OF THE ROYAL SOCIETY A* 372 (2014). URL: https://doi.org/10.1098/rsta.2012.0319.

[24] P. Luis. “Use of monoethanolamine (MEA) for CO2 capture in a global scenario: Consequences and alternatives”. In: *Desalination* (2016). URL: https://doi.org/10.1016/j.desal.2015.08.004.

[25] Alessadro Volta. *On the electricity excited by the mere contact of conducting substances of different kinds*. Ed. by Hoepli. Università degli studi Pavia, 1800.

[26] E. Katz. “Electrochemical contributions: William Nicholson (1753–1815)”. In: *Electrochemical Science Advances* (2021).

[27] M. Faraday. *Experimental researches in chemistry and physics*. Taylor and Francis, 1859.

[28] A.P. O’Mullane. “Electrochemistry”. In: *Elsevier* (2013). URL: http://dx.doi.org/10.1016/B978-0-12-409547-2.05344-0.

[29] Ruinan He et al. “Advances in electrolyzer design and development for electrochemical CO2 reduction.” In: *EcoMat* 5.7 (2023). URL: https://doi.org/10.1002/eom2.12346.

[30] Sheng Zhang et al. “CO2 Reduction: From Homogeneous to Heterogeneous Electrocatalysis”. In: *Accounts of Chemical Research* 53 (2020), pp. 255–264. URL: https://doi.org/10.1021/acs.accounts.9b00496.

[31] A.J. Bard. *Electrochemical Methods: Fundamentals and Applications*. Wiley, 2001.

[32] Wenjun Zhang et al. “Progress and Perspective of Electrocatalytic CO2 Reduction for Renewable Carbonaceous Fuels and Chemicals. In Advanced Science”. In: *Wiley-VCH Verlag* 5.1 (2018). URL: https://doi.org/10.1002/advs.201700275.

[33] Michael L. Pegis et al. “Standard Reduction Potentials for Oxygen and Carbon Dioxide Couples in Acetonitrile and N,N-Dimethylformamide”. In: *Inorganic Chemistry* 54.24 (2015). URL: https://doi.org/10.1021/acs.inorgchem.5b02136.

[34] B. Nourmohammadi Khiarak et al. “Macro and Nano-Porous Ag Electrodes Enable Selective and Stable Aqueous CO2 Reduction”. In: *Small* (2024). URL: https://doi.org/10.1002/smll.202409669.

[35] Joseph Wang. *Analytical Electrochemistry*. Wiley, 2006.

[36] Marco Dunwell, Yushan Yan, and Bingjun Xu. “Understanding the influence of the electrochemical double-layer on heterogeneous electrochemical reactions”. In: *Current Opinion in Chemical Engineering* 20 (2018), pp. 151–158. URL: https://doi.org/10.1016/j.coche.2018.05.003.

[37] Y. Jean. *An Introduction to Molecular Orbitals*. Oxford University Press, 1993.

[38] Xingli Wang et al. “Electrochemical CO2 Activation and Valorization on Metallic Copper and Carbon-Embedded N-Coordinated Single Metal MNC Catalysts”. In: *Angewandte Chemie (International)* 63 (2024). URL: https://doi.org/10.1002/anie.202401821.

[39] F. Solymosi. “The bonding, structure and reactions of CO2 adsorbed on clean and promoted metal surfaces”. In: *Journal of Molecular Catalysis* 65 (1991), pp. 337–358. URL: https://doi.org/10.1016/0304-5102(91)85070-I.

[40] Qi Lu and Feng Jiao. “Electrochemical CO2 reduction: Electrocatalyst, reaction mechanism, and process engineering”. In: *Nano Energy* 29 (2016), pp. 439–456. URL: https://doi.org/10.1016/j.nanoen.2016.04.009.

[41] Yurou Celine Xiao et al. “Direct carbonate electrolysis into pure syngas”. In: *EES Catalysis* 54.1 (2023). URL: http://dx.doi.org/10.1039/D2EY00046F.

[42] Q. Lu, J. Rosen, and Y. Zhou et al. “A selective and efficient electrocatalyst for carbon dioxide reduction”. In: *Nat Commun* (2014). URL: https://doi.org/10.1038/ncomms4242.

[43] Toru Hatsukade et al. “Insights into the electrocatalytic reduction of CO2 on metallic silver surfaces”. In: *Physical Chemistry Chemical Physics* 27 (13814-13819 2014). URL: https://doi.org/10.1039/C4CP00692E.

[44] K. G. Schmitt and A. A. Gerwirth. “In Situ Surface-Enhanced Raman Spectroscopy of the Electrochemical Reduction of Carbon Dioxide on Silver with 3,5-Diamino-1,2,4-Triazole”. In: *ACS Publications* 118.31 (2014), pp. 17567–17576. URL: https://doi.org/10.1021/jp503598y.

[45] Q. Feng, Y. Sun, and X. Gu et al. “Advances of Cobalt Phthalocyanine in Electrocatalytic CO2 Reduction to CO: a Mini Review”. In: *Electrocatalysis* 13 (2022), pp. 675–690. URL: https://doi.org/10.1007/s12678-022-00766-y.

[46] Z. Weng, Y. Wu, and M. Wang et al. “Active sites of copper-complex catalytic materials for electrochemical carbon dioxide reduction”. In: *nature communications* 9.415 (2018). URL: https://doi.org/10.1038/s41467-018-02819-7.

[47] C. Sun, R. Gobetto, and C. Nervi. “Recent advances in catalytic CO2 reduction by organometal complexes anchored on modified electrodes”. In: *New Journal of Chemistry* 40.7 (2016), pp. 5656–5661. URL: https://doi.org/10.1039/C5NJ03426D.

[48] Minghui Zhu et al. “Elucidating the Reactivity and Mechanism of CO2 Electroreduction at Highly Dispersed Cobalt Phthalocyanine”. In: *ACS Energy Letters* 3.6 (2018). URL: https://doi.org/10.1021/acsenergylett.8b00519.

[49] Ichiro Yamanaka et al. “Electroreduction of Carbon Dioxide to Carbon Monoxide by Co-pthalocyanine Electrocatalyst under Ambient Conditions”. In: *ISIJ International* 55.2 (2015), pp. 399–403. URL: https://doi.org/10.2355/isijinternational.55.399.

[50] N. Corbin, J. Zeng, and K.Williams. “Heterogeneous molecular catalysts for electrocatalytic CO2 reduction”. In: *Nano Research* 12 (2019). URL: https://doi.org/10.1007/s12274-019-2403-y.

[51] Y. Bhargav Kumar. *Theoretical and Computational Chemistry*. Vol. 21. Elsevier, 2022.

[52] Mingming Huai et al. “Electrochemical CO2 reduction on heterogeneous cobalt phthalocyanine catalysts with different carbon supports”. In: *Chemical Physics Letters* 754.137655 (2020). Ed. by Elsevier. URL: https://doi.org/10.1016/j.cplett.2020.137655.

[53] Y. Wang et al. “Molecular Modification Strategies for Enhancing CO2 Electroreduction”. In: *Molecules* 30.3038 (2025). URL: https://doi.org/10.3390/molecules30143038.

[54] Jiahui Yang et al. “Insight into Impacts of $\pi - \pi$ Assembly on Phthalocyanine Based Heterogeneous Molecular Electrocatalysis”. In: *J. Phys. Chem. Lett.* 15.17 (2024). URL: https://doi.org/10.1021/acs.jpclett.4c00774.

[55] Jing-He Yang et al. “Cobalt Phthalocyanine–Graphene Oxide Nanocomposite: Complicated Mutual Electronic Interaction”. In: *The Journal of Physical Chemistry C* 117.8 (2013), pp. 3785–3788. URL: https://doi.org/10.1021/jp311051g.

[56] Miroslawa Pawlyta, Jean-Noël Rouzaud, and Stanislaw Duber. “Raman microspectroscopy characterization of carbon blacks: spectral analysis and structural information”. In: *Carbon* (2014). URL: http://dx.doi.org/10.1016/j.carbon.%202014.12.030.

[57] R.D. Heidenreich, W.M. Hess, and L.L. Ban. “Structure of spherule and layers inferred from electron microscopy and X-ray diffraction.” In: *Journal of Applied Crystallography* 1 (1968).

[58] Mengxin Shen, Liyao Ji, and Dongfang Cheng. “Hierarchical design enables sufficient activated CO2 for efficient electrolysis of bicarbonate to CO”. In: *Joule* 8 (2024). URL: https://doi.org/10.1016/j.joule.2024.04.006.

[59] S. Petrovic, P. Kurweill, and J. Garche. *Electrochemical Energy Storage*. McGraw Hill Professional, 2022.

[60] T. Sadhasivam et al. "An experimental investigation of the feasibility of Pb based bipolar plate material for unitized regenerative fuel cells system". In: *International Journal of Hydrogen Energy* 45.13101-13107 (2020). URL: https://doi.org/10.1016/j.ijhydene.2020.03.023.

[61] R. Pärnamäe, S. Mareev, and V. Nikonenko. "Bipolar membranes: A review on principles, latest developments, and applications". In: *Journal of Membrane Science* 617 (2021). URL: https://doi.org/10.1016/j.memsci.2020.118538.

[62] Noémi V. Galbicsek et al. "Comparative Study of Different Polymeric Binders in Electrochemical CO Reduction". In: *Energy and fuels* 38 (2024), pp. 22307–22314. URL: https://doi.org/10.1021/acs.energyfuels.4c04058.

[63] H. Li, P. Wei, and T. Liu. "CO electrolysis to multicarbon products over grain boundary-rich Cu nanoparticles in membrane electrode assembly electrolyzers". In: *nature communications* 15.4603 (2024). URL: https://doi.org/10.1038/s41467-024-49095-2.

[64] Akash S. Rasal, Hao Ming Chen, and Wen-Yueh Yu. "Electronic structure engineering of electrocatalyst for efficient urea oxidation reaction". In: *Nano Energy* (2024). URL: https://doi.org/10.1016/j.nanoen.2023.109183.

[65] Yongwook Kim et al. "Integrated CO2 capture and conversion to form syngas". In: *Joule* 8 (2024), pp. 3106–3125. URL: https://doi.org/10.1016/j.joule.2024.10.010.

[66] Ana Sofia Varela et al. "Controlling the selectivity of CO2 electroreduction on copper: The effect of the electrolyte concentration and the importance of the local pH". In: *Catalysis Today* 260 (2016), pp. 8–13. URL: https://doi.org/10.1016/j.cattod.2015.06.009.

[67] M.H. Ghobadi, M. Firuzi, and E. Asghari-Kaljahi. "Relationships between geological formations and groundwater chemistry and their effects on the concrete lining of tunnels (case study: Tabriz metro line 2)". In: *Environmental Earth Sciences* (2016). URL: https://doi.org/10.1007/s12665-016-5785-0.

[68] Thanh Ngoc-Dan Cao et al. "Unraveling the Potential of Electrochemical pH-Swing Processes for Carbon Dioxide Capture and Utilization". In: *Industrial and Engineering Chemistry Research* 49.20979-20995 (2023). URL: https://doi.org/10.1021/acs.iecr.3c02183.

[69] R. Philips and C. W. Dunnill. "Zero gap alkaline electrolysis cell design for renewable energy storage as hydrogen gas". In: *RSC Advances* 102 (2016), pp. 100643–100651. URL: https://doi.org/10.1039/C6RA22242K.

[70] S.J.C. Cleghorn, C.R. Derouin, and M.S. Wilson et al. "A printed circuit board approach to measuring current distribution in a fuel cell". In: *Journal of Applied Electrochemistry* 28.663 (1998). URL: https://doi.org/10.1023/A:1003206513954.

[71] Tatyana V. Reshetenko et al. "A segmented cell approach for studying the effects of serpentine flow field parameters on PEMFC current distribution". In: *Electrochimica Acta* 88 (2013), pp. 571–579. URL: https://doi.org/10.1016/j.electacta.2012.10.103.

[72] Yizhe Li et al. “A Comparative Study of CCM and CCS Membrane Electrode Assemblies for High-Temperature Proton Exchange Membrane Fuel Cells with a CsH5(PO4)2-Doped Polybenzimidazole Membrane”. In: *Materials* 16.11 (2023).

[73] Sang Hyun Ahn, Byung Seok Lee, and Insoo Choi et al. “Development of a membrane electrode assembly for alkaline water electrolysis by direct electrodeposition of nickel on carbon papers”. In: *Applied Catalysis B: Environmental,* (2014).

[74] Shaoxuan Ren et al. “Molecular electrocatalysts can mediate fast, selective CO2 reduction in a flow cell”. In: *Science* 6451.367-369 (2019). URL: https://doi.org/10.1126/science.aax4608.

[75] Zishuai Zhang et al. “pH Matters When Reducing CO2in an Electrochemical Flow Cell”. In: *ACS Energy Letters* 5 (2020), pp. 3101–3107. URL: https://doi.org/10.1021/acsenergylett.0c01606.

[76] Kohta Nomoto et al. “Highly selective formate formation via bicarbonate conversions”. In: *Royal Society of Chemistry* (2024). URL: http://dx.doi.org/10.1039/D4EY00122B.

[77] Alexandros Ch. Lazanas and Mamas I. Prodromidis. “Electrochemical Impedance Spectroscopy, A Tutorial”. In: *ACS Measurement Science Au* 3.3 (2023), pp. 162–193. URL: https://doi.org/10.1021/acsmeasuresciau.2c00070.

[78] Mary M. Walczak et al. “pH Dependent Redox Couple: An Illustration of the Nernst Equation”. In: *Journal of Chemical Education* 74.10 (Oct. 1997), p. 1195. DOI: 10.1021/ed074p1195. URL: https://doi.org/10.1021/ed074p1195.

[79] Ashok K. Singh. *Engineered nanoparticles*. Academic Press, 2016.

[80] Jianyun Zheng et al. “Defect engineering of the protection layer for photoelectrochemical devices”. In: *EnergyChem* 2 (2020). URL: https://doi.org/10.1016/j.enchem.2020.100039.

[81] M.N. Hafiz, Iqbal Muhammad Bilal, and Tuan Anh Nguyen. *Nano-Bioremediation : Fundamentals and Applications*. Elsevier, 2022.

[82] Ahmad Fauzi Ismail, Kailash Chandra Khulbe, and Takeshi Matsuura. *Reverse Osmosis*. Elsevier, 2019.

[83] A. Otsuki. *Non-Destructive Material Characterization Methods*. Elsevier, 2024.

[84] Marzieh Namdari et al. “Reactive carbon capture using electrochemical reactors”. In: *Chemical Society Reviews* (2025). URL: http://dx.doi.org/10.1039/D4CS00834K.

[85] N. Hussain et al. *Encyclopedia of Smart Materials*. Vol. 2. Elsevier, 2022.

[86] Yang Li et al. “Elevated temperature and pressure driven ampere-level CO2 electroreduction to CO in a membrane electrode assembly electrolyzer”. In: *EES Catalysis* 3.843 (2025). URL: http://dx.doi.org/10.1039/D5EY00034C.

[87] Stefan Piontek et al. “Influence of the Fe:Ni Ratio and Reaction Temperature on the Efficiency of (FexNi1x)9S8 Electrocatalysts Applied in the Hydrogen Evolution Reaction”. In: *ACS Catalysis* 8.2 (2018), pp. 987–996. URL: https://doi.org/10.1021/acscatal.7b02617.

[88] Yingxue Fu et al. “Inhibition of CO2 Carbonation Promotes Efficacy of Bicarbonate Electrolysis to CO”. In: *ACS Energy Letters* 10 (2025), pp. 2143–2149. URL: https://doi.org/10.1021/acsenergylett.4c03465.

[89] Shanhe Gong et al. “Elucidating influence of the existence formation of anchored cobalt phthalocyanine on electrocatalytic CO2-to-CO conversion”. In: *Nano Energy* 84 (2021). URL: https://doi.org/10.1016/j.nanoen.2021.105904.

[90] X. Zhang, Z. Wu, and X. Zhang. “Highly selective and active CO2 reduction electrocatalysts based on cobalt phthalocyanine/carbon nanotube hybrid structures”. In: *nature communications* 8 (2017). URL: https://doi.org/10.1038/ncomms14675.

[91] Jaecheol Choi et al. “Steric Modification of a Cobalt Phthalocyanine/Graphene Catalyst to give enhanced and stable electrochemical CO2 reduction to CO”. In: *ACS Energy Letters* 4 (2019). URL: https://doi.org/10.1021/acsenergylett.8b02355.

[92] J. F. Moulder. *Handbook of X-ray Photoelectron Spectroscopy*. Ed. by J. Chastain. Perkin-Elmer Corp., 1992.

[93] H. Estrade-Szwarckopf. “XPS photoemission in carbonaceous materials: A “defect” peak beside the graphitic asymmetric peak”. In: *Carbon* 42 (2004), pp. 1713–1721. URL: https://doi.org/10.1016/j.carbon.2004.03.005.

[94] Martin Schmid et al. “The electronic structure of cobalt(II) phthalocyanine adsorbed on Ag(111)”. In: *Surface Science* 606 (2012), pp. 945–949.

[95] Hejun Li, Zhanwei Xu, and Kezhi Li. “Modification of multi-walled carbon nanotubes with cobalt phthalocyanine: effects of the templates on the assemblies”. In: *J. Mater. Chem.* 21 (2011), pp. 1181–1186.

[96] Matthew Smith et al. “Improving the deconvolution and interpretation of XPS spectra from chars by ab initio calculations”. In: *Carbon* 110 (2016), pp. 155–171. URL: https://doi.org/10.1016/j.carbon.2016.09.012.

[97] D. Briggs and G. Beamson. “Primary and Secondary Oxygen-Induced C1s Binding Energy Shifts in X-ray Photoelectron Spectroscopy of Polymers”. In: *Anal. Chem.* 64 (1992), pp. 1729–1736. URL: https://doi.org/10.1021/ac00039a018.

[98] Xiaobin Fan et al. “Deoxygenation of Exfoliated Graphite Oxide under Alkaline Conditions: A Green Route to Graphene Preparation”. In: *Advanced Materials* 20 (2004), pp. 4490–4493. URL: https://doi.org/10.1002/adma.200801306.

[99] H. Soliman, A.M.A. El-Barry, and M. M. El-Nahass. “Structural and electrical properties of thermally evaporated cobalt phthalocyanine (CoPc) thin films”. In: *The European Physical Journal Applied Physics* 37.1 (2007). URL: https://doi.org/0.1051/epjap:2006135.

[100] Paolo Ballirano et al. “X-ray Powder Diffraction Structure reinvestigation of the α and β Forms of Cobalt Phthalocyanine and Kinetics of the α to β Phase Transition”. In: *J. Am. Chem. Soc.* 120 (1998), pp. 12798–12807. URL: https://doi.org/10.1021/ja973815p.

[101] Ungár T., Gubicza J., and Ribárik G. “Microstructure of carbon blacks determined by X-ray diffraction Abstract a profile analysis”. In: *Carbon* 40 (2002), pp. 929–937.